Direct Numerical Simulations of the Degeneration and Shear Instability of Large and Small Amplitude Basin Scale Internal Waves at Varied Aspect Ratios

by

Andrew Grace

A thesis
presented to the University of Waterloo
in fulfillment of the
thesis requirement for the degree of
Master of Mathematics
in
Applied Mathematics

Waterloo, Ontario, Canada, 2018

I hereby declare that I am the sole author of this thesis. This is a true copy of the thesis, including any required final revisions, as accepted by my examiners.

I understand that my thesis may be made electronically available to the public.

Abstract

This thesis presents high resolution simulations of the degeneration and shear instability of standing waves, or seiches, of varying amplitudes and aspect ratios in a continuously stratified fluid. It is well known that such waves evolve to form non–linear, dispersive wave trains under certain conditions. When the initial amplitude scaled by the upper layer depth (the dimensionless amplitude) is sufficiently large, it is possible that stratified shear instability develops, possibly at the same time as the formation of wave trains early in the evolution of the flow. While both of these physical phenomena serve to move energy from large to small scales, they are fundamentally different. The development into wave trains is non-dissipative in nature, and in the asymptotic limit of small, but finite amplitude seiches may be described by variants of the Korteweg–de–Vries (KdV) equation. Shear instability, on the other hand yields Kelvin-Helmholtz billows which in turn provide one of the basic archetypes of transition to turbulence, with greatly increased rates of mixing and viscous dissipation. Discussed is how the two phenomena vary as the aspect ratio of the tank and the height of the interface between lighter and denser fluid are changed, finding examples of cases where the two phenomena co-exist. Beginning with an expository set of examples of small amplitude seiches, the process by which a seiche changes from a traditional standing wave to a more complicated small scale set of dynamics is discussed. The results demonstrate that when the initial dimensionless amplitude is small, the seiche takes more than one oscillation period for non–linear effects to become obviously present in the flow. The small amplitude results put into context the cases where the dimensionless amplitude becomes large enough such that non–linear process occur at much earlier times and there is a competition between the formation of wave trains and stratified shear instability. A quantitative accounting for the evolution of the horizontal modewise decomposition of the kinetic energy of the system is presented along with a semi-analytical model of the evolution of the fundamental mode of the seiche. Using two well known methodologies from the literature, the evolution of the mixing dynamics of the seiche is compared from an energetic perspective and a density variability perspective which illustrates a fundamental transition that occurs as the aspect ratio is decreased. Finally, the seiche degeneration and the mixing dynamics are summarized and the most likely future directions of study are highlighted.

Acknowledgements

There are so many people to recognize here. First and foremost, I want to thank my girlfriend Samantha Martinelli for sticking by me throughout this whole process and constantly believing in me. Having you to be a rock in my life made this whole endeavor a whole lot easier. Thanks to my supervisors Marek Stastna and Francis Poulin for the thought provoking discussion and telling me that I'm wrong a lot of the time but it's also okay. Thanks to my lab mates (and extended lab mates) Justin Shaw, Jared Penney, Stan Zonov, Aaron Coutino, Ben Storer, William Xu, Lauren Burnett, Laura Chandler, David Deepwell, Lindsey Daniels and Kris Rowe for helping me to become a productive grad student and making the transition to a new institution an easy one. Also, a big thanks goes out to the Toronto Maple Leafs Fanclub consisting of Andrew Cameron, Bradley Noonan, Bryce Hosking, Jay Henderson, Jonathan Horrocks, Matt Angus and Matt (Cheerios) Slavin. Thanks for giving me a great group of friends to spend my non–academic time with. Another big thanks goes out to my friends that I don't see so often: Sean Davis, Riley Brooks, Ben Arnold and Donovan Allum. I also want to thank my parents for allowing me the opportunity to make it this far and always giving me a strong pair of people to rely upon. Last but certainly not least, I want to thank my cat Boog for being someone I always look forward to seeing at the end of the day and who apparently enjoys seeing me at the end of the day too. He probably can't read this, but I'm sure he gets the point.

Dedication

I dedicate this thesis to every person who has made a positive impact on my life. Thank you.

Table of Contents

List of Tables

List of Figures

Chapter 1

Introduction

1.1 General Introduction

The majority of temperate lakes are density stratified throughout a significant portion of the calendar year [8]. What this means is that natural lakes tend to form into reasonably defined layers of fluid, with the densest fluid deeper in lake and the lighter, less dense fluid sitting on top. While the true interior of a lake is continuously stratified, a reasonable idealization is of two isothermal layers, of thickness h_2 (lower) and h_1 (upper), separated by a sharp interface. This interface provides a wave guide, with a reduced gravity proportional to the density change across the layer. The density change within a lake is typically two orders of magnitude smaller than at the air-water interface and hence waves in the interior, or internal waves, are much larger in amplitude, and slower propagating than waves on the surface. Physical characteristics of internal waves can be affected by a number of external processes. Wind stress on the surface, solar heating and cooling from ice on the surface are some examples. Provided that the along-lake and across-lake length scales are smaller than the Rossby radius of deformation, the rotation of the earth does not play a significant factor in the evolution of fluid flows within the lake and an interesting type of wave phenomena known as a "seiche", or an internal standing wave, can occur. Technically speaking, a seiche *can* occur when the Earth's rotation is non–negligible, but the resulting dynamics are more complicated due to the competition between different large scale waves. Rotational behaviour is not considered here.

A standing wave in general can be understood through the following heuristic example. Imagine a rope or string with both ends clamped down, such as a guitar string. If this string or rope is plucked, there is some restoring force which moves the string back to

its original position. If there is no mechanism to slow this motion, the string overshoots its original position and oscillates. The string only moves up and down and does not propagate left or right because both ends are clamped. This up and down motion is known as a standing wave and a similar phenomena happens within a lake (albeit with differences at the boundaries). Standing waves within lakes and how they change due to different physical phenomena is the subject of this thesis.

1.2 Internal Standing Waves

It has been known since as far back as 1904 [53] that isothermal surfaces (surfaces of constant temperature) in Loch Ness oscillate with a period dependent on physical parameters such as the lake's length and depth. A century of observational work has led to the basic understanding of internal seiches as driven by the wind in the following manner. A sustained period of wind leads to a 'piling up' of water on the downwind side of the lake. While the change in water depth is small, the resulting pressure gradient is large enough so that the compensating displacement of the interior isotherms from their rest height is large (on the order of several meters). When the wind ceases, the sloping internal interface begins to oscillate, yielding large amplitude standing waves [59]. The standing waves created via the above processes break down into propagating wave trains, which in turn transport material and energy.

Internal waves in lakes have been simulated using a variety of numerical models, and at different levels of detail. Basin scale models, for larger lakes especially, typically make the hydrostatic approximation. This is expedient numerically but *a priori* removes short wave dispersion, which is a well known aspect of internal waves, from consideration. Non–hydrostatic modeling of an entire basin is possible, but resolution demands are extreme (see the rightmost column in table 1 of [16]). Layered models based on the classical shallow water equations have no way to remove energy at the smallest scales (i.e. they are derived from the inviscid Euler equations) so various modifications must be made in order to faithfully represent physical phenomena on small scales. In classical hydraulics, the analogy between the shallow water equations and the equations of gas dynamics is often exploited, with the non–linear hyperbolic theory of shocks providing a means to locally dissipate energy. On the lake scale, it is finite wavelength dispersion that is more important to represent. One common method of simulating this phenomenon is to employ a weakly non–hydrostatic correction to the pressure [10, 14, 45, 46]. This allows for a balance between non–linear and dispersive terms that is otherwise impossible in shallow water theory and allows for the development of coherent wave trains, including Kelvin waves in circular domains under

the f–plane approximation. Regardless of the detailed methodology, numerical modeling of lake scale motions requires both parameterizations of physical processes (e.g. energy input from wind) and compromises on physical representation of unresolved scales (e.g. eddy viscosity).

Laboratory experiments provide an alternative means to gain information about internal seiches. In a laboratory setting, a seiche can be generated by stably stratifying a long and narrow tank of water and adiabatically tilting it to some angle. Once any transient wave motion has ceased, the tank can be quickly returned to its original position and a realization of a tilted density interface is created. Since there is no force to balance buoyancy, the density interface begins to oscillate. The energy injected into the system by this action allows for relatively easy manipulation of the seiche amplitude, and hence access to portions of parameter space in which large scale oscillations coexist with smaller scale features such as shear instabilities. A schematic of a basic experiment where a seiche is created is shown in figure 1.1. The meaning of each stage of the evolution of the seiche is described in the caption.

Indeed, in a lake, the interface shape can be much more complicated than the linear tilt in the schematic in figure 1.1. The reason for this is due to spatiotemporal variations in wind forcing and influences of bottom topography and lake shape. For example, Henderson and Deemer [20] shows measurements of temperature and the strength of the stratification from an Acoustic Doppler Profiler in Lacmas Lake in Washington state, USA. Their figure is reproduced in figure 1.2. In figure 1.2(a), lines of the same colour represent isotherms. Clearly, different isotherms do not have the same angle of tilt with respect to the surface, meaning that the influence from the wind at depth is not homogeneous. In figure 1.2(b) is the strength of the stratification, where red is strongly stratified and blue is weakly stratified. Here, there are two regions of relatively strong stratification which could result in complicated wave motion. Figure 1.2 is simply meant to show that isothermal tilts in nature are typically more complicated than what happens in a laboratory, thus the experiments presented in this thesis do not paint an entire picture of what can happen in nature.

1.3 Format of the thesis

In this thesis, high resolution numerical simulations of the evolution of both relatively small and large amplitude internal standing waves are discussed. The simulations are performed at the laboratory scale so as to not have to parameterize small scale processes, but the length of the tank is systematically increased (decreasing the aspect ratio) since

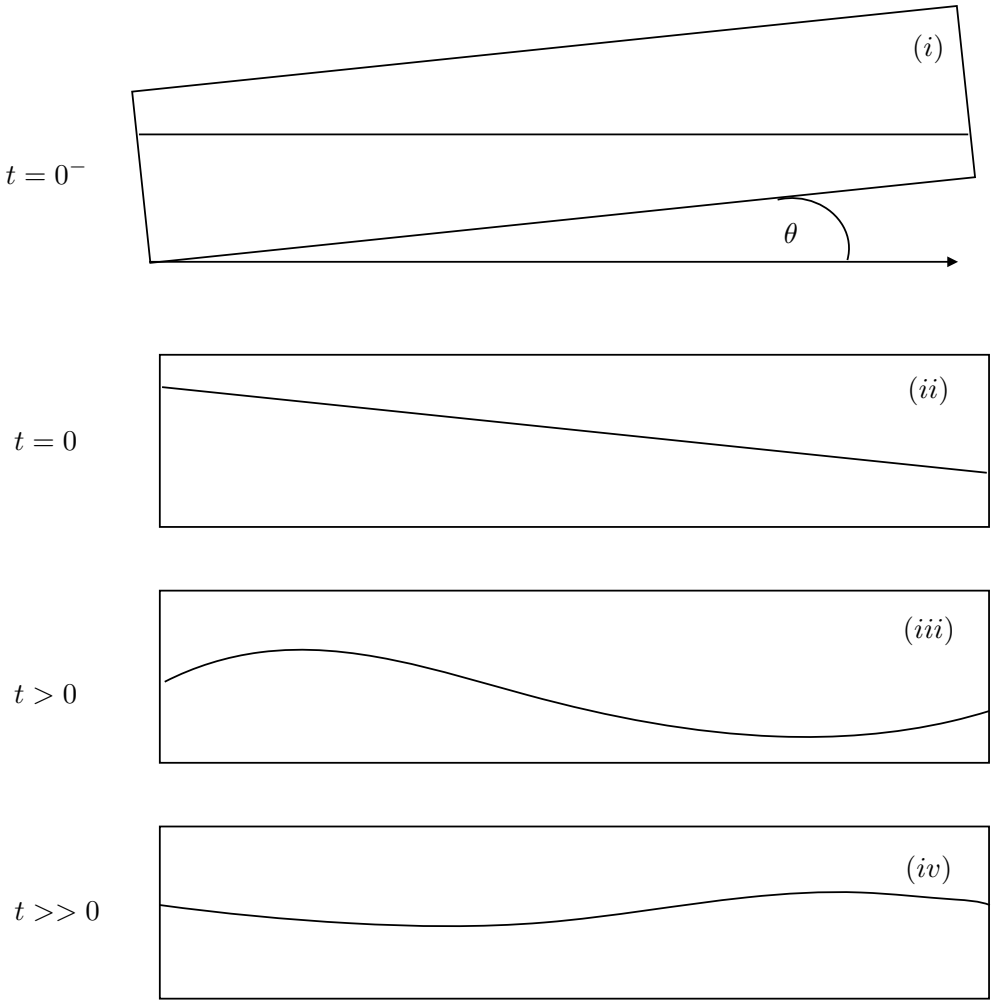

Figure 1.1: Example schematic of how a seiche could be created in a laboratory. First, before the experiment starts, a long and narrow tank is tilted to an angle θ and then filled with a layer of fresh water. Pumped in below this is a layer of salty water, shown in panel (i). The experiment begins when the tank is brought back to the horizontal position and the density interface is tilted instantaneously, shown in panel (ii). The density interface oscillates and different types of wave phenomena may occur under certain conditions as schematized in panel (iii). Finally, at long times, the wave is damped by viscosity and the amplitude becomes smaller over time, shown in panel (iv).

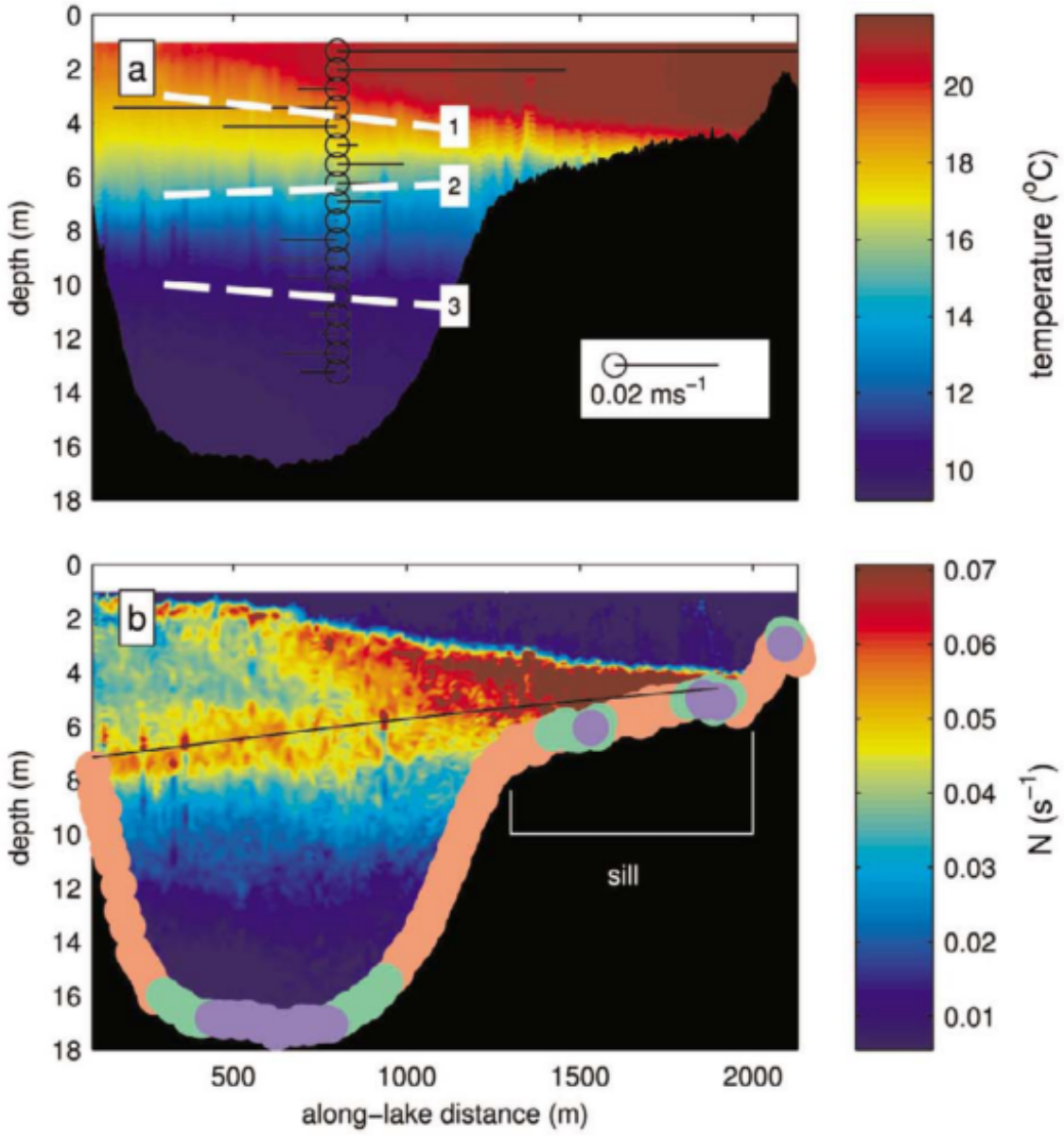

Figure 1.2: Figure 3 from Henderson and Deemer [20] showing temperature measurements in Lacmas Lake, Washington State, U.S.A. Panel (a) shows the temperature field of a cross section of the lake. The angle of the tilt of each the isotherm varies with depth resulting in the possibility of complicated vertical wave propagation. Panel (b) shows the strength of the stratification with circles denoting a measurement of the bed slope.

the disparity between lab dimensions and field scales is large. The primary goals are: i) to present detailed examples of large amplitude wave train formation hitherto unavailable in the literature, ii) to quantify the budget of energy in different horizontal component modes as large amplitude seiches evolve in different combinations of aspect ratio and dimensionless amplitude, iii) to contrast two well known methodologies for quantifying the mixing of stratified fluids as it applies to situations in which wavetrains and shear instabilities coexist.

The remainder of the thesis is organized as follows. Chapter 2 provides the necessary technical background to understand the mathematics and analysis in the results chapter. The equations of motion are discussed, the various ways in which energy is quantified follows and finally, the ways in which fluid mixing is quantified are presented. Chapter 3 contains the main results of the thesis. Chapter 3 begins with the motivation of the results followed by a few words on the software used to simulate the fluid motion. Following this is a discussion of the small amplitude waves and their qualitative evolution with a small discussion of the quantification of the kinetic energy of the system. Following this is a qualitative interpretation of the large amplitude sieches with an in depth quantification of the kinetic energy, potential energy and the mixing. Lastly, chapter 4 contains the conclusions that can be made from the results of chapter 3 as well as provides a qualitative interpretation of the degeneration of the seiches. Finally, chapter 4 concludes with some routes for future work.

Chapter 2

Technical Background

The goal of this chapter is to give an exposition of the technical background required to provide the reader with the necessary understanding of the concepts used for the analysis of the results in chapter 3. This chapter is outlined as follows: first, a brief overview of the idea of the material derivative is given followed by a discussion of the conservation of momentum. Following this, the consequences of the Boussinesq approximation are discussed and the conservation of mass and energy are given. Next, the importance of the stratification of the fluid and some emergent wave phenomena are discussed, relating to linear theory and weakly non–linear theory. Following this is a discussion of energy within the fluid flow in a closed domain, and finally, the last section of this chapter discusses the various ways in which mixing is characterized in this thesis.

2.1 Conservation equations and the Boussinesq approximation

One of the biggest differences between a fluid and a solid is the fact that a fluid cannot support a shear stress without flowing. This brings about the notion of a fluid particle, which is a volume of fluid that can be made arbitrarily small that is able to deform and move under stresses and is associated with the bulk quantities of the fluid, such as pressure, temperature, etc.[51]. Of course, on the molecular level, the notion of the fluid particle fails, but ignoring that limiting case, the fluid particle is a good starting point to quantifying fluid phenomenon. There are two common methods to describe a fluid flow, one being referred to as the Lagrangian interpretation, and the other as the Eulerian interpretation.

The former describes the flow field characteristics as one moves with the fluid particle and the latter describes the flow characteristics at a fixed point in space. For instance, in an experiment, one may decide to use Particle Image Velocimetry (PIV) to characterize a flow, and thus a Lagrangian description would suffice as the particle moves around the field. Alternatively, when performing numerical simulations of geophysical flows, the data is often output as a full field thereby warranting an Eulerian description. Thus, in order to describe information changing with time following a fluid particle in a field, the idea of the material derivative is necessary [24, 33]. If time is represented by t, space represented by the 3D vector $(x(t), y(t), z(t))$, and an arbitrary quantity $X(x(t), y(t), z(t), t)$, the material derivative is defined as

$$\frac{DX}{Dt} = \frac{\partial X}{\partial t} + \boldsymbol{u} \cdot \nabla X \tag{2.1}$$

where (in 3 dimensions) $\boldsymbol{u} = \left(\frac{dx}{dt}\boldsymbol{i} + \frac{dy}{dt}\boldsymbol{j} + \frac{dz}{dt}\boldsymbol{k}\right)$ represents the local velocity field with $\boldsymbol{i}, \boldsymbol{j}, \boldsymbol{k}$ representing unit vectors in the x, y, z directions respectively. Mathematically speaking, the material derivative represents the time rate of change of the quantity X in the velocity field denoted by $\boldsymbol{u}$. The first term in equation (2.1) is known as the unsteady term which provides information on how the local field is changing with time while the second term, called the advective term, gives information on the rate at which X changes as a particle moves from one place to another. Often, the material derivative can be thought of as simply the rate of change of the quantity X when following a fluid particle. The notion of the material derivative becomes important when talking about the conservation laws that a fluid must obey. For instance, in order for momentum to be conserved, the statement of Newton's second law for a fluid with density ρ and velocity $\boldsymbol{u}$ is given in Kundu et al. [24] as

$$\rho \frac{D\boldsymbol{u}}{Dt} = \rho \boldsymbol{g} + \nabla \cdot \boldsymbol{\tau} \tag{2.2}$$

where $\boldsymbol{g}$ is the body force on the fluid (gravity in this case) and $\boldsymbol{\tau}$ is the stress tensor of the fluid particle representing the forces due to neighbours unique to a continuum. The fundamental non–linearity comes from the advective term within the material derivative of the velocity, $\boldsymbol{u} \cdot \nabla \boldsymbol{u}$. Buoyancy effects due to gravity and variations in the mass of the fluid are denoted by $\rho \boldsymbol{g}$.

The tangential and normal stresses on a fluid particle are encapsulated in the stress tensor, $\boldsymbol{\tau}$, which has units of $force/area$. The physical significance of the stress tensor is better understood through its components, τ_{ij}. τ_{ij} is the ith component of stress on a surface element which has normal $\hat{\boldsymbol{n}}$ pointing in the jth direction[1] where i and j can both

take on values of 1, 2 and 3 corresponding to the x, y, z directions respectively in Cartesian coordinates. The tensor representation itself is coordinate free.

The stress tensor can be decomposed as follows

$$\tau_{ij} = -P\delta_{ij} + \sigma_{ij}. \tag{2.3}$$

In equation (2.3), $-P\delta_{ij}$ represents the isotropic stress on a fluid element and σ_{ij} represents all other forces due to neighbours, known as the deviatoric stress tensor. In particular σ_{ij} contains all the shear forces. Here, P is the thermodynamic pressure, and δ_{ij} is a Kronecker delta [24, 3]. For ease of manipulation, vector notation will be used for the remainder of the derivation with the stress tensor denoted in bold.

Rewriting equation (2.2) using the decomposition in equation (2.3), the conservation of momentum is

$$\rho\frac{D\boldsymbol{u}}{Dt} = -\nabla P + \rho\boldsymbol{g} + \nabla\cdot\boldsymbol{\sigma}. \tag{2.4}$$

For a moment, assume that the fluid is completely stationary, meaning $\boldsymbol{u} = 0$, and hence $\boldsymbol{\sigma} = 0$. Equation (2.4) reduces to

$$\nabla P = \rho\boldsymbol{g} \tag{2.5}$$

The density field can be broken up into a constant reference density plus a stratification term that varies in z only, as

$$\rho = \rho_0(1 + \bar{\rho}(z)) \tag{2.6}$$

with the added assumption that $\bar{\rho}(z) \ll 1$. Gravity can be written as $-g\boldsymbol{k}$ and the resulting pressure distribution is thus governed by

$$\frac{dp^H}{dz} = -\rho_0 g(1 + \bar{\rho}(z)). \tag{2.7}$$

p^H is the *hydrostatic* contribution to the pressure and balances the weight of the overlying fluid. However, if the fluid undergoes some motion, a *non–hydrostatic* pressure can be defined, p. Therefore, the total pressure is the sum of the hydrostatic and the non–hydrostatic pressures written as

$$P = p^H + p. \tag{2.8}$$

For the density field to induce any motion, there must be an added perturbation $\rho'(x, y, z, t)$. The total density of the fluid is then

$$\rho = \rho_0(1 + \bar{\rho}(z) + \rho'(x, y, z, t)). \tag{2.9}$$

Using the above decomposition of the density on the second term on the right of equation (2.4) gives

$$\rho \frac{D\boldsymbol{u}}{Dt} = -\frac{dp^H}{dz}\boldsymbol{k} - \nabla p - \rho_0(1+\bar{\rho}(z))g\boldsymbol{k} - \rho_0\rho' g\boldsymbol{k} + \nabla\cdot\boldsymbol{\sigma} \tag{2.10}$$

Of course, equation (2.7) can be used to simplify the above equation leaving

$$\rho \frac{D\boldsymbol{u}}{Dt} = -\nabla p - \rho_0\rho' g\boldsymbol{k} + \nabla\cdot\boldsymbol{\sigma}. \tag{2.11}$$

Equation (2.11) represents the momentum balance of a small fluid particle subject to a non–hydrostatic pressure force, buoyancy due to a density perturbation, and tangential stresses within fluid due to motion. Note that the pressure p contains a small component due to the weight of the overlying density perturbations. The above equation will be simplified even further when subjected to the Boussinesq approximation discussed as follows.

The Boussinesq approximation finds wide use in published literature as it performs remarkably well in many cases [48, 15, 12, 36, 13, 4, 47]. The particular details of the Boussinesq approximation are left to resources external to this thesis such as Spiegel and Veronis [44], Batchelor [3], Tritton [51], and Kundu et al. [24] as the details themselves are not important to the main results of this thesis. However, some of the results of the Boussinesq approximation are discussed here. In order for the Boussinesq approximation to be internally consistent and to yield reasonable results, some important points must be kept in mind.

The first is that density changes within the fluid must be small with respect to the reference density of the fluid. This notion is consistent with the approximation made in equation (2.9). By ensuring that the density differences within the fluid are small, the conservation of mass equation [24, 51] of a fluid particle can be written as (with approximate equality being understood)

$$\nabla\cdot\boldsymbol{u} = 0. \tag{2.12}$$

This is known as the incompressibility condition and is the full (no approximation) conservation of mass equation written in its constant density form. Thus, equation (2.12) actually says that fluid particles retain their volume to leading order.

The next restriction of the Boussinesq approximation is that density changes are due to temperature variations (or salinity in relevant cases) but never pressure [24, 51, 44]. This idea comes from the discussion in Kundu et al. [24] which shows that density changes due to pressure occur when the vertical scales of the motion under consideration are comparable to any vertical "scale heights" in the problem. Take for example the e–folding height of an isothermal atmosphere, RT/g [24]. As an example, this height works out to about 10 km

for air. Another situation where the pressure dependence of the density might be expected is in a very deep lake, such as Lake Baikal [9] which has a maximum depth of about 1600 m [54] . A deep lake such as Baikal can thermobarically stratified, which means the water density is both a function of the temperature *and* pressure [8]. To avoid stratification due to pressure, the vertical excursions of the motion of interest must therefore be smaller than the scale heights of the problem [24, 44].

The final restriction of the Boussinesq approximation is that flow speeds must be slow compared to the speed of sound within the medium in which the oscillations occur. The Mach number, U/c, where U is a characteristic flow speed and c is the speed of sound in the medium, must be below about 0.3 for the validity of the Boussinesq approximation. This is typically a safe approximation due to the fact that the speed of sound in water is about 1470 m/s and flow speeds are much slower than this [24, 51].

With an understanding of the assumptions behind the Boussinesq approximation in hand, the conservation of mass, momentum and energy can be simplified. The Boussinesq approximation allows for the conservation of mass to be written as equation (2.12) and is discussed in detail in Kundu et al. [24], Tritton [51] and Batchelor [3]. Next, simplifications to the conservation of momentum can be made. The first simplification, which is actually not part of the Boussinesq approximation, is made by using the constitutive equation for a Newtonian incompressible fluid given Kundu et al. [24] to rewrite the divergence of the deviatoric stress tensor as

$$\nabla \cdot \boldsymbol{\sigma} = \mu \nabla^2 \boldsymbol{u}. \tag{2.13}$$

The second simplification comes from using the decomposition for density in equation (2.9) on the lefthand side of equation (2.11). This simplifies the left hand side to

$$\rho_0(1 + \bar{\rho}(z) + \rho'(x, y, z, t))\frac{D\boldsymbol{u}}{Dt} \approx \rho_0 \frac{D\boldsymbol{u}}{Dt}. \tag{2.14}$$

because $1 \gg \bar{\rho}(z) \gg \rho'(x, y, z, t)$.

Thus, the equation for conservation of momentum for a Boussinesq fluid after dividing by the reference density is

$$\frac{D\boldsymbol{u}}{Dt} = -\frac{1}{\rho_0}\nabla p - \rho' g\boldsymbol{k} + \nu \nabla^2 \boldsymbol{u}. \tag{2.15}$$

where $\nu = \mu/\rho_0$ is the kinematic viscosity.

The last conservation law that is simplified using the Boussinesq approximation is the

conservation of energy. This can be shown using the internal energy equation [24]

$$\rho \frac{De}{Dt} = -\nabla \cdot \boldsymbol{q} + P(\nabla \cdot \boldsymbol{u}) + \epsilon. \tag{2.16}$$

Here, e is the internal energy, ρ is the full density field of the fluid, q is the heat within the fluid, p is the thermodynamic pressure and ϵ is the viscous dissipation. The first term on the righthand side of equation (2.16) represents the convergence of heat within the fluid, the second term represents pressure work, and the third term represents viscous dissipation due to fluid friction. In essence, allowing for a Fourier–like heat diffusion law, and modeling the fluid as an ideal gas, and arguing that viscous dissipation makes only small contributions to the internal energy, equation (2.16) can be reformulated as

$$\frac{D\rho}{Dt} = \kappa \nabla^2 \rho \tag{2.17}$$

where κ is the diffusivity of heat. The details of how one goes from equation (2.16) to equation (2.17) are shown in Kundu et al. [24], Tritton [51] and Spiegel and Veronis [44].

For completeness, the equations of motion governing a Boussinesq fluid in this thesis are summarized here as follows:

$$\frac{D\boldsymbol{u}}{Dt} = -\frac{1}{\rho_0}\nabla p - \rho' g \boldsymbol{k} + \nu \nabla^2 \boldsymbol{u}, \tag{2.18}$$

$$\frac{D\rho}{Dt} = \kappa \nabla^2 \rho, \tag{2.19}$$

$$\nabla \cdot \boldsymbol{u} = 0. \tag{2.20}$$

Equation (2.18) represents conservation of momentum, equation (2.19) represents conservation of energy, and equation (2.20) represents conservation of mass.

2.2 Stratification

Often in geophysical contexts, especially in a limnic setting in the summer season, the fluid is density stratified and this stratification is integral to wave motion within the fluid. The density difference in a Boussinesq fluid (a fluid subject to the Boussinesq approximation and the incompressibility condition) can only vary by a few percentage points which contrasts with the surface of a body of water where the stratification is effectively a step function due to the large difference between the densities of air and water. Thus the inherent differences

between an internal stratification and a surface stratification allow for the development of differing wave phenomena. For example, a common sight on the surface of natural bodies of water are fast waves with small amplitudes. Conversely, the wave activity within the fluid is slower (and harder to visualize) and exhibits slightly different attributes such as larger amplitudes and slower wave velocities.

2.2.1 Derivation of linear internal wave equation with discussion of a standing wave

As first step, this section discusses the concept of a standing wave in terms of an ideal type of stratification, called a *linear stratification*. The reason this problem is discussed is due to its analytical tractability as well as the insight one can gain from the results. Fluids in limnic and coastal oceanic settings are typically not linearly stratified, but this stratification is nevertheless, a good starting point. Beginning with the 2D inviscid Euler equations which are equations (2.18),(2.19) and (2.20) but ignoring thermal diffusion and viscosity, and assuming homogeneity in the y direction and no rotation, the equations of motion are as follows, with subscripts denoting partial derivatives:

$$u_t + uu_x + wu_z = -\frac{1}{\rho_0}p_x, \tag{2.21}$$

$$w_t + uw_x + ww_z = -\frac{1}{\rho_0}p_z - \rho' g, \tag{2.22}$$

$$u_x + w_z = 0, \tag{2.23}$$

$$\rho_t + u\rho_x + w\rho_z = 0. \tag{2.24}$$

Equations (2.21) – (2.24) provide a closed system of four coupled PDEs in four variables (u, w, ρ, p). The density field in the fourth equation must be decomposed using equation (2.9) in 2D,

$$\rho(x, z, t) = \rho_0(1 + \bar{\rho}(z) + \rho'(x, z, t)), \tag{2.25}$$

with the same assumption that $\rho'(x, z, t) \ll \bar{\rho}(z) \ll 1$.

Applying the simplification in equation (2.25) to equation (2.24) gives:

$$\rho'_t + u\rho'_x + w\rho'_z + w\bar{\rho}_z(z) = 0 \tag{2.26}$$

The next step is to linearize about a state of rest due to the fact that the velocities are

assumed to be small deviations from the rest state. This restriction must be made to justify the removal of the non–linear terms in equations (2.21) and (2.22). Using this assumption in tandem with the decomposition of the density field, the $u\rho'_x$ and $w\rho'_z$ terms in equation (2.24) can also be ignored. Note that the $w\bar{\rho}_z(z)$ term in equation (2.24) cannot be removed as $\bar{\rho}$ cannot be considered small with respect to the remaining terms. The following set of equations remain:

$$u_t + \frac{1}{\rho_0} p_x = 0, \tag{2.27}$$

$$w_t + \frac{1}{\rho_0} p_z + \rho' g = 0, \tag{2.28}$$

$$u_x + w_z = 0, \tag{2.29}$$

$$\rho'_t + w\bar{\rho}_z(z) = 0. \tag{2.30}$$

At this stage, the system above gives some important insights into the motion. From equations (2.27) and (2.29), changes in the horizontal velocity are due the horizontal pressure gradient and the vertical convergence of fluid respectively. As well, the vertical velocity in equation (2.28) changes due to vertical pressure gradients, and gravity. Finally, the wave motion that is of interest, the time rate of change of the perturbation to the density field, is a result of the vertical advection of the background density field.

To further simplify the above system of equations the pressure terms must be removed somehow. The reason for doing this is that there is no explicit equation for pressure as there is for ρ', u and w. This can be performed by taking the z derivative of equation (2.27) and the x derivative of equation (2.28) and then computing the difference. This gives the following equation:

$$(u_z - w_x)_t = \rho'_x g. \tag{2.31}$$

The term on the left hand side of the above equation is simply the time derivative of the y component of what is known as vorticity. Vorticity is defined as $\boldsymbol{\omega} = \nabla \times \boldsymbol{u}$ and can be thought of as a measure of the local rotation of fluid particles. The above equation reveals that horizontal variations in the density field induce span–wise vorticity, meaning that horizontal density gradients induce a torque on individual fluid particles thus inducing rotation of them.

Upon taking the time derivative of equation (2.31) and the x derivative of equation (2.30), some algebra reveals

$$(u_z - w_x)_{tt} = -w_x \bar{\rho}_z g. \tag{2.32}$$

The above equation still has 2 unknowns, u and w. One of these can be eliminated by taking the x derivative of the entire equation and utilizing the incompressibility condition which allows the entire equation to be written in terms of a stream function, ψ:

$$\nabla^2 \psi_{tt} - \frac{d\bar{\rho}}{dz}\psi_{xx} g = 0 \tag{2.33}$$

where $u = \psi_z$ and $w = -\psi_x$. The stream function guarantees that the velocity field satisfies equation (2.29) and a stream function can be defined whenever (2.29) is valid [24].

Next, an important quantity known as buoyancy frequency, or the *Brunt–Väisälä frequency* is defined. The squared buoyancy frequency is defined as

$$N^2(z) = -g\frac{d\bar{\rho}}{dz}. \tag{2.34}$$

N is interpreted as the frequency of oscillation of a displaced fluid particle in the absence of friction within the fluid [24, 33]. With this definition, the internal wave equation in terms of a stream function is

$$\nabla^2 \psi_{tt} + N^2(z)\psi_{xx} = 0. \tag{2.35}$$

Equation (2.35) is a fourth order PDE requiring two initial conditions, two boundary conditions in z, and two boundary conditions in x. However if solutions of a particular form are sought, certain symmetries of the problem can be exploited to simplify the boundary and initial conditions. In a horizontally unbounded domain for instance, the solution of interest is that of a traveling wave in the horizontal with some undetermined structure in the vertical denoted by ϕ. Mathematically, this is

$$\psi = \exp\left[i(kx - \sigma t)\right]\phi(z). \tag{2.36}$$

By making a choice of solution of this form, only the vertical boundary conditions are of interest. For the moment, the boundary conditions are no normal flow through the upper and lower walls. In terms of the fluid velocities, this is $w(x, 0) = w(x, H) = 0$ and in terms of the stream function, the vertical boundary conditions are $\psi_x(x, 0) = \psi_x(x, H) = 0$. More of a discussion on boundary conditions is saved for later in this chapter and in chapter 3.

Of direct interest to the results of this thesis are results based not on a traveling wave, but on a standing wave due to the fact that the domain is horizontally bounded (one with vertical walls at $x = 0, L$). Leaving both the vertical and horizontal structure undetermined for now, and keeping with the notion of the vertical structure function, the stream function

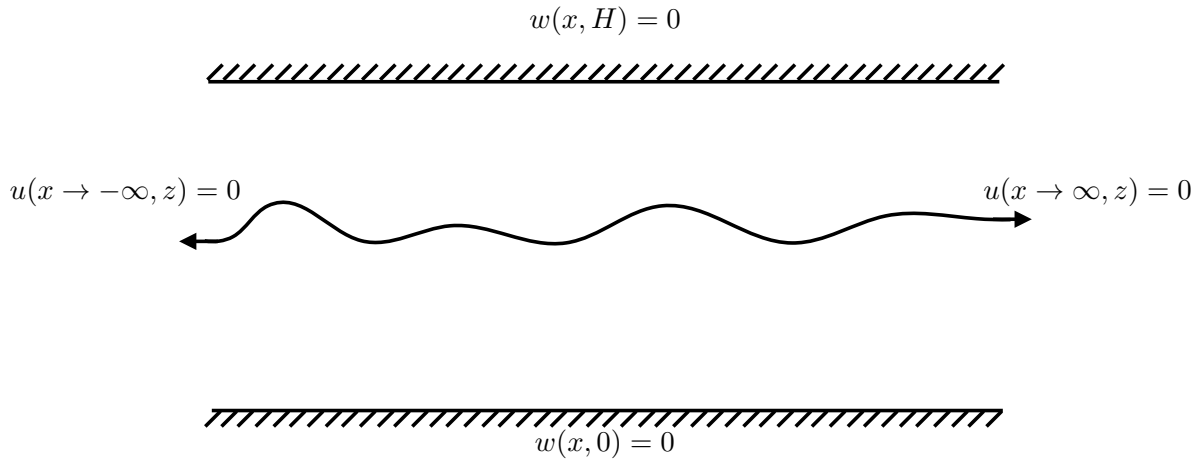

Figure 2.1: Schematic of the pycnocline and the boundary conditions that must be satisfied for a horizontally unbounded flow. Typically the pycnocline has finite thickness but is simply represented as curve here for clarity. Since the domain is unbounded in the horizontal direction, the horizontal wavenumber, k, can take on any real value. Since there are walls at the upper and lower bounds of the domain, the vertical wavenumber can only take on discrete values.

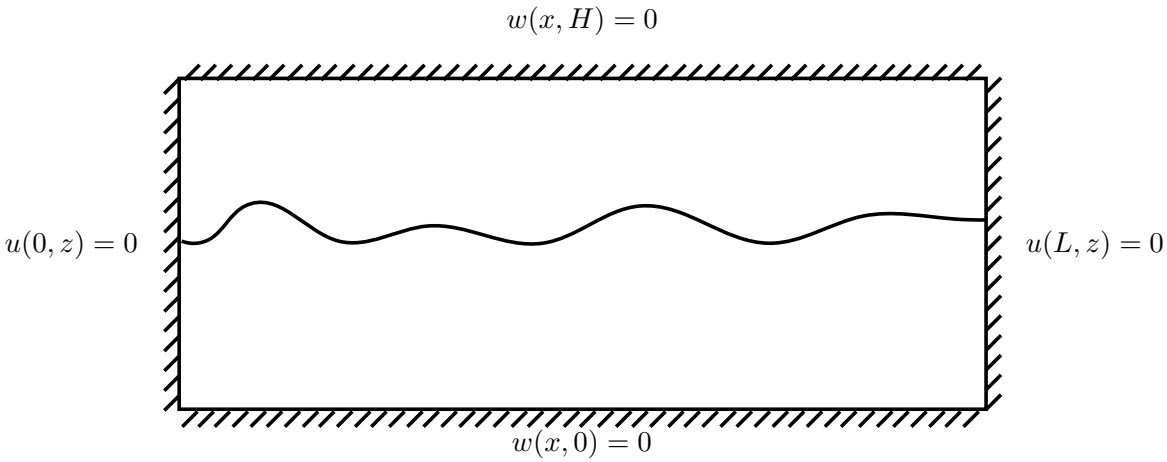

Figure 2.2: As in figure 2.1 but for a horizontally bounded domain. Since the domain is bounded in the horizontal direction, the horizontal wavenumber, k, can only take on discrete values. Since there are walls at the upper and lower bounds of the domain, the vertical wavenumber can only take on discrete values.

can be written as

$$\psi = \phi(z) f(x) \cos(\sigma t). \tag{2.37}$$

In the horizontally bounded domain of interest, the boundary conditions on the vertical walls at $x = 0, L$ are no normal flow conditions, meaning $\psi_z(0, z) = \psi_z(L, z) = 0$. Substituting the above ansatz into (2.35) and invoking the boundary conditions and disallowing $\phi(z) = 0$ and $\phi_z(z) = 0$ forces

$$f(x) = \sin(kx). \tag{2.38}$$

In order to satisfy the boundary conditions at the vertical walls, k must be quantized as

$$k = \frac{n\pi}{L} \tag{2.39}$$

where n is a positive, non–zero integer. To contrast, in a horizontally unbounded domain, k can take any value and is considered a continuous variable.

After substitution of the known standing wave solution above and some rearranging, equation (2.35) yields what is known as the Taylor–Goldstein, or T-G, equation (technically the T-G equation without a shear current).

$$\phi_{zz} + \frac{k^2}{\sigma^2}\left(N^2(z) - \sigma^2\right)\phi = 0 \tag{2.40}$$

$$\phi(0) = \phi(H) = 0 \tag{2.41}$$

In order to have bounded solutions to equation (2.40), the frequency of oscillation of the wave must be lower than the maximum of the buoyancy frequency, else the trial solutions become exponential and in character and the boundary conditions cannot be satisfied. The problem posed by equations (2.40) and (2.41) describes the behaviour of the vertical structure of a small amplitude internal wave with arbitrary stratification [1, 24]. This problem is also an example of a classical Sturm–Liouville eigenvalue problem [18], thus much can be predicted about the solutions of the problem. Because of the known properties of a Sturm–Liouville boundary value problem, the set of these modes is linearly independent and complete, meaning any smooth flow can be represented by projecting onto these modes. Whether such flows are stable to perturbations is the subject of linear stability problems [1, 24], and beyond the scope of the present work. What is also known is that there is a lowest eigenvalue and no highest eigenvalue. In the present context, the eigenvalues are either the allowed frequencies with the wavenumber specified, or the wavenumbers with the frequency specified. In the case with sidewalls it is the quantized k_n that is taken as given and the resulting σ yield the dispersion relation (the relationship between the frequency of oscillation and wavenumber). This means that there is a lowest frequency as well as a highest frequency.

Since the buoyancy frequency determines the stratification, the linearly stratified case is labelled as such because the background density profile reads

$$\bar{\rho}(z) = -\frac{\Delta\rho}{H}z + \frac{\Delta\rho}{2} \tag{2.42}$$

so that the constant buoyancy frequency is given by

$$N^2(z) = \frac{g\Delta\rho}{H}. \tag{2.43}$$

$\Delta\rho$ is the total density difference as a percentage of the background ρ_0, g is gravity, and H is the total depth of the fluid. Thus, the Taylor–Goldstein equation is a simple ODE with a known solution

$$\phi(z) = \sin\left(\frac{m\pi z}{H}\right) \tag{2.44}$$

with m being an integer, also known as the vertical mode number.

Substitution of the expression for ϕ back into the equation for the vertical structure while letting the horizontal wavenumber $k = n\pi/L$ take on discrete values gives

$$\sigma^2(k) = \frac{N^2 \frac{n^2\pi^2}{L^2}}{\frac{n^2\pi^2}{L^2} + \frac{m^2\pi^2}{H^2}}. \tag{2.45}$$

Thus the frequency of different horizontal and vertical modes can only take on discrete frequencies. If the domain were to be horizontally unbounded, only the vertical frequencies would be quantized. From the expression above for σ, the period of oscillation of a linear internal standing wave is

$$T_{linear} = \frac{2\pi}{\sigma}, \tag{2.46}$$

which when simplified by letting $n = 1$ and $m = 1$ (the fundamental horizontal mode) is

$$T_{linear} = 2\pi\sqrt{\frac{L^2 + H^2}{\Delta\rho g H}}. \tag{2.47}$$

This oscillation period is of fundamental importance because it is the period of oscillation of the longest wavelength mode and thus sets the longest time scale as to which internal wave processes can occur.

The above discussion gives some important insights into the motion of an internal standing wave under idealized conditions. However, a linear stratification, as previously mentioned, is rarely seen in limnic and coastal settings. Thus, in equation (2.48) a model of the density field that is often found in geophysical settings is presented. This stratification is plotted in figure 2.3(i), the buoyancy frequency is shown in figure 2.3(ii), and the first four vertical modes of(2.40) and (2.41) are plotted in figure 2.3(iii).

$$\rho = \rho_0 \left(1 - \frac{\Delta\rho}{2} \tanh\left(\frac{z - z_0}{h}\right)\right). \tag{2.48}$$

Note the above differences in the structure of the above equation, the density difference is again given by $\Delta\rho$, the height of the center of the pycnocline is given by z_0, and the halfwidth of the pycnocline is given by h.

The important point shown in figure 2.3(i) is that there is an upper layer and a lower layer each having an approximately constant density with a transition region (the pycnocline) in between. In the linearly stratified case (not shown), there is neither a transition region nor any well defined layers, thus the motion discussed in the linear case should be

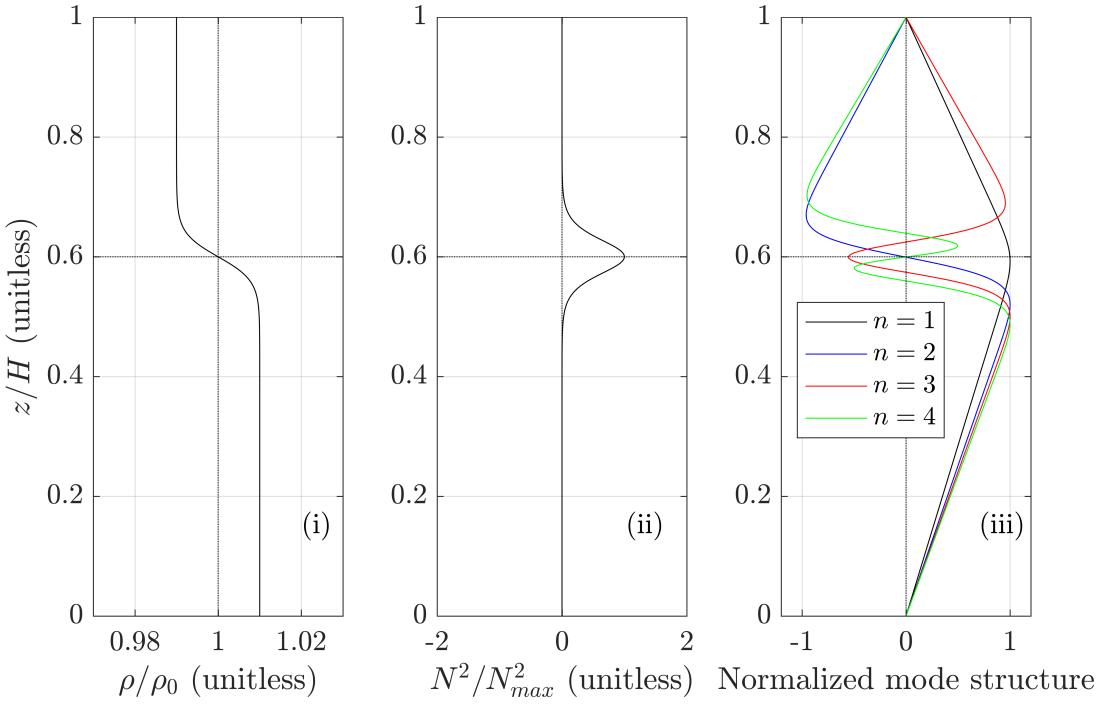

Figure 2.3: Panel (i) shows the background stratification in equation (2.48) with $z_0/H = 0.6$, $h/H = 0.04$, $\Delta\rho = 0.02$. H is the total depth. Panel (ii) shows the buoyancy frequency, $N^2(z)$, of the fluid. Finally, panel (iii) is the first four vertical modes from equation (2.40) normalized by their maximums.

considered a unique case of internal wave motion. It is also important to keep in mind that the stratification in equation (2.3) is a simplification of what can happen in nature, but is much more representative than the linear stratification [28, 6, 8, 41, 40, 20]. A detailed discussion as to what causes the stratification to take this form is not necessary, but a few words would help give some context. A number of factors determine the hyperbolic tangent structure of the stratification such as solar and wind forcing, the presence of ice, seasonal overturns, wind and depth of the body of water. A body a water can be stratified by one or more factors such as differences in temperature, salinity, other dissolved substances, oxygen content or biological material [8, 9]. Since many lakes undergo seasonal changes in their stratification[8], this vertical structure in the stratification is especially prevalent in early summer into fall before fall overturns. For the purposes of this thesis, it is sufficient to begin with a stratification similar to equation (2.48).

Looking at figure 2.3(iii), it is clear that all the highest spatial variation in the modes is near the pycnocline suggesting the largest vertical variation in the wave is near there. Observations in the field suggest that this is certainly the case [28] with higher vertical modes having much of their variation near to the pycnocline while the lower modes vary slowly over the entire water column. Since vertical mode–1 waves typically contain most of the energy in the flow, they are the most common to be documented. However, in some situations, vertical mode–2 waves can be present in the same flow. Maxworthy et al. [32] showed that vertical mode–2 waves can appear as a result of energy redistribution from a shoaling Kelvin wave in Lake Biwa. This mechanism was then demonstrated in the laboratory. Maxworthy et al. [32] suggested that the generation of vertical mode–2 waves is a result of the energy cascade from the largest scales where it is introduced to where it is ultimately dissipated at very small length scales. What they also saw was that these vertical mode–2 waves has smaller amplitudes and wavelengths than their mode–1 counterparts. Boegman et al. [6] added that the shoaling of these waves energizes the bottom boundary layer further contributing to dissipation at the smallest scales.

It is also possible to explore the dependence of the mode structure on the horizontal length scales in equation (2.40) through k which is shown in figure 2.4. Here, the first vertical mode is shown to change as k is varied. The value that k takes on in each curve in figure 2.4 are arbitrary and were chosen to highlight the fact that as k increases (wavelength decreases), the vertical modes localize near the pycnocline suggesting that shorter waves have a weaker influence away from the pycnocline and that longer waves have a greater influence away from the pycnocline. For reference as to where the stratification is the strongest, the buoyancy frequency is plotted.

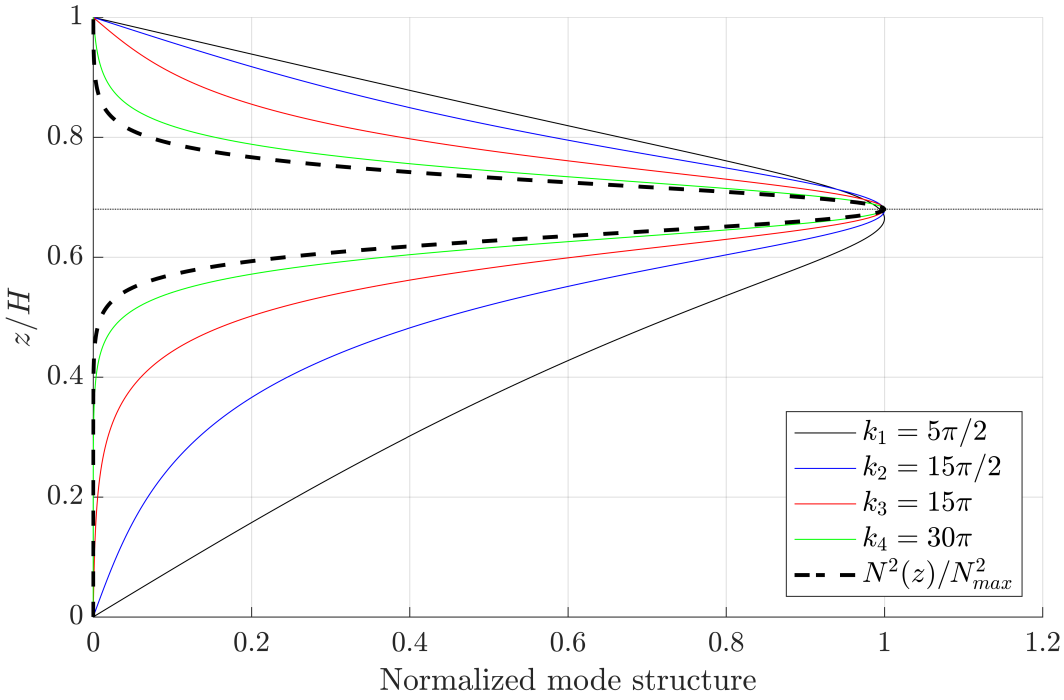

Figure 2.4: The first eigenvector of equation (2.40) (first vertical mode) with varying k. The buoyancy frequency is plotted for reference.

2.2.2 Emergent Wave Phenomena

The derivation of the linear theory above determines the vertical structure of a standing wave with the vertical structure given by $\phi(z)$. Due to the linearity of the stratification, a test solution can be found which yields useful information about the wave. As the name suggests, linear theories remove any possibility for non–linear interactions, meaning that a wave predicted by linear theory cannot possibly undergo any process that is non–linear in nature (e.g. steepening). However, because the governing equations (equations (2.18), (2.19) and (2.20)) contain a quadratic non–linearity, it is possible that at some point in the wave's evolution, non–linear effects might become important. Thus, linear internal waves are simply an idealized example of wave phenomena. Fully non–linear equations present certain mathematical difficulties, so instead, theories based on weak non–linearities are often of interest because of the analytical tractability and the ability to predict more realistic motion under certain conditions.

The simplest theory which accounts for non–linear effects and the effects of finite wavelength (dispersion) is termed Eulerian weakly non–linear theory (henceforth WNL). Its derivation begins from the inviscid, stratified Euler Equations. Using perturbation theory, one can build a theory based upon unidirectional propagating waves to first order. One of the fundamental assumptions is the fact that these waves have a much longer wavelength than amplitude, or in other words, their aspect ratio is very small. WNL gives the Korteweg–de–Vries, or KdV, equation [23, 5, 34, 19] for the horizontal and temporal structure of the isopycnal displacement. In the two-layer situation, this specifies the interface displacement η as, and the coefficients in the KdV equation may be given as closed form formulae:

$$\eta_t + c_0\eta_x + \alpha\eta\eta_x + \beta\eta_{xxx} = 0. \tag{2.49}$$

where

$$c_0 = \sqrt{\frac{\Delta\rho g z_0(H - z_0)}{H}}, \tag{2.50}$$

$$\alpha = \frac{3}{2}c_0(H - 2z_0)/z_0(H - z_0), \tag{2.51}$$

and

$$\beta = c_0 z_0(H - z_0)/6. \tag{2.52}$$

Note that $\beta > 0$ while α can take on either sign. While the KdV equation can be solved as an initial value problem, waves of permanent form, or solitary waves are of fundamental

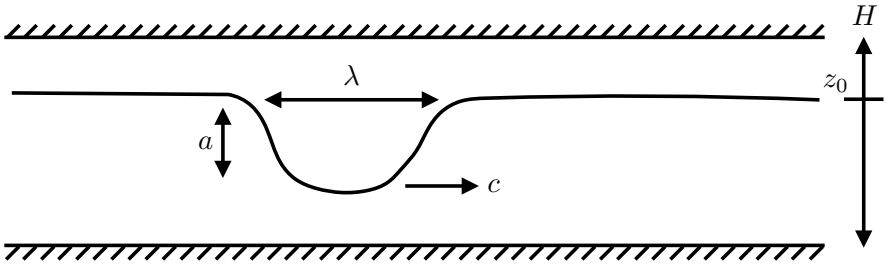

Figure 2.5: A schematic of a solitary wave. The wave and the energy associated with it propagates with a speed of c with amplitude a and wavelength λ.

interest. They have the form

$$\eta(x,t) = a\,\mathrm{sech}^2\left(\frac{x-ct}{\lambda}\right) \tag{2.53}$$

where $c = c_0 + \frac{1}{3}\alpha a$ is the non–linear phase speed and $\lambda = \sqrt{12\frac{\beta}{a\alpha}}$ is the wavelength. A schematic of a solitary wave of the form of equation (2.53) is presented in figure 2.5 [19].

An understanding of the mechanisms that equation (2.49) represents can be demonstrated by looking at each independently. Following the derivation in Benney [5], ignoring non–linear effects and dispersion (letting $\alpha, \beta = 0$), solutions of equation (2.49) are waves of permanent form that propagate at a fixed speed and satisfy a unidirectional wave equation:

$$\eta_t = -c_0\eta_x. \tag{2.54}$$

At the first order in the amplitude parameter, the non–linear term in equation (2.49) appears. Factoring the η_x term out, the non–dispersive version of equation (2.49) can be written as

$$\eta_t = -(c_0 + \alpha\eta)\eta_x. \tag{2.55}$$

The above equation can be interpreted as an advection equation similar to equation (2.54)

except that the speed that the wave propagates at now depends on the amplitude of the wave itself. This phenomenon is termed *steepening* with the sign of α determining the polarity of the wave via the observations that larger waves propagate faster. If $\alpha > 0$, the waves are known as waves of elevation and if $\alpha < 0$, the waves are known as waves of depression. Physically speaking, the sign of α is determined by the difference of the layer depths. If the upper layer depth is larger than the lower layer depth, then $\alpha > 0$, and conversely, if the lower layer depth is larger, $\alpha < 0$.

The evolution of the waves predicted by this equation is that to first order, the wave propagates rightward with permanent form, except that the peak of the wave propagates slightly faster than the rest of the wave. This results in steepening of the deflection of the interface and an increase in the energy density associated with the wave. If this process happens quickly, then the wave will break and the behaviour can no longer be predicted by the above equation.

This problem is potentially fixed by adding in the dispersive term. The effects of this term can be seen by linearizing equation (2.49):

$$\eta_t = -c_0\eta_x - \beta\eta_{xxx}. \tag{2.56}$$

Looking at the definition of β (which is greater than zero), one can see that the dispersion mechanism is strongest when the layer depths are equal. In the current form of the above equation, the third derivative is difficult to interpret. This can be made easier by looking at this equation in Fourier space. Upon taking a Fourier transform of the above equation and factoring out some common terms, one arrives at the following equation for the Fourier transformed deflection, $\hat{\eta}$:

$$\hat{\eta}_t = ik(c_0 - \beta k^2)\hat{\eta}. \tag{2.57}$$

where we note $\beta > 0$. Some insight on the motion can be obtained by comparing to the Fourier transformed advection equation (2.54) to get

$$\hat{\eta}_t = ikc_0\hat{\eta}. \tag{2.58}$$

It is known that waves that satisfy the advection equation travel at speed c_0, so the comparison to be made is that the dispersive in equation (2.49) term changes the speed of the wave depending on its wavenumber (c_0 goes to $c_0 - \beta k^2$). Thus, as the wavenumber increases (smaller wavelengths), the wave speed will decrease resulting in dispersion. However, at a certain point, this theory predicts waves with large enough wavenumber will propagate leftward which goes against the fundamental assumption of rightward propagating waves. Thus, KDV theory is truly an approximation of the motion associated with

only long waves. With steepening and dispersion taken together, the balances between the nonlinear and dispersive terms create a rank ordered wave train of solitary waves from a general initial condition. The number, amplitude, and wavelength of these rank ordered waves may be determined via inverse scattering theory (not done here)[55].

Waves of the form of equation (2.53) are known in the literature as solitary waves. Solitary waves represent a significant topic in the environmental fluid mechanics literature as they are a common feature in the coastal ocean and especially in lakes. The reason these waves are important in a limnic setting is because they effectively move material and energy around a lake as they propagate. Their significance will become apparent in the results presented in chapter 3.

2.3 Energetics

In the following section, both the concepts related to the kinetic energy (hereafter referred to as KE) and potential energy (hereafter referred to as PE) will be introduced separately. The buoyancy force performs work on the fluid which converts PE to KE. The change in the form of the energy is what is responsible for the oscillation of the density interface. Generally speaking, instead of the energy in a fluid, it is common in the literature to talk about energy density in a fluid, or the energy per unit volume (or area in 2D). Though they are different quantities, unless specifically noted, the terms energy and energy density are used interchangeably.

First the KE is discussed in physical space and an equivalent representation in wave number space is derived. Next, the concept of PE is introduced followed by a discussion of the concepts of available potential energy (APE) and a common approximation used when talking about APE.

2.3.1 Kinetic Energy

Assuming that the flow can be represented as two-dimensional with no rotation, the velocity field is given by $\boldsymbol{u} = (u(x,z,t), w(x,z,t))$ and the KE density (or just simply KE) of a fluid is defined at every location in space and time by

$$\varphi_k = \frac{1}{2}\rho_0(u(x,z,t)^2 + w(x,z,t)^2). \tag{2.59}$$

where u is the horizontal component of the velocity of the fluid, w is the vertical component of the velocity of the fluid and ρ_0 is a reference density. An important point to be made here is that for φ_k to be correct before making the Boussinesq approximation, ρ_0 should be replaced with the full density field ρ. In order to be consistent with the Boussinesq approximation, ρ_0 must appear in the above equation. Often in the literature, ρ_0 is dropped from the above equation, but this will not be done here. Note also that the analysis is restricted to only the $x-z$ plane for simplicity, but adding a third dimension is almost no extra work. To get the total KE density, φ_k can simply be integrated over all space which leaves the KE density as only a function of time, Φ_k:

$$\begin{aligned}\Phi_k(t) &= \frac{1}{HL}\int_0^H \int_0^L \varphi_k dxdz \\ &= \frac{1}{HL}\int_0^H \int_0^L \frac{1}{2}\rho_0 \left(u(x,z,t)^2 + w(x,z,t)^2\right) dxdz. \end{aligned} \tag{2.60}$$

The above quantity is the mean KE density as a function of time. Often, the horizontal structure of the KE density is of interest so instead, one can perform a vertical integral of the KE. The vertically integrated KE, or the vertical mean of KE, is simply the following:

$$\mathcal{KE}^{(p)}(x,t) = \frac{1}{H}\int_0^H \frac{1}{2}\rho_0 \left(u(x,z,t)^2 + w(x,z,t)^2\right) dz \tag{2.61}$$

This formulation of the KE gives tells how the vertical mean of KE changes with time and allows for a useful interpretation of the temporal changes in the KE in addition to spatial changes. Alternatively, more can be learned regarding the distribution of energy across wavelengths by investigating the Fourier Transform of the above quantity. Since the physical variable x and the Fourier variable k are Fourier pairs, by taking the Fourier Transform of a quantity in physical space, the spectral distribution of that quantity is produced. In the $x-z$ plane transforms with respect to x and z are necessary. This can give a new perspective on the motion that would otherwise be impossible to quantify otherwise.

For a finite domain the Fourier transform becomes a Fourier series when the appropriate periodic extension of the function is used (e.g. odd for a sine series). The periodic extension depends on the boundary conditions. For this section, the boundary conditions are chosen

to match those in chapter 3. Mathematically, these are

$$u(0,z) = u(L,z) = 0, \tag{2.62}$$
$$w(x,0) = w(x,H) = 0, \tag{2.63}$$
$$\rho_x(0,z) = \rho_x(L,z) = 0, \tag{2.64}$$
$$\rho_z(x,0) = \rho_z(x,H) = 0 \tag{2.65}$$

where the second two are for computational convenience and not strictly necessary. In the following section is presented only the transform of the u contribution to the kinetic energy (the vertical component's contribution follows the same algorithm albeit for an expansion in a slightly different basis). Because of these conditions at the boundary and assuming u is periodic on $[0, L]$, the horizontal velocity field can be formulated in terms of a Fourier sine series in x.

$$u(x,z,t) = \sum_{n=1}^{\infty} \hat{u}_n(z,t) \sin\left(\frac{n\pi x}{L}\right). \tag{2.66}$$

Suppressing the functional dependence of u and $\hat{u}_n$, u^2 becomes

$$u^2 = \sum_{n=1}^{\infty} \hat{u}_n \sin\left(\frac{n\pi x}{L}\right) \sum_{m=1}^{\infty} \hat{u}_m \sin\left(\frac{m\pi x}{L}\right). \tag{2.67}$$

Integrating the above equation over the domain $[0, L]$ gives

$$\int_0^L u^2 dx = \int_0^L \left[\sum_{n=1}^{\infty}\sum_{m=1}^{\infty} \hat{u}_n\hat{u}_m \sin\left(\frac{n\pi x}{L}\right) \sin\left(\frac{m\pi x}{L}\right)\right] dx. \tag{2.68}$$

Since $\hat{u}_n$ and $\hat{u}_m$ do not have a dependence on x, and the sum and the integral can be switched, the above equation above becomes

$$\int_0^L u^2 dx = \sum_{n=1}^{\infty}\sum_{m=1}^{\infty} \hat{u}_n\hat{u}_m \int_0^L \sin\left(\frac{n\pi x}{L}\right) \sin\left(\frac{m\pi x}{L}\right) dx, \tag{2.69}$$

and the integral in the above equation becomes

$$\int_0^L \sin\left(\frac{n\pi x}{L}\right) \sin\left(\frac{m\pi x}{L}\right) dx = \delta_{n,m}\frac{L}{2} \tag{2.70}$$

where $\delta_{n,m}$ is the Kronecker Delta. Thus, equation (2.69) becomes.

$$\int_0^L u^2 dx = \frac{L}{2} \sum_{n=1}^{\infty} \sum_{m=1}^{\infty} \hat{u}_n \hat{u}_m \delta_{n,m} \tag{2.71}$$

Using the properties of the Kronecker Delta, the above infinite sum becomes

$$\int_0^L u^2 dx = \frac{L}{2} \sum_{n=1}^{\infty} \hat{u}_n^2. \tag{2.72}$$

Upon performing the analogous operation for $\hat{w}_n$, the vertically integrated KE becomes

$$\mathcal{KE}^{(f)}(t) = \frac{1}{2}\frac{1}{H} \int_0^H \frac{L}{2} \sum_{n=1}^{\infty} \frac{1}{2} \rho_0 \left(\hat{u}_n^2 + \hat{w}_n^2 \right) dz \tag{2.73}$$

The vertical mean of KE in equations (2.73) (wavenumber space) and equation (2.61) (physical space) represent the same quantity but can be manipulated in different ways to understand different aspects of the flow field. This relationship is known as Parseval's Theorem [39, 18]. For instance by summing only over a subset of the Fourier components, $\hat{u}_n$, in equation (2.73), one can determine what proportion of KE is found in a certain subset of horizontal modes. Likewise, integrating over only part of the domain in equation (2.61), one can calculate how much energy is in a certain part of the domain.

As a summary, all of these forms of the KE are related via the following: φ_k is the KE density at any point in space or time in the domain, $\Phi_k(t)$ is the mean KE density at any point in time, $\mathcal{KE}^{(p)}$ is the vertical mean of the KE in physical space, and $\mathcal{KE}^{(f)}$ is the vertical mean of the KE in wavenumber space.

2.3.2 Potential Energy

In the field analogue to the numerical experiments presented in chapter 3, the stress on the surface due to the wind ultimately provides an initial input of potential energy, PE, by tilting the density interface. This process is very complicated [59], but the idea is that a certain amount of KE from the wind is transformed into some PE which can then be used for work on the on the fluid. The energy that is available to do work on the fluid is known as the available potential energy, or the APE. In order to develop an understanding of the APE input from the wind (or the tilt of a tank in an experimental setting), in two

dimensions, the mean PE of a fluid must first be defined as the following:

$$PE = \frac{1}{LH}\int_0^L \int_0^H \rho(x,z,t) g z dz dx \tag{2.74}$$

where $\rho(x,z,t)$ is the full density field. If the fluid was completely at rest with horizontal density surfaces, it would still have some potential energy due to the fact that the fluid's centre of mass has non–zero displacement from the reference height. However, this energy cannot be used to do work. This part of the PE is called the background potential energy, BPE, defined as

$$BPE = \frac{1}{HL}\int_0^L \int_0^H \tilde{\rho}(z,t) g z dz dx \tag{2.75}$$

where $\tilde{\rho}(z,t)$ is the adiabatically rearranged density field. Calculating the BPE can be a numerically costly process because calculating $\tilde{\rho}(z,t)$ involves rearranging the density field to its most stable configuration at each time. In an open system, if BPE is to be calculated, the adiabatically rearranged density field can be hard to define, so an alternative is to define the BPE in terms of the far field density[27]. However, in a closed system, the BPE is well defined by the rearranged field, equation (2.75).

With the continuously stratified model, the APE can be calculated by simply taking the difference between the PE and BPE: $APE = PE - BPE$, or

$$APE = \frac{1}{LH}\int_0^L \int_0^H (\rho(x,z,t) - \tilde{\rho}(z,t)) g z dz dx. \tag{2.76}$$

In a closed system with a continuous stratification, the APE varies in time due to different processes which are developed and discussed in detail in Winters et al. [57] and Winters and D'Asaro [56]. The main findings of the above mentioned papers are that in a continuously stratified fluid in a closed system, APE can go to one of two places; to KE or directly to BPE. The mechanism by which APE gets transferred to KE is known as the buoyancy flux and the mechanism that changes APE to BPE is the irreversible mixing of fluid layers. Fluid mixing is one process which leads to the decay of the amplitude of internal oscillations. Viscous dissipation also directly damps the internal oscillations by removing KE from the system. From viscous dissipation, the temperature of the fluid becomes higher due to the fact that the internal energy has increased. Some of the internal energy is then put in the background at a rate proportional to the overall density difference in the fluid [57].

Though the method of calculating the PE above is formally correct, if the two layer

approximation of the fluid is made, the following expression can be used to derive the two layer approximation for the APE, which is denoted by $APE^{(2)}$. Useful insights on how the different energy fluxes present within the wavefield can be gained from this, especially from a spatial perspective. To derive the two layer approximation for the PE, denoted by $PE^{(2)}$, the density field must first be decomposed into its two layer analogue:

$$\rho^{(2)} = \begin{cases} \rho_1 & z_0 + \eta \leq z \leq H \\ \rho_2 & 0 \leq z \leq z_0 + \eta \end{cases} \tag{2.77}$$

with the deflection of the interface about the mean depth z_0 is given by η. Substituting the above approximation into equation (2.74) gives

$$PE^{(2)} = \frac{1}{HL} \int_0^L \left(\int_0^{z_0} \rho_2 g z dz + \int_{z_0}^{z_0+\eta} \rho_2 g z dz + \int_{z_0+\eta}^{H} \rho_1 g z dz \right) dx. \tag{2.78}$$

Since APE is simply the difference between the PE of the system and BPE of the system, the next step is to calculate the PE of the fluid if it was stationary, in this case meaning the PE if $\eta = 0$. The two layer PE of a motionless is system, denoted by $BPE^{(2)}$, is given by

$$BPE^{(2)} = \frac{1}{HL} \int_0^L \left(\int_0^{z_0} \rho_2 g z dz + \int_{z_0}^{H} \rho_1 g z dz \right) dx. \tag{2.79}$$

Using the definition for APE, the two layer analogue to the APE in a closed system is given by

$$\begin{aligned} APE^{(2)} = \frac{1}{HL} \int_0^L \Bigg(& \int_0^{z_0} \rho_2 g z dz + \int_{z_0}^{z_0+\eta} \rho_2 g z dz \\ & + \int_{z_0+\eta}^{H} \rho_1 g z dz - \int_0^{z_0} \rho_2 g z dz - \int_{z_0}^{H} \rho_1 g z dz \Bigg) dx \end{aligned} \tag{2.80}$$

which simplifies to

$$APE^{(2)} = \frac{1}{HL} \int_0^L \left(\frac{1}{2}(\rho_2 - \rho_1) g (z_0 + \eta)^2 - \frac{1}{2}(\rho_2 - \rho_1) g z_0^2 \right) dx. \tag{2.81}$$

Expanding the $(z_0 + \eta)^2$ and simplifying gives the following equation:

$$APE^{(2)} = \frac{1}{HL} \int_0^L \left(\frac{1}{2}(\rho_2 - \rho_1) g \eta^2 + \frac{1}{2}(\rho_2 - \rho_1) g z_0 \eta \right) dx \tag{2.82}$$

The boundary conditions for the density field in a continuously stratified fluid (which will be discussed later) are $\nabla\rho \cdot \boldsymbol{n} = 0$, so the two layer analogue is that $\frac{\partial\eta}{\partial x}\Big|_{x=0,L} = 0$. This implies that η can be written in the following way:

$$\eta \sim \sum_{n=1}^{\infty} \eta_n \cos kx \tag{2.83}$$

with $k = \frac{n\pi}{L}$ and η_n are expansion coefficients.

Simply integrating the above representation of η over the entire domain gives 0 because of the parity of the expansion, thus the second term in equation (2.82) contributes nothing to the APE. After re–writing $\rho_{2,1} = \rho_0\left(1 \pm \frac{\Delta\rho}{2}\right)$, the two layer approximation of the two layer APE is

$$APE^{(2)} = \frac{1}{2}\frac{\Delta\rho g\rho_0}{HL}\int_0^L \eta^2(x)dx. \tag{2.84}$$

By making the two layer approximation for the fluid, insight on the motion can be gained by considering only the interface displacement rather than the entire density field. This has proven useful in published experimental work [22]. Using a similar algorithm discussed in the KE section, wavenumber information of APE is now available due to the fact that the boundary conditions imply that η^2 can be broken down into Fourier modes which can independently be discussed.

2.4 Mixing Characterizations

The final section of this chapter is a discussion of the various ways mixing is quantified in this thesis. First, a few brief words on diffusion can shed some light on why mixing might be worth studying. As an example, if a fluid is temperature stratified resulting in a stratification similar to equation (2.48), the two component layers will undergo heat diffusion until the entire fluid has reached some intermediate temperature barring any motion or outside forcing. In a fluid in a closed system with no external sources, this equilibrium temperature is the average of the layer temperatures, however, this process is remarkably slow.

The time at which diffusion will begin to play an appreciable role is calculated from

equation (2.19) using the following scalings:

$$\begin{aligned} \rho &= \Delta\rho\tilde{\rho} \\ \nabla &\sim \frac{1}{2h} \\ t &= T_{diff}\tilde{t} \end{aligned}$$

where T_{diff} is the diffusive timescale, $\Delta\rho$ is the density difference, h is the pycnocline half–width, and the gradient operator operates only in the vertical direction and is strongest at the pycnocline. Using these scalings and balancing the diffusive term with the unsteady term in equation (2.19), one arrives at a scaling for the diffusive time:

$$T_{diff} = \frac{4h^2}{\kappa}. \tag{2.85}$$

With ordinary values of κ being on the order of $10^{-7}\text{m}^2/\text{s}$ and pycnocline thickness in laboratory experiments on the order of 0.01 m, the diffusive timescale can be quite large, on the order of about 4×10^3 s. The large value of the diffusive time scale implies that there must be other processes at work to enhance the effects of diffusion in the field, where observations suggest that layers of fluid mix much faster than T_{diff}. This process by which enhanced diffusion occurs is generally termed *fluid mixing*.

The following discussion gives the background on two quantification methods of fluid mixing, one from an energetic perspective and one from a perspective based on the stretching of the interfaces between fluid layers. The first is termed the *Energetic mixing characterization* (EMC) which is based upon the idea of BPE presented in [57, 56], while the latter is not as widely used but has the added benefit of allowing for local information of fluid mixing to be preserved and is termed the *Variability mixing characterization* (VMC) based on the idea of defining the variability of the density field [43].

2.4.1 Energetic Mixing Characterization

The Energetic mixing characterization is understood as an irreversible increase in the BPE of the fluid (equation (2.75)). Most of the initial input of APE is converted to KE, but due to diapycnal mixing (spreading of isopycnals), some of this APE is changed to BPE where it is no longer accessible to the system. Alternatively, some of the KE can be dissipated due to fluid friction which increases the internal energy (equation (2.16)) and some of this internal energy is in turn changed to BPE at a rate proportional to the overall density difference of the fluid. This entire process is derived and schematized in Winters et al. [57].

Assuming the fluid is homogeneous in the y direction, the potential energy can be modeled as a 2D entity and the Energetic mixing characterization (EMC) is quantified by the following:

$$EMC = \frac{1}{BPE(0)} \int_0^L \int_0^H \tilde{\rho}(z,t) g z dz dx - 1 \tag{2.86}$$

where $\tilde{\rho}(z,t)$ is the adiabatically rearranged density field in equation (2.76) and $BPE(0)$ is the initial BPE of the fluid. The above quantity is the normalized increase in the background potential energy during the motion of the fluid and is a direct measure of the irreversible mixing in the fluid.

2.4.2 Variability–based mixing characterization

The characterization of mixing in this subsection is based upon the idea of a tracer's variability. The following method can be used for any arbitrary tracer that satisfies an advection–diffusion equation like equation (2.19). Specifically, if the density field is the tracer of interest, the mean variability of the density field is defined as

$$C = \frac{1}{2V} \iiint_V |\nabla \rho|^2 dV. \tag{2.87}$$

where in this case, V, is the entire volume of the tank. This quantity measures the "strength" of the density gradients in the fluid. This means that if there are many high density gradients (thin interfaces), then this quantity will be large. Conversely, if there are low or no density gradients, then this quantity will be low. Following [43], taking the time derivative of the variability gives

$$\frac{dC}{dt} = \frac{1}{V} \iiint_V \nabla \rho \cdot \nabla \frac{\partial \rho}{\partial t} dV \tag{2.88}$$

Using the product rule to rewrite the integrand in the above equation gives

$$\frac{dC}{dt} = \frac{1}{V} \iiint_V \underbrace{\nabla \cdot \left(\frac{\partial \rho}{\partial t} \nabla \rho \right)}_{(1)} - \underbrace{\frac{\partial \rho}{\partial t} \nabla \cdot \nabla \rho}_{(2)} \, dV. \tag{2.89}$$

The divergence theorem can be used on the first term to determine

$$\frac{dC}{dt} = \frac{1}{V}\left(\iint_{\partial V} \frac{\partial \rho}{\partial t}(\nabla\rho \cdot \boldsymbol{n})dA - \iiint_{V} \frac{\partial \rho}{\partial t}\nabla^2\rho dV\right). \tag{2.90}$$

Using the boundary conditions mentioned previously, $\nabla\rho \cdot \hat{\boldsymbol{n}} = 0$ on the boundary of the tank (∂V). Finally, ρ obeys equation (2.19), which is rewritten here for convenience:

$$\frac{\partial \rho}{\partial t} + \boldsymbol{u} \cdot \nabla\rho = \kappa\nabla^2\rho. \tag{2.91}$$

Upon substituting in the above integral expression, the rate of change of the variability is given by

$$\frac{dC}{dt} = \frac{1}{V}\iiint_{V} (\boldsymbol{u} \cdot \nabla\rho)\nabla^2\rho - \kappa(\nabla^2\rho)^2 dV \tag{2.92}$$

The first term in the integral of equation (2.92) is called *stirring*. This term works along isopycnals to stretch them out *or* squeeze them together, depending on the relative directions of the density gradient and the velocity field. A schematic of the stirring mechanism is shown in figure 2.6. The stirring mechanism is reversible meaning that one could imagine unstirring a fluid. This phenomenon can be easily seen in a very low Reynolds number flow or in fluids with remarkable low diffusivities.

The second term is referred to as *mixing*, and always decreases the variability of a tracer because it is a negative semi-definite quantity. Physically speaking, this term works orthogonal to isopycnals to spread them out, thereby always decreasing the variability of the tracer field. A schematic of the mixing mechanism is shown in figure 2.7. These mechanisms work in tandem to decrease the variability of the fluid. Stirring stretches isopycnals which then creates high density gradients where mixing can occur to irreversibly change the variability of the density field. For the analysis in this thesis, only the irreversible part of the change in variability is of interest so as to compare the EMC, which is irreversible by definition. The Variability Mixing Characterization (VMC) in 2 dimensions with the volume of the domain denoted by $V = HL$ and is non–dimensionalized by

$$\rho = \Delta\rho\tilde{\rho},$$
$$\nabla \sim \frac{1}{2h}.$$

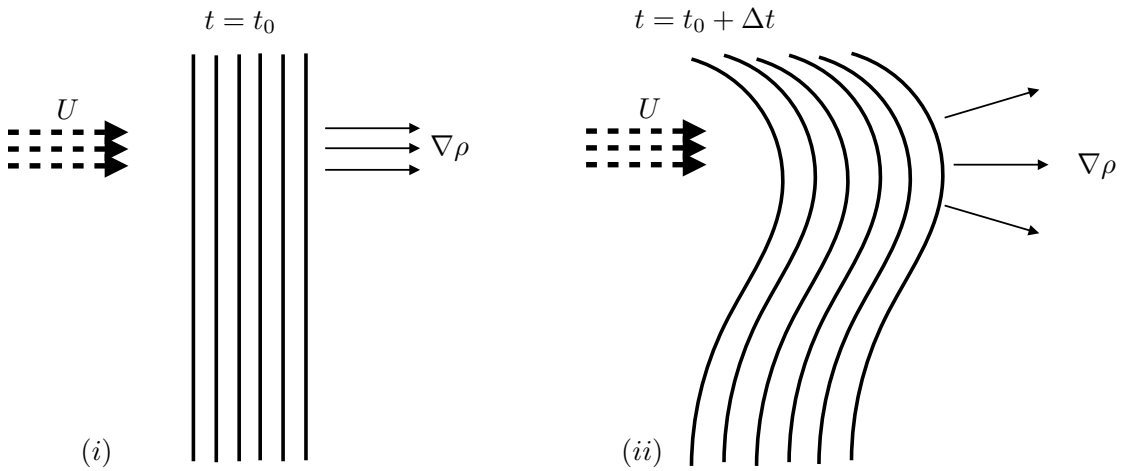

Figure 2.6: The effect of stirring on density contours. The example above shows a localized jet with velocity rightward denoted by hatched lines. The contour lines are lines of constant density (isopycnals). Panel (i) shows the states of the isopycnal surfaces at t_0 while panel (ii) shows the state of isopyncal surfaces a short time later at $t_0 + \Delta t$. When the gradient of ρ is oriented in the same direction as the velocity, the stirring is maximized meaning that the surfaces are advected around the most. Stirring stretches out isopycnal surfaces which effectively increases gradients.

Thus the VMC is defined as

$$VMC = \frac{(2h)^4}{HL\Delta\rho^2} \int_0^L \int_0^H |\nabla^2\rho|^2 dzdx. \tag{2.93}$$

This quantity measures the irreversible rate of change of the variability of the density field.

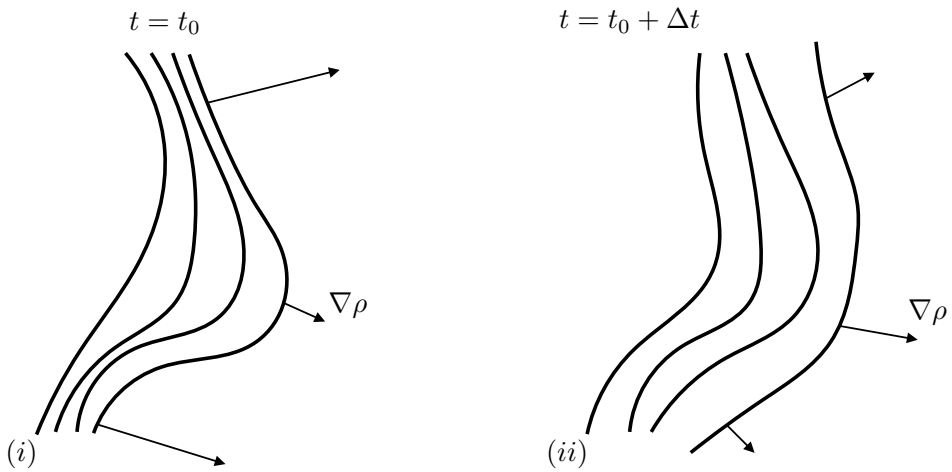

Figure 2.7: The effect of mixing on density contours. The contour lines are lines of constant density (isopycnals). Panel (i) shows the states of the isopycnal surfaces at t_0 while panel (ii) shows the state of isopyncal surfaces a short time later at $t_0 + \Delta t$. Mixing is maximized when isopycnals are close together (high density gradients). Mixing spreads out isopycnals, effectively reducing the density gradients.

Chapter 3

Results

The results section is organized as follows. First, the motivation for the results presented in this thesis is discussed including examples of past experiments and field observations. Following this, qualitative analysis and a discussion of the energetics of some small amplitude numerical experiments are provided to give some context for later results. Lastly, experiments on larger amplitude and smaller aspect ratio cases are discussed in order to compare features such as qualitative degeneration mechanisms, large scale energetics and mixing characteristics.

3.1 Motivation

Lakes that are relatively narrow are known to exhibit evidence of seiche motion, such as Loch Ness in Scotland [35]. This sort of motion provides the background state in a lake upon which smaller scale wave motion develops. Thus, understanding how this background state breaks down into different kinds of motion can provide an insight on how large scale energy cascades to the smaller scales. The breakdown of the background state is generically referred to as *degeneration*. Typically, models of seiches are done via linear–theories due to reasonably small amplitudes, but with sufficiently strong wind stress, the amplitude of the seiche can reach values where non–linear effects are important. Early in the history of geophysical fluid dynamics, linear theories were the only means available to analyze the motion, but with the ever increasing computing power available, complicated simulations can be performed and the degeneration can be analyzed.

To eliminate effects that may not be of interest, investigation into the degeneration of a seiche requires reasonably controlled conditions such as idealized boundaries, and a

consistent forcing parameterization. A series of laboratory experiments using the basic methodology in figure 1.1 were carried out by Horn et al. [22]. The goal of this study was to quantify different mechanisms responsible for the degeneration of large scale interfacial gravity waves in lakes under the influence of different amounts of wind stress, which was parameterized by the initial tilt of the interface with respect to the horizontal. The motivation to do this was to build an understanding of the processes that occur in lakes which bring the large scale initial APE to smaller scales where it can affect the boundary layer or be dissipated at various topological features. This aspect of the energy cascade is yet to be parameterized in field scale models which typically cannot account for sub-basin scale, non–hydrostatic motion.

The analysis of the experimental results in Horn et al. [22] were based on assuming simple two layer stratification, no mixing, homogeneous behaviour in the y direction and with layer–averaged velocities. By making these assumptions, the equations of motion became much more tractable and timescaling arguments could be made depending on some bulk parameters. The main results from Horn et al. [22] suggested that different degeneration mechanisms were expected to dominate depending on their relative timescales. The timescales that they focused on were those of shear instabilities, formation of solitary waves, supercritical flows, and damped linear waves. Each of the aforementioned timescales were derived as via existing theories in the literature. The timescale in which shear instability was expected to dominate was based on the stability criterion dictated by the gradient Richardson number, itself based on the finite–wavelength Taylor–Goldstein Equation (equation (2.40))[24]. The timescale in which super critical flow was expected to dominate was due to a layered Froude number criterion[58]. Solitary wave formation was based on a balance of the unsteady and steepening terms in equation (2.49), itself based on the two–layer idealization of long wave theory [19]. This assumption was made because closed form expressions for the propagation speed, non–linearity and dispersion coefficients are available when this approximation is used. Finally, the timescale in which linear waves were damped by viscosity was determined by a parameterization of the amplitude decay of an internal wave. In reality, the asymptotic expressions used for the various estimates do not have clear upper bounds on applicability in terms of seiche amplitude. Moreover, estimates based on different modes of degeneration, e.g. wave train formation versus shear instability, may not be theoretically consistent with one another. Nevertheless, in regimes where two different degeneration mechanisms are not expected to compete, this analysis does fine.

Using the timescaling analysis described above, Horn et al. [22] found that for certain initial tilts, the dominant degeneration mechanism is that of the development of dispersive solitary waves roughly predicted by equation (2.49). They compared the findings to field

data and found that most lakes underwent a steepening of the initial basin–scale wave and formed what they labeled 'solitons'. As a side note, internal solitary waves are, in fact, not solitons in the mathematical sense [25], and the trains of solitary-like waves that form in the experiments are not expected to exhibit soliton behaviour when colliding with end walls and other waves.

The fact that they found that the dominant mechanism was solitary wave formation agreed with published work. Observations of large amplitude wave trains in lakes have been reported at a wide variety of geographic locations. Lake Kinneret, Israel, has received consistent sampling over several decades and large amplitude trains of internal solitary-like waves (ISWs) have been reported in Lake Constance [41, 40, 42]. With respect to Lake Kinneret, Ostrovsky et al. [37] provided evidence that the smaller internal wave dynamics induced by a seiche in the lake can mix hypolimnetic and epilimnetic waters while Boegman et al. [6] provided a conceptual model of the fate of shoaling internal solitary waves and their ramifications for the bottom boundary layer of the lake. Specifically, Boegman et al. [6] proposed that due to surface wind forcing, horizontal currents were induced which degenerated into trains of solitary waves, which then shoal on the boundaries of the lake and energize the bottom boundary layer. This process has consequences for the biomass of the lake due to the vertical transport of organic material that might otherwise not have any way to reach the surface.

The data from this study was analyzed further in Boegman et al. [7]. In this study, the authors used the data from wave-gauges to determine how the initial non–linearity of the wave determined how energy was cascaded to small wavelengths through the emergence of a non–linear surge. The surge serves as one possible link between large scale oscillations, small scale features and wave propagation. The authors quantified the temporal distribution of available potential energy in different component horizontal wave modes and determined that the proportion of available potential energy brought to smaller scales by the non–linear surge scaled with the non–dimensional grouping $\alpha\eta_0/c_0$ where α is the non–linearity coefficient in the Korteweg–de–Vries (KdV) equation [23, 34, 19], c_0 is the wave speed and η_0 is the initial amplitude of the wave. Some of the data analysis techniques from Boegman et al. [7] are used in this thesis extensively.

Much of the theory discussed in Horn et al. [22] was independent of the length of the domain, thus some work is put into quantifying the degeneration of a laboratory scale standing wave under different initial wavelengths. Different numerical experiments show some dependence of degeneration on the wavelength of the initial condition. For a motivating example, if there is a lake of length l and depth d, the wind must input a certain amount of energy to tilt the pycnocline to an amplitude a. However, by making l larger, the energy required to tilt the thermocline to an amplitude a is larger. Since more mass is

moved, there is more energy available for oscillation. Thus, an attempt is made to quantify this phenomenon.

3.2 Governing equations and numerical method

Simulations are performed using the (psuedo)–Spectral Parallel Incompressible Navier–Stokes Solver(SPINS)[48]. The equations of motion that are solved are the incompressible Navier–Stokes Equations under the Boussinesq approximation which are restated here for convenience:

$$\frac{\partial \boldsymbol{u}}{\partial t} + \boldsymbol{u} \cdot \nabla \boldsymbol{u} = -\frac{\nabla p}{\rho_0} - \frac{\rho'}{g}\boldsymbol{k} + \nu \nabla^2 \boldsymbol{u}, \tag{3.1}$$

$$\frac{\partial \rho}{\partial t} + \boldsymbol{u} \cdot \nabla \rho = \kappa \nabla^2 \rho, \tag{3.2}$$

$$\nabla \cdot \boldsymbol{u} = 0. \tag{3.3}$$

The definitions of all of these symbols have not changed from the definitions in chapter 2. The numerical scheme employed uses 3rd order Adams–Bashforth time stepping with a dynamically varying time step and spatial derivatives are computed spectrally. The model has been thoroughly validated on a wide range of test cases [48] and has been used in many other studies [15, 12, 36, 13, 4, 47] and the present simulations have been validated against past results on Kelvin-Helmholtz billows in a parallel shear flow. A grid halving study was performed and it was determined that the present resolution is adequate for the results presented in this chapter.

All of the cases are run on a uniform grid in the horizontal and the vertical with no normal flow and free–slip boundary conditions for the velocities. The normal derivatives of the density field are specified at the boundary for computational purposes. By specifying the normal derivatives along the boundary, a cosine transform can be used to calculate the

derivatives of the density field. These are given mathematically as:

$$\begin{aligned} u(0,z) &= u(L,z) = 0 \\ w(x,0) &= w(x,H) = 0 \\ u_z(x,0) &= u_z(x,H) = 0 \\ w_x(0,z) &= w_x(L,z) = 0 \\ \rho_x(0,z) &= \rho_x(L,z) = 0 \\ \rho_z(x,0) &= \rho_z(x,H) = 0 \end{aligned}$$

Time is non–dimensionalized with the following *ad hoc* time scale for the horizontal mode-1 seiche:

$$\tau \sim \frac{4\pi}{3}\sqrt{\frac{L^2+H^2}{\Delta\rho g H}} \tag{3.4}$$

This timescale is the same timescale determined in the derivation of the dispersion relation for linear internal waves with horizontal mode number $n = 1$ given in equation (2.47) and then multipled by 2/3 so it approximately matched the period of the standing waves in this study. The reason for this is driven by the desire to present the scaling as a closed formula. The horizontal lengths are non–dimensionalized by L (the length of the domain) and vertical lengths by H (vertical extent of the domain).

The initial condition is taken to be a quiescent fluid with a density perturbation, given mathematically as

$$\rho(x,z) = \rho_0 + \frac{1}{2}(\rho_2 - \rho_1)\tanh\left(\frac{z-(z_0+\eta(x))}{h}\right) \tag{3.5}$$

where $\eta = \eta_0 \cos\left(\frac{\pi x}{L}\right)$ and $\boldsymbol{u}(x,z,0) = 0$. The relevant parameters used are h for the pycnocline halfwidth, the amplitude of the density surface, η_0 with respect to the average depth of the pycnocline, z_0. Here, ρ_0 is the reference density of the fluid and $\Delta\rho = \frac{\rho_2-\rho_1}{\rho_0}$. A schematic of the initial condition is given in figure 3.1 with a curve used to schematize the pycnocline. h was chosen to closely match Horn et al. [22] and to ensure that $\rho_z(x,0) = \rho_z(x,H) = 0$.

Parameters that change across trials are in tables 3.2 and 3.3 and parameters that do not change are in 3.1. The initial condition is chosen for mathematical simplicity and to facilitate a modal breakdown of energetics. As such it only approximately represents the state that the density interface would take in a tilted tank experiment.

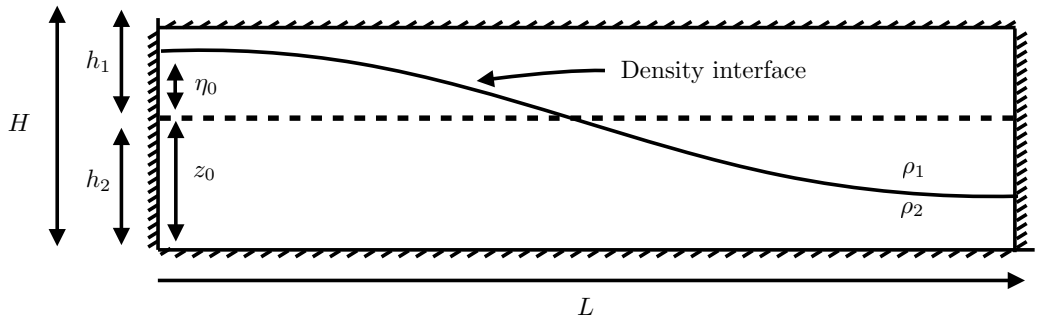

Figure 3.1: A schematic of the initial condition indicating each of the layer depths (h_1 and h_2), the total depth (H), the length (L), amplitude (η_0), and pycnocline mean depth (z_0). The continuous density interface is represented as a single curve. Here, h_1 and h_2 are the mean upper and lower depths of the fluid.

Table 3.1: Unchanged physical parameters for the cases in tables 3.2 and 3.3. ν is the kinematic viscosity, κ is the coefficient of heat diffusion, Sc is the Schmidt number (the ratio of kinematic viscosity to diffusivity), h is the half–width of the pycnocline, $\Delta\rho$ is the density difference between upper and lower layers normalized by the total density difference, ρ_0 is the reference density of the fluid and H is the total depth. The units are given in the table.

ν (m^2/s)	κ (m^2/s)	Sc	h (m)	$\Delta\rho$	ρ_0 (kg/m^3)	H (m)
1×10^{-6}	1.4×10^{-7}	6.99	0.005	0.02	1000	0.25

3.3 Small amplitude cases

This subsection aims to give some context to the degeneration of large amplitude seiches by looking at how small amplitude seiches change over time. Each of the following cases were simulated over 4 periods of oscillation beginning with the initial condition in equation (3.5). The following cases are classified by the dimensionless amplitude, η_0/h_1, also known as the inverse Wedderburn Number (W^{-1})[22, 21, 7, 14]. This number represents a parameterization of the wind stress that the surface of a body of water is subject to such that the density interface tilts with an amplitude of η_0 with respect to the vertical location of a horizontal pycnocline. The following four cases were run on a uniform 8192×512 grid, have a horizontal length of $L = 4$m, vertical length of $H = 0.25$m, a average pycnocline height of $z_0 = 0.15$m. The upper layer is $h_1 = H - z_0$. The results in the following sections are presented using perceptually uniform colormaps as to avoid instances of artificial gradients [49].

Table 3.2: All small amplitude cases considered in this subsection. N_x and N_z are the number of grid points in the x and z directions respectively, η_0 is the initial amplitude with respect to the mean depth z_0. L is the horizontal length, η_0/h_1 is the dimensionless amplitude with h_1 being mean upper layer depth, H/L is the aspect ratio and z_0/H is the dimensionless lower layer depth. The grid points are evenly spaced in both the vertical and the horizontal directions.

Case	$N_x \times N_z$	z_0 (m)	η_0 (m)	L (m)	η_0/h_1	H/L	z_0/H
SA–2	8192×512	0.15	0.02	4	0.2	0.0625	0.6
SA–25	8192×512	0.15	0.025	4	0.25	0.0625	0.6
SA–3	8192×512	0.15	0.03	4	0.3	0.0625	0.6
SA–35	8192×512	0.15	0.035	4	0.35	0.0625	0.6

The section is organized as follows. The qualitative evolution of two of the cases in table 3.2 will be discussed in detail and some of the important qualitative features will be discussed. Following the qualitative discussion is a quantitative discussion of the physical and fourier interpretations of the KE of the four cases presented in table 3.2. The discussion in this section serves as a tutorial for the results discussed in the the large amplitude section of this chapter.

The first case that will be discussed in detail is SA–2. This is the case with the smallest dimensionless amplitude considered, $\eta_0/h_1 = 0.2$ and is meant to demonstrate the effects of a seiche with a relatively small non–linearity. Snapshots of the density field are shown

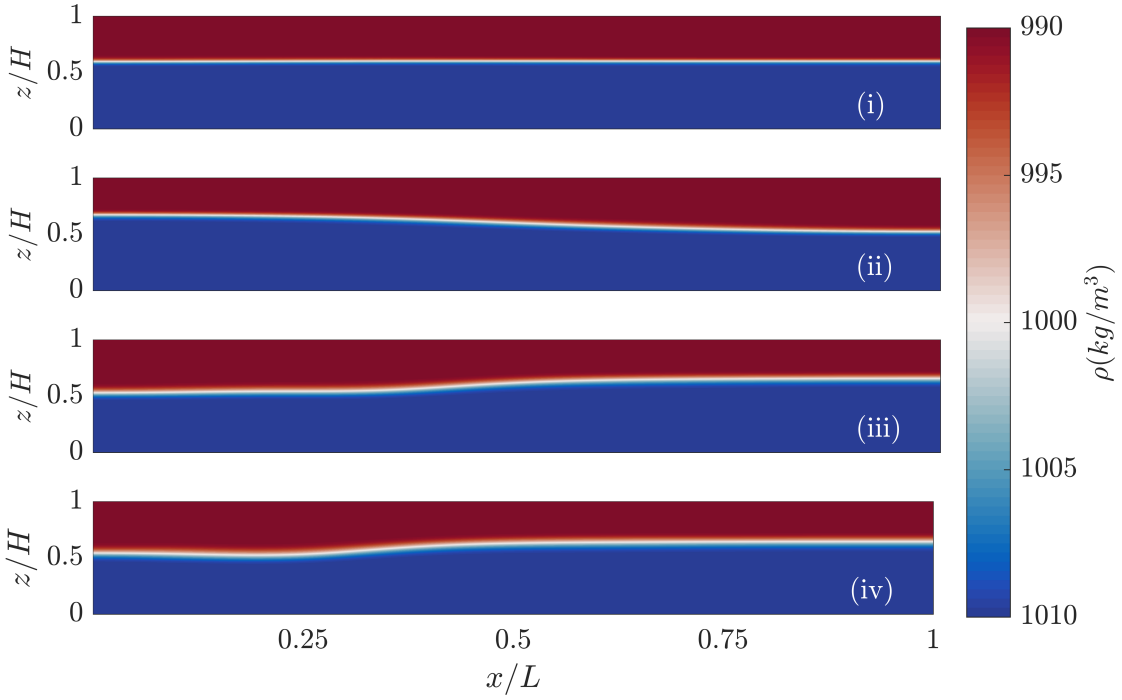

Figure 3.2: States of the density interface of case SA–2. Panel (i) is the density interface at $\tau = 0.25$, panel (ii) is at $\tau = 1$, panel (iii) is at $\tau = 2.5$ and panel (iv) is at $\tau = 3.5$.

in figure 3.2 with the upper layer denoted by red, the lower layer denoted by blue and the pycnocline denoted by the thin region between them. The initial condition is shown as a schematic in figure 3.1. At $\tau = 0.25$, figure 3.2(i), the interface is nearly flat meaning there is almost no APE and the energy is all kinetic. At $\tau = 1$, figure 3.2, the density interface continues to oscillate and has yet to show signs of non–linear behaviour. After the seiche has oscillated for another period and a half, $\tau = 2.5$ in figure 3.2(iii), there is some slight steepening just left of the centre of the tank. This is evident because the interface is no longer sinusoidal in nature but is more irregular. Lastly, at $\tau = 3.5$, figure 3.2(iv), there is some evidence of the formation of non–linear steepening on the left side of the tank at about $x/L = 0.25$.

Now, if the dimensionless amplitude is increased to $\eta_0/h_1 = 0.35$, there should be stronger non–linear effects that become apparent. In figure 3.3 are shown the states of the density interface for SA–35 at the same non–dimensional times as SA–2 so as to directly compare the motion. Again, at $\tau = 0.25$, figure 3.3(i), the interface is flat indicating

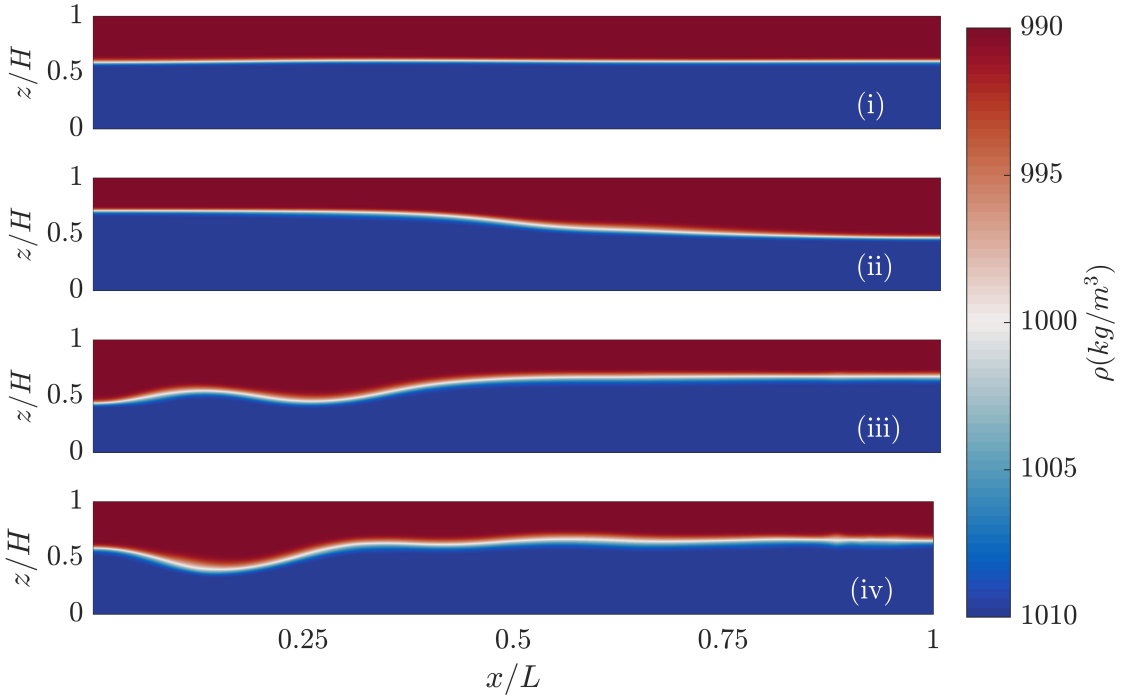

Figure 3.3: States of the density interface of case SA–35. Panel (i) is the density interface at $\tau = 0.25$, panel (ii) is at $\tau = 1$, panel (iii) is at $\tau = 2.5$ and panel (iv) is at $\tau = 3.5$.

that all the energy is in kinetic form. However, at $\tau = 1$, figure 3.3(ii), there is evidence of steepening at the node, which is about 1.5 oscillation periods earlier than SA–2. At $\tau = 2.5$ and $\tau = 3.5$, figures 3.3(iii–iv), a fully formed solitary wave propagates across the domain and reflects until is is eventually damped by viscosity.

An important process that occurs fairly frequently throughout this thesis is the steepening of the initial large scale wave into a train of solitary waves. The solitary wave takes a portion of the available energy from the seiche and brings it to smaller scales. For small amplitude seiches, there is not much available energy to redistribute to smaller scales, thus resulting in a small amplitude solitary wave occurring fairly late in the evolution of the wave. When the dimensionless amplitude of the initial state increases, the rate at which energy redistributes to smaller scales is higher. Qualitatively, this is understood because of the formation of the solitary wave in SA–35 at times when no such wave is visible in the SA–2 case.

3.3.1 Energetic comparison of the small amplitude cases

The evolution of the cases in table 3.2 can be quantified by looking at the vertical mean of KE. To help build a spatial understanding of the development of the KE in these cases, the vertical mean of KE, equation (2.61) is plotted below in figures 3.4(i), (iii), (v), and (vii) for cases SA–2, SA–25, SA–3, and SA–35 respectively. On the horizontal axis is the horizontal dimension of the tank and on the vertical axis is time measured in oscillation periods, equation (3.4). Meanwhile, in figures 3.4(ii), (iv), (vi), and (viii) is the normalized power spectral density, hereafter referred to as the PSD, for cases SA–2, SA–25, SA–3, and SA–35 respectively. The PSD is given by equation (2.73). On the horizontal axis is the normalized PSD and the vertical axis is time normalized by the the period of oscillations.

Considering figures 3.4(i), (iii), (v), and (vii); the vertical mean of KE initially appears as lobe–like structures in SA–2, SA–25, SA–3 and SA–35, but as the dimensionless amplitude is increased, the time in which the lobes deform decreases and the rate of deformation of the lobes indicates the rate that the effects of non–linearity occur. Under the influence of non–linear effects, the KE appears to change from lobes to streak–like features. These streaks that are the signature of a propagating solitary wave train. Of course, the rate at which non–linear effects redistribute energy is dependent on the dimensionless amplitude of the initial state and the difference between the layer depths, meaning that the cases with larger dimensionless amplitudes redistribute energy to become solitary waves faster than smaller amplitude cases.

Next, considering figures 3.4(ii), (iv), (vi), and (viii); for the smallest two cases, the KE is mostly in the largest modes, as the blue curve is mostly zero in this case and the red and green curve overlap for the entire simulation time. The second smallest case, the low mode and total KE overlap until the 3rd period of oscillation, where there is some high frequency motion that is captured by the blue curve. As the dimensionless amplitude increases more energy is found in the higher horizontal modes, as seen for the two higher mode cases where the red and green curves begin to separate from each other. As well, in the two of the largest cases considered in figure 3.4, there are high frequency oscillations in the vertical mean of KE due to wave interference there.

The first reason to show this picture is to demonstrate how the vertical mean of KE changes systematically due to an increase in the dimensionless amplitude of the seiche. It says that with a larger input of available potential energy, the seiche breaks into a solitary wave train faster and this process puts energy in smaller scales. This is not new information as will be shown later, but it serves to show how this process can be quantified. The second reason to show this picture is to demonstrate key features such as the streaks in the plot that represent the propagation of the solitary waves and the semi–circular lobes

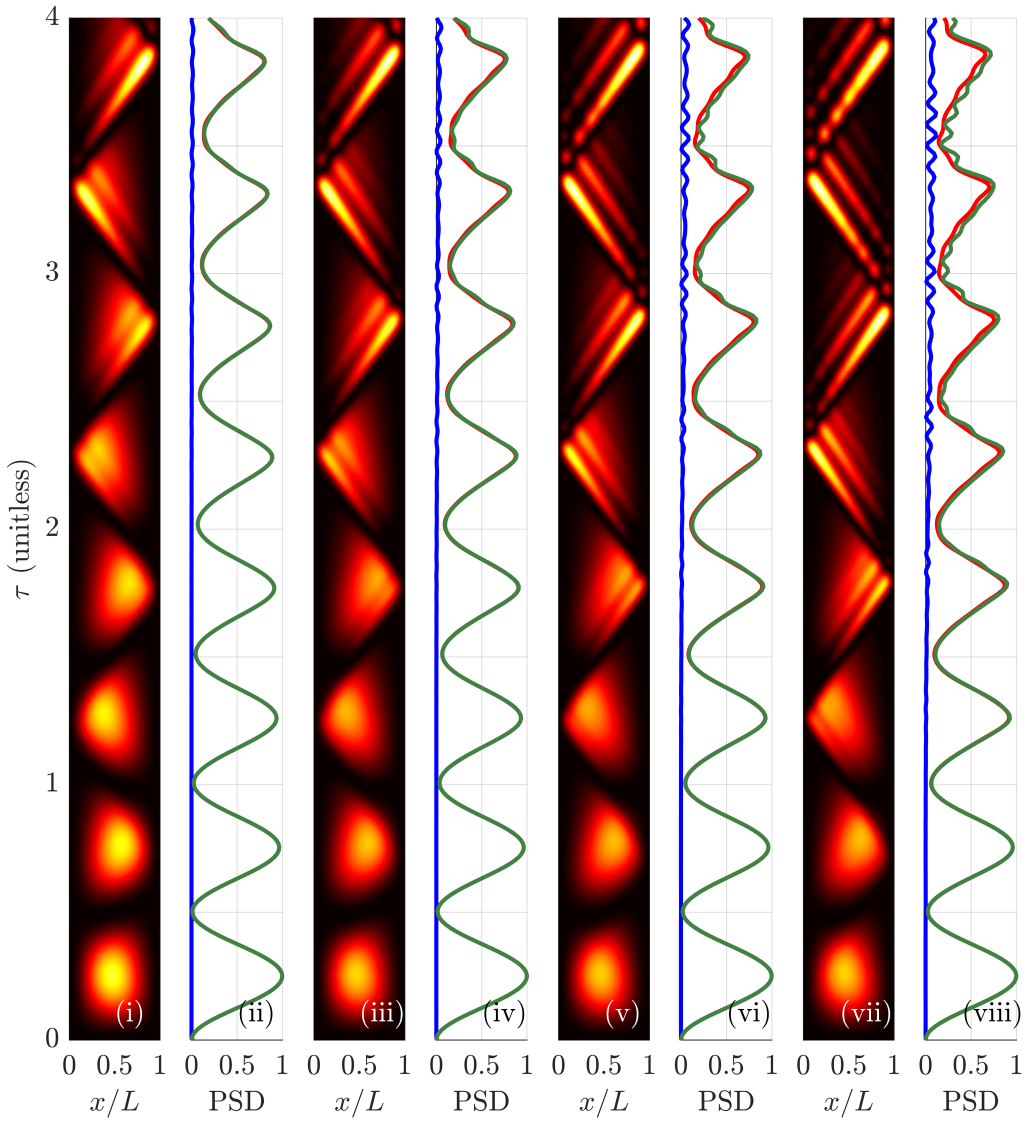

Figure 3.4: The vertical mean of KE(panels (i), (iii), (v), and (vii)) and the power spectral density, or the PSD(panels (ii), (iv), (vi), and (viii)), for the four cases summarized in table 3.2. Each pair of panels are the vertical mean and PSD for SA–2, SA–25, SA–3 and SA–35 respectively. The green curve represents the total KE, the red line is the sum of the KE over the first four horizontal modes, and the blue line is the sum of the remaining horizontal modes.

that represent the oscillation of the seiche itself.

Finally, in order to quantify smaller scale behaviour of the seiche undergoing evolution that is non–linear in nature, it is useful to get an idea of how the KE evolves by mode. In figure 3.5, the KE in each of the second to 8th horizontal modes time averaged over half a period is presented in the form of a histogram. Horizontal mode–1 is ignored because it encompasses so much of the kinetic energy and skews the plots. Each half period is represented a grouping of bars while each mode is represented by a bar of a certain colour. This is meant to show how each horizontal mode gains KE throughout the evolution of small amplitude seiche. Hypothetically speaking, each mode could be discussed individually, but that would complicate the plot without adding any extra useful information. Each grouping of bars is normalized by the maximum of the KE *in that half period*. This is due to the fact that some kinetic energy is dissipated due to friction and there might be losses of potential energy due to mixing. Non–linear effects can be characterized by energy moving from large scales to small scales due to the quadratic non–linearity in the momentum equations. In figure 3.5, this appears as an increase in KE in higher horizontal modes over time. For the smallest case, mode–2 initially starts with a small amount of energy, and higher horizontal modes start with almost none. As time progresses, all modes appear to gradually gain energy, which comes from the horizontal mode–1 seiche (not pictured in this plot). Qualitatively speaking, this behaviour can be seen in figure 3.4 by the change from symmetric to streaks due to the formation of solitary waves. As the dimensionless amplitude is increased, the increase in energy to the second mode happens at a higher rate. This rapid increase happens for about two oscillation periods after which, the increase appears to level off at about 15% of the KE. To summarize, for cases with sufficiently large dimensionless amplitude, KE from the horizontal mode–1 seiche is redistributed into the higher horizontal modes. Most of this energy goes into the next highest modes (horizontal mode–2) but with a large enough initial energy input, some energy is put in even smaller scales. Eventually this increase levels off. Similar processes have been discussed in previously published literature suggesting that there is intermodal energy flux until about the second period of oscilltion after which each mode is damped individually by viscosity [6]. According to the results in figure 3.5, after about 2 periods, there is still some increase in the higher modes for SA–3 and SA–35 after the beginning of the second period as well as an increase in horizontal mode–2 for the SA–2 and SA–25 cases.

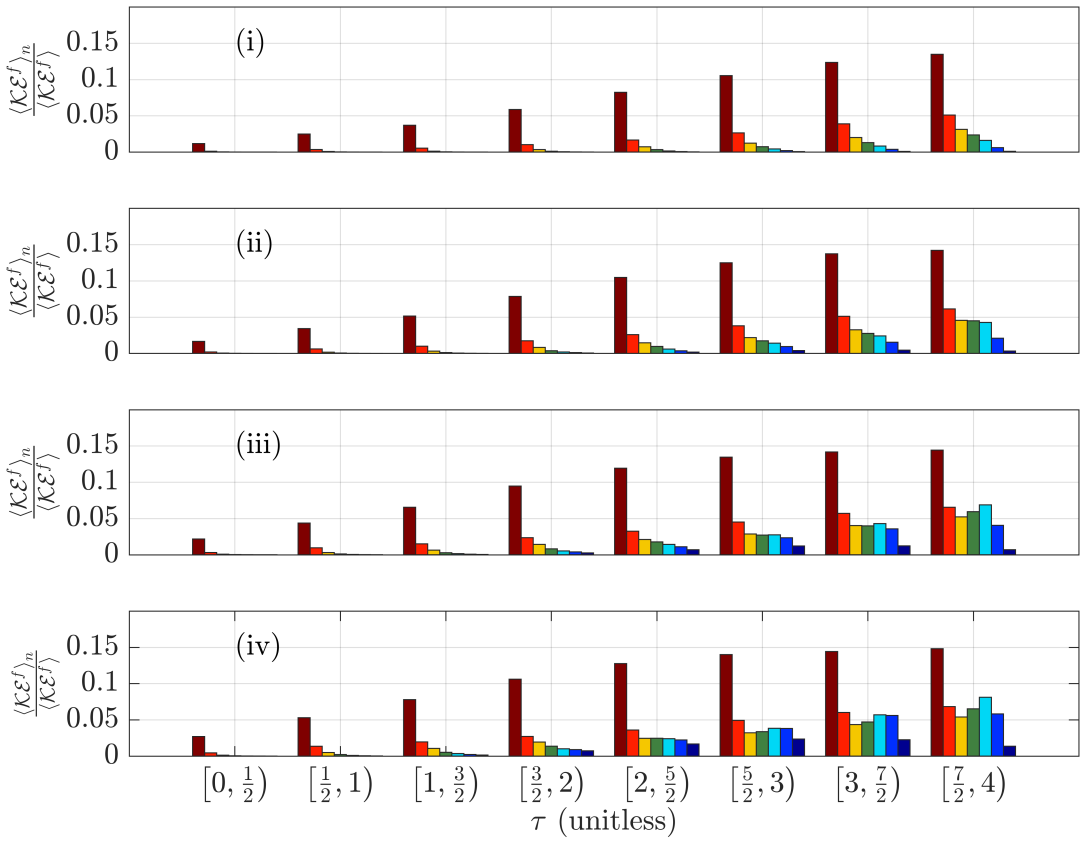

Figure 3.5: KE in each of the first 2 to 8 horizontal modes time averaged over half a period for four periods. Panel (i) shows case SA–2, panel (ii) shows SA–25 case, panel (iii) shows the SA–3 case, and panel (iv) shows SA–35 case. Each grouping of bars is normalized over the maximum KE in that time period. Horizontal mode–1 is ignored here because it skews the plots.

3.4 Large amplitude cases

The analysis regarding the large amplitude section is divided into 3 subsections. First, unlike the small amplitude section above, the evolution of two *symmetric* cases where $h_1 = h_2 = 0.5H$ is discussed. These cases are chosen to highlight the differences in the degeneration of the wave when weakly non–linear theories do not predict non–linear steepening. In equation (2.49), $\alpha = 0$ for cases where the layer depths are equal, this removing the ability for the wave to steepen. The first cases discussed are L5–2m and L5–8m. Following this, the quantitative breakdown of the energy into horizontal modes for these cases is discussed. The second subsection presents a discussion of the skew cases (15L5–8m and 25L5–8m) where $h_1 \neq h_2$ which is similarly followed by a detailed mode breakdown of the energy. The large amplitude section is followed by a section which contains a discussion of the KE and the APE of several of the large amplitude cases compared to one another. Finally, concluding this chapter is a discussion of irreversible mixing of the large amplitude cases.

A note that the cases are named using a different naming convention in this section. This is due to the face that cases are now classified due to both their dimensionless amplitude *and* their aspect ratio. Cases are also simulated to only two periods of oscillation instead of four. This is because three dimensional dynamics are expected earlier in the evolution and simulating only two dimensional motion for long times does not fully encapsulate the dynamics.

3.4.1 Symmetric Cases

First consider the L5–2m and L5–8m cases, both with equal layer depths. The cases are discussed independently followed by a comparison to the small amplitude cases. The states of the density interface are plotted at times $\tau = 0.25, 0.7, 0.9$, and 1.25.

Consider figure 3.6 which shows the temporal evolution of the L5–2m case. At early times in 3.6(i), the density interface is stable and there are two small amplitude waves steepening on either side of the node propagating inwards from the sidewalls. This is immediately different than any of the small amplitude cases. At about $\tau = 0.7$ and $\tau = 0.9$ (figure 3.6(ii)–(iii)), there is visible growth and collapse of shear instabilities on the interface near the node as the seiche reaches its second amplitude maximum at $\tau = 1$. As well, there is evidence of two statically unstable wisps that occur on the flanks of the pycnocline at about 0.25 and 0.75 of figure 3.6(iii). At about $\tau = 1.25$ (figure 3.6(iv)) shear instabilities

Table 3.3: All cases considered in the large amplitude section. Cases are characterized by depth above mid–depth in mm (e.g., a prefix of 15 means that the average depth of the pycnocline is 15 mm above $H/2$), amplitude with Q < P < L (smallest to largest), and finally tank length (1m is a tank length of 1 metre, etc.). All other columns have the same meanings as in table 3.2.

Case	$N_x \times N_z$	z_0 (m)	η_0 (m)	L (m)	η_0/h_1	H/L
Q5–1m	2048×512	0.125	0.05	1	0.4	0.25
P5–1m	2048×512	0.125	0.065	1	0.52	0.25
L5–1m	2048×512	0.125	0.0825	1	0.66	0.25
15L5–1m	2048×512	0.14	0.0825	1	0.75	0.25
25L5–1m	2048×512	0.15	0.0825	1	0.825	0.25
Q5–2m	4096×512	0.125	0.05	2	0.4	0.125
P5–2m	4096×512	0.125	0.065	2	0.52	0.125
L5–2m	4096×512	0.125	0.0825	2	0.66	0.125
15L5–2m	4096×512	0.14	0.0825	2	0.75	0.125
25L5–2m	4096×512	0.15	0.0825	2	0.825	0.125
Q5–4m	8192×512	0.125	0.05	4	0.4	0.0625
P5–4m	8192×512	0.125	0.065	4	0.52	0.0625
L5–4m	8192×512	0.125	0.0825	4	0.66	0.0625
15L5–4m	8192×512	0.14	0.0825	4	0.75	0.0625
25L5–4m	8192×512	0.15	0.0825	4	0.825	0.0625
Q5–8m	16384×512	0.125	0.05	8	0.4	0.03125
P5–8m	16384×512	0.125	0.065	8	0.52	0.03125
L5–8m	16384×512	0.125	0.0825	8	0.66	0.03125
15L5–8m	16384×512	0.14	0.0825	8	0.75	0.03125
25L5–8m	16384×512	0.15	0.0825	8	0.825	0.03125

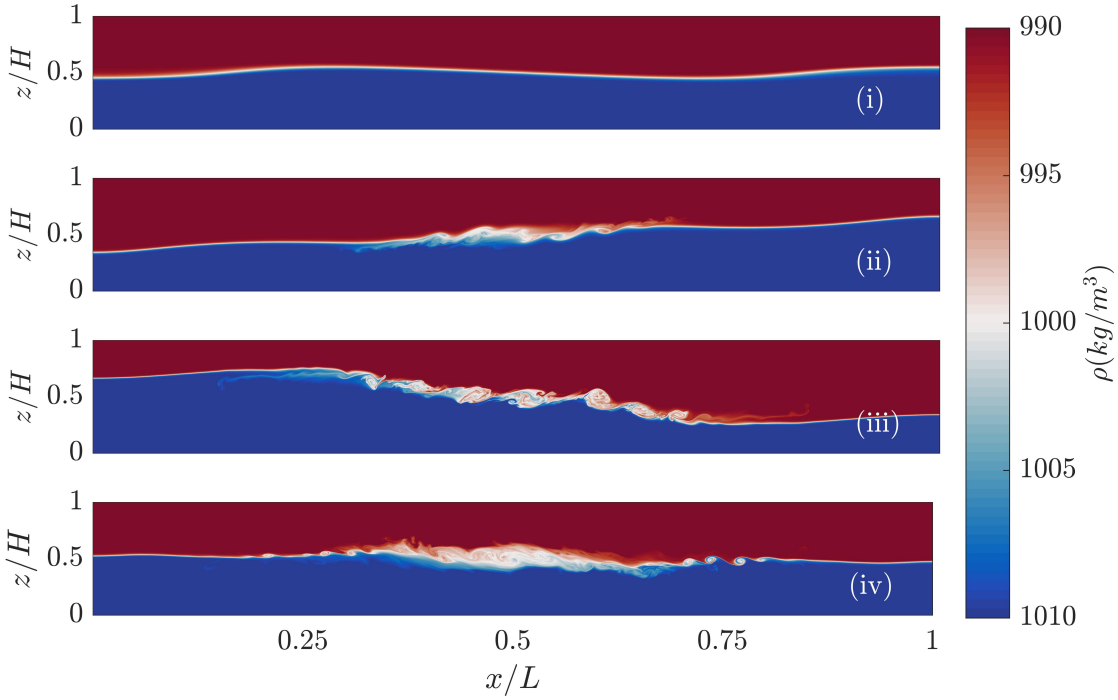

Figure 3.6: States of the density interface of case L5–2m. Panel (i) is the density interface at $\tau = 0.25$, panel (ii) is at $\tau = 0.7$, panel (iii) is at $\tau = 0.9$, and panel (iv) is at$\tau = 1.25$.

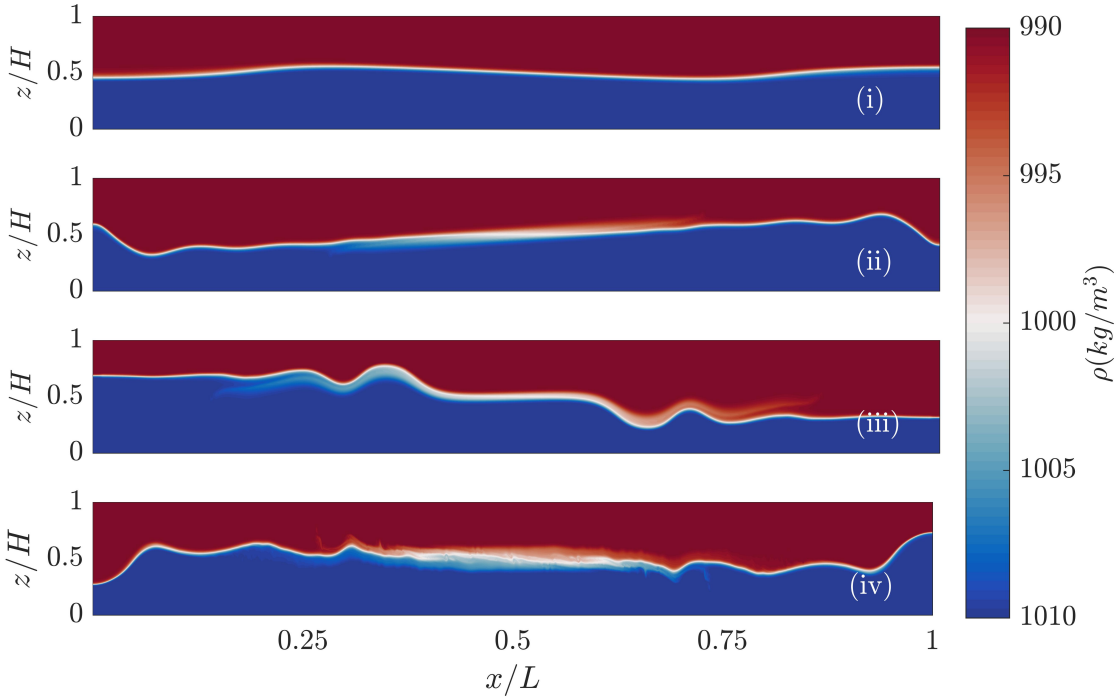

Figure 3.7: States of the density interface of case L5–8m. Panel (i) is the density interface at $\tau = 0.25$, panel (ii) is at $\tau = 0.7$, panel (iii) is at $\tau = 0.9$, and panel (iv) is at$\tau = 1.25$.

have completely collapsed. Due to the collapse, it looks as if enhanced interfacial mixing has occurred in the central region and the pycnocline has widened considerably near the centre of the domain providing a smoother density gradient there but is still fairly thin on the edges of the domain. There is also evidence of a second burst of shear instability as the wave continues to oscillate.

Consider now figure 3.7 which shows the L5–8m case. At early times, the state of the density interface is nearly indistinguishable to that of the L5-2m case (note the change in aspect ratio). The main similarity is the emergence of similar counter–propagating waves of small amplitude forming on the density interface. However, by $\tau = 0.7$ (figure 3.7(ii)), the state of the density interface differs dramatically. There is evidence of substantial deflections of the density interface at the walls as well as some widening near the node. At $\tau = 0.9$ (figure 3.7(iii)), there is clear formation of dispersive waves. At $\tau = 1.25$ (figure 3.7(iv)), there is clear evidence of higher horizontal mode wave activity near the sidewalls of the tank as well as some widening near the node. At this time, the horizontal mode–1 seiche should be at a KE maximum but because of the clear deflections of the interface, especially near the walls, this is not the case. This case appears to differ from the L5–2m case with respect to the primary degenerative mechanism that occurs.

These cases show some dramatic differences from the cases discussed in the small amplitude section. The first difference appearing in both L5–2m and L5–8m is the development of two counter–propagating waves as the wave begins to oscillate which are symmetric about the node of the seiche. Due to the symmetry of the layer depths, these counter propagating modes have identical behaviour save for their polarity. Due to the differences in the layer depths in the small amplitude cases, these nearly identical counter–propagating modes are not seen. The second clear difference is the way in which the interface changes in figures 3.6(ii) and 3.7(ii). It is clear that the mode of degeneration is fundamentally different when the length of the tank is increased and the amplitude is large. It appears that in the shorter cases, (including L5-1m which was not not shown) shear instabilities dominate the dynamics initially, while in the longer cases, (including L5-4m not shown) the seiche develops into higher horizontal mode waves and coexists with smaller scale shear instabilities. It seems that for the small amplitude cases, the amplitude is not large enough to trigger shear instability and the dominant degeneration is then the formation of a solitary wave. The symmetric cases also show no signs of true solitary wave motion. Broadly speaking, this behaviour agrees with the findings of equation (2.49). If the layer depths are equal, then no steepening can occur according to equation (2.49), resulting in no solitary wave formation. However, in the L5–8m case, higher horizontal mode waves do form from a larger scale wave meaning that there is still some process that redistributes the energy into higher modes that is not predicted by equation (2.49).

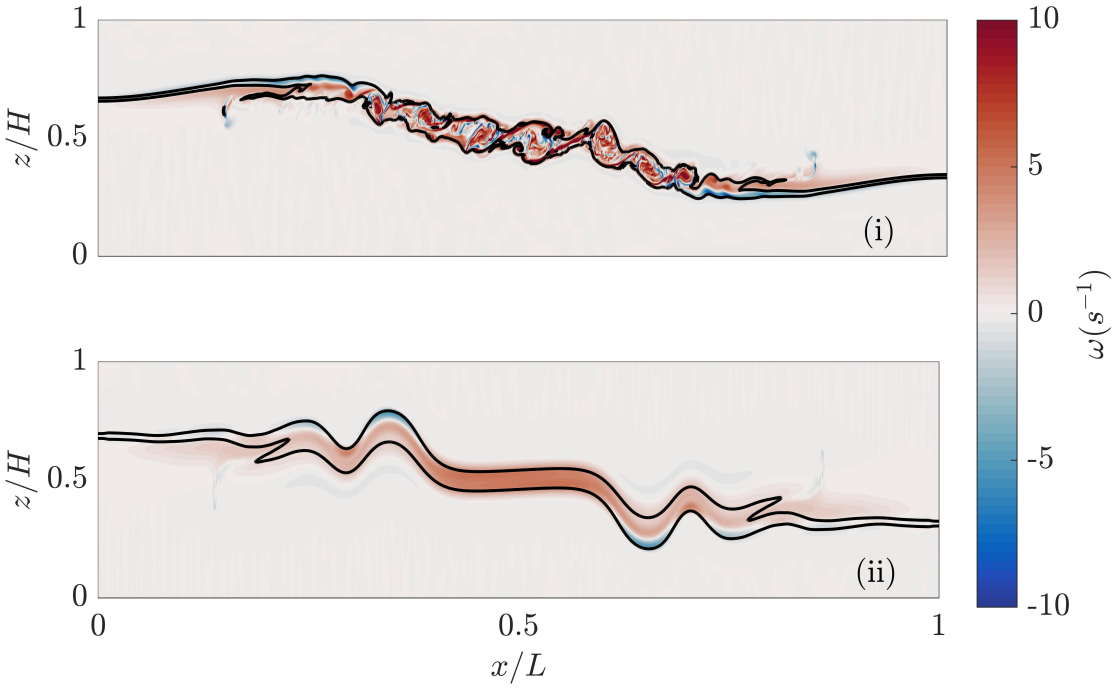

Figure 3.8: The vorticity field for the L5–2m (top) and L5–8m (bottom) cases at $\tau = 0.9$. The black contours are two representative isopycnals.

The redistribution of energy can be further visualized by looking at the vorticity fields and the KE fields for these cases. These fields are show in figures 3.8 and 3.9 respectively at $\tau = 0.9$.

As a reminder, the vorticity measures the local rotation of fluid particles. Where there is high vorticity, these is a large amount of rotation within the fluid. First consider figure 3.8(i), the vorticity in the L5–2m case is mainly large scale and induced by the oscillation of the seiche and is confined mostly to the pycnocline, which is denoted by the black isopycnals. There are some high frequency spatial variations within the pycnocline and even small features that are negative (or opposite in orientation to the seiche induced vorticity). Looking now at the vorticity shown in 3.8(ii) which shows the vorticity field for the L5–8m case. Similar to the L5–2m case, it is mostly positive due to the oscillation of the seiche with small amounts of negative vorticity at the peaks of the propagating modes and is mainly confined to the pycnocline. However, the vorticity field is qualitatively different from the L5–2m case because there are almost no fine scale features present and the field

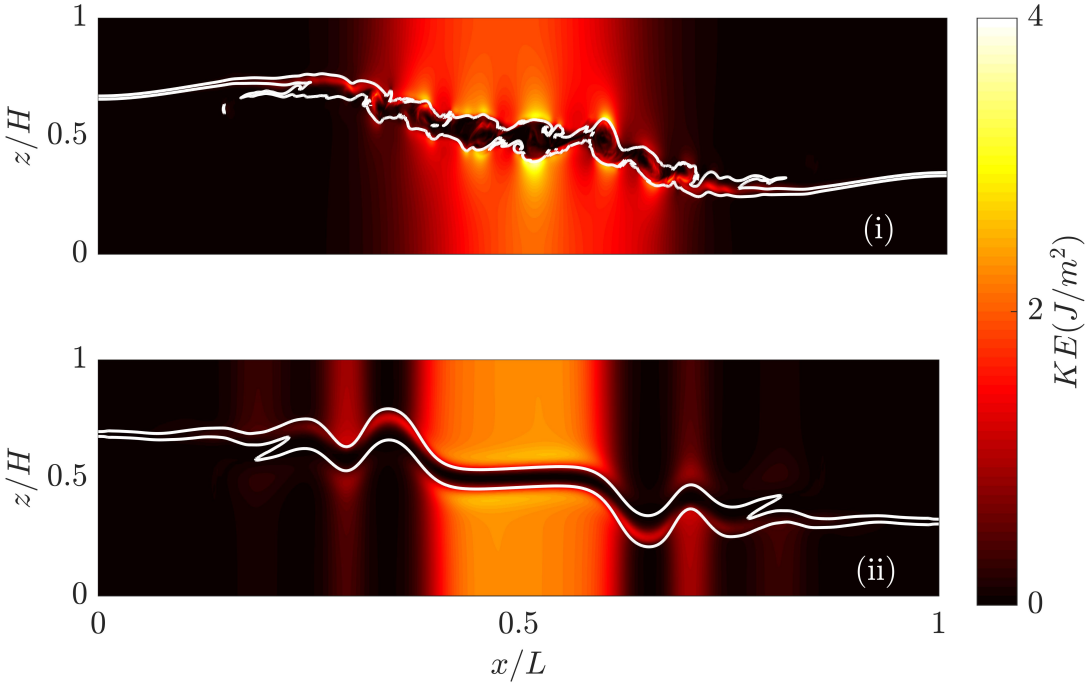

Figure 3.9: The KE for the L5–2m (top) and L5–8m (bottom) cases at $\tau = 0.9$. The white contours are two representative isopycnals.

has significantly less spatial variation.

Moving on to figure 3.9(i), the large scale KE in the L5–2m case is focused near the centre of the tank and is much more intense above and below the pycnocline rather than within it(characteristic of vertical mode-1 structure). However, there are some high frequency variations in the KE field within the pycnocline due to the instabilities that form there. A major difference in the KE of the L5–8m case is that at the horizontal location of the crests of the propagating waves there are vertical bands of KE due to their propagation. This feature differs from the L5–2m case because the highest KE was in a contiguous region near the node of the wave and it appears as if waves are not able to form in that case.

The main similarities between these two cases are that there is only a small amount of KE within the pycnocline when compared to the rest of the field, while the vorticity is contained to the pycnocline and is negligible outside it. There are small bands of negative vorticity at approximately the same non–dimensional location in both waves. As well, due to the L5–8m case being able to form high horizontal mode waves, KE is redistributed around the domain away from the centre region while this is not the case in the L5–2m case.

A better temporal understanding of how the energy is distributed in the domain is presented in figure 3.10. Figures 3.10(i) and (iii) show the vertical mean of KE for the L5-2m and L5–8m cases, respectively, as a function of time and space and figures 3.10(ii) and (iv) show a basic breakdown of the power spectral density [39] for the L5–2m case and L5–8m cases respectively. These plots are similar to figure 3.4 and have the same normalizations for time and space.

Consider the vertically integrated KE of the L5–2m case in figure 3.10(i). The first point to note is the periodic structure of the lobes in time due to the oscillation of the large scale seiche. Note that the shape of the first lobe here is slightly different than the shape of the lobes in figure 3.4 suggesting that the size of the dimensionless amplitude has an immediate effect on how energy is distributed around the domain. At $\tau = 0.5$, 1, 1.5, the KE is nearly zero, save for some faint streaks in the plot which are Kelvin–Helmholtz billows. These times, of course, correspond to a maximum or minimum of the seiche, meaning that the energy of the seiche is stored as potential. Another feature to note is that throughout the evolution of the L5–2m case, the KE is mostly distributed in a contiguous lobe which qualitatively agrees with figure 3.9(i). Looking now at the measure of the power spectral density of the L5–2m case in figure 3.10(ii), what is important to note here is that the total KE and the KE in the first four horizontal modes is nearly the same. This suggests that most of the KE is present in low horizontal modes while the KE

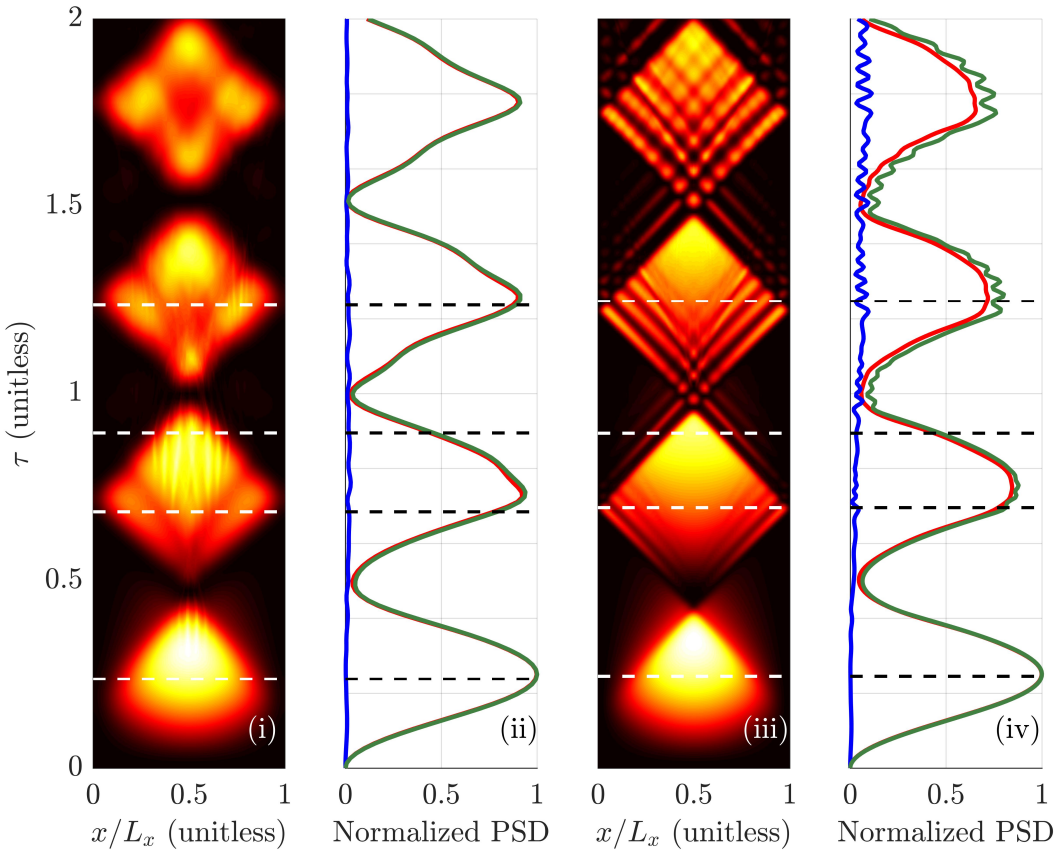

Figure 3.10: As in figure 3.4 but for the L5–2m (panels (i) and (ii)) and L5–8m (panels (ii) and (iv)) cases.

in the highest horizontal modes is very small. The curve tracing out the total KE is not a simple sinusoid suggesting that the background oscillation is not just a simple standing wave anymore.

Moving now to vertical mean of KE for the L5–8m case in figure 3.10(iii). Similar to the L5–2m case, the large scale behaviour is clearly periodic denoted by the lobe-like features in the plot, but the major difference is that the lobes of KE clearly break into a dispersive wave pattern in space–time suggesting higher mode wave activity. This suggests that there is some mechanism influencing the spatial structure of the KE of the seiche. This is apparent in figure 3.7 because of the high horizontal mode waves that appear on the density interface. This difference is also manifested in the power spectra shown in figure 3.10(iv). The smaller scales play a more prominent role in the degeneration of the interface because the contribution from the highest horizontal modes is a greater proportion of the total KE in this case than in the L5–2m case. The total and the low mode energies are noticeably different near the KE peaks at $\tau = 0.75$,1.25, and 1.75 possibly due to the fact that higher horizontal mode waves have a different period of oscillation and thereby undergo many oscillations over the course of one seiche period. This translates to a faster conversion between KE and APE for these modes which results in the high frequency horizontal oscillations seen in the vertically integrated KE.

Looking qualitatively at the states of the density interface for both symmetric cases considered, it seems that large scale process happen at about the same non–dimensional rate, but the small scale processes differ substantially depending on the length of the seiche. For the longer L5–8m case, the small scales appear to have more of an impact on determining how the interface changes in terms of horizontal wave modes, while for the shorter L5–2m case, the length of the tank seems to allow for the formation of shear instabilities which degenerate the interface differently.

3.4.2 Skew Cases

The following section outlines the qualitative evolution of cases where the layer depths are no longer equal. Physically speaking, z_0 has been changed for these cases. Snapshots of the 15L5–8m case are shown in figure 3.11 and the 25L5–8m case in 3.12.

Though equation (2.49) cannot accurately predict the motion of the seiche, the parameters governing the different mechanisms can still provide insight as to how fast some processes might occur. Since there is now a greater dimensionless amplitude than in the small amplitude cases discussed, non–linear effects are expected to happen earlier in the

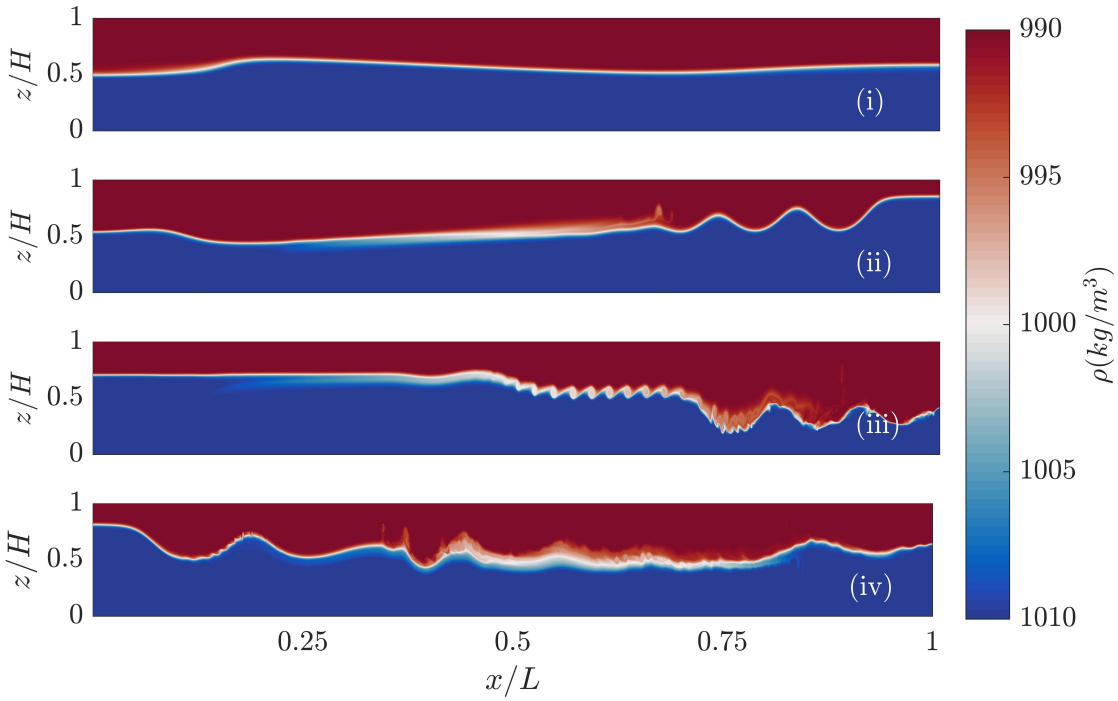

Figure 3.11: States of the density interface of case 15L5–8m. Panel (i) is the density interface at $\tau = 0.25$, panel (ii) is at $\tau = 0.7$, panel (iii) is at $\tau = 0.9$, and panel (iv) is at$\tau = 1.25$.

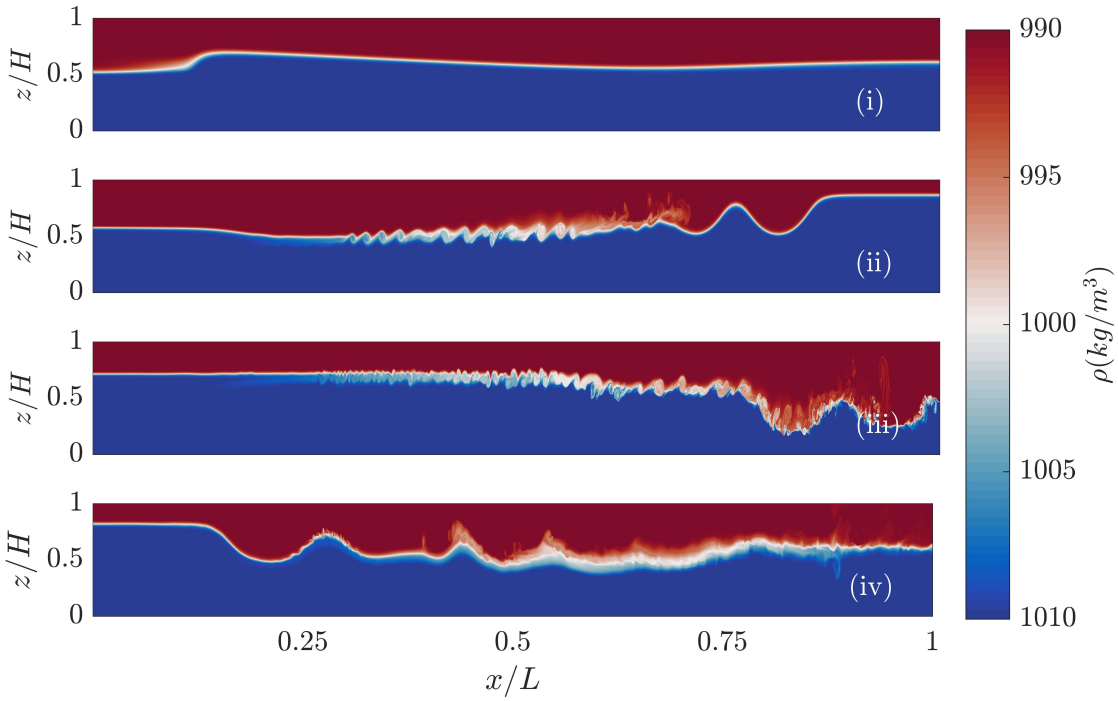

Figure 3.12: States of the density interface of case 25L5–8m. Panel (i) is the density interface at $\tau = 0.25$, panel (ii) is at $\tau = 0.7$, panel (iii) is at $\tau = 0.9$, and panel (iv) is at$\tau = 1.25$.

evolution of the wave. In the 15L5–8m case, the asymmetry in the layer depths reveals itself almost immediately in the form of a progressive surge. At $\tau = 0.25$ (figure 3.11(i)), a non–linear steepening process on the left side of the tank is beginning. This differs from the symmetric cases where two initial wave fronts steepen at approximately the same rate. At $\tau = 0.7$ (figure 3.11(ii)), a dispersive solitary wave train is seen to propagate rightwards. At $\tau = 0.9$ (figure 3.11(iii)), the wavetrain has reflected off the right hand wall and propagates leftwards. The dispersive wave train is mostly preserved upon reflection and there are some shear instabilities on the density interface to the right of the node. Finally, at $\tau = 1.25$ (figure 3.11(iv)), the solitary wave train has reached the left side of the tank and the pycnocline has widened where the shear instabilities collapse. What is also of note is the formation of very small shear instabilities on the right hand side of the leading solitary wave within the depression.

Upon increasing the difference between the layer depths, the behaviour changes slightly. Plots of the density field for 25L5–8m are shown in figure 3.12(i)–(iv). At $\tau = 0.25$ (figure 3.12(i)), a similar but faster steepening process occurs for the rightward propagating wave. The leftward propagating wave is barely noticeable in this case. At $\tau = 0.7$ (figure 3.12(ii)), a dispersive wave train has formed, similar to that of figure 3.11(ii). A difference to note here is that dispersion has a weaker influence on the leading wave due to the fact that there are only two waves which make up the wave train whereas in the figure 3.11(ii), there are 3 clear waves. Close to the centre of the tank, many high density gradients are forming due to the development of shear instabilities which is unlike the static instability formed in figure 3.11(ii). Finally, there is a rightward propagating reflected mode that is slowly steepening. At $\tau = 0.9$ (figure 3.12(iii)), the wave train has reflects off the righthand wall and propagates leftward which subsequently collides with the shear instability effectively suppressing them and widening the pycnocline. Finally, at $\tau = 1.25$ (figure 3.12(iv)), the solitary wave continues propagating leftward and similar to figure 3.11(iv), the emergence of small shear instabilities within the solitary wave can be seen as it propagates. The evolution of this particular case is qualitatively similar to 15L5–8m but exhibits many more shear instabilities and is effected differently by dispersion.

By making the layer depths drastically asymmetric, clear solitary waves were seen to form. Qualitaitvely speaking, this was initially seen in figure 3.2 and 3.3 but on a much longer non–dimensional timescale. Thus, it is expected that the rate at which these waves form is due to the initial dimensionless amplitude. This is made clear in the laboratory experiments [22] as well as the qualitative results presented above. Clearly, the formation of a solitary wave train happens very quickly in the cases described above. This mechanism takes energy from the large scale seiche [22, 7], which results in different dynamics than a simple standing wave. What is also common between these two cases is the development of

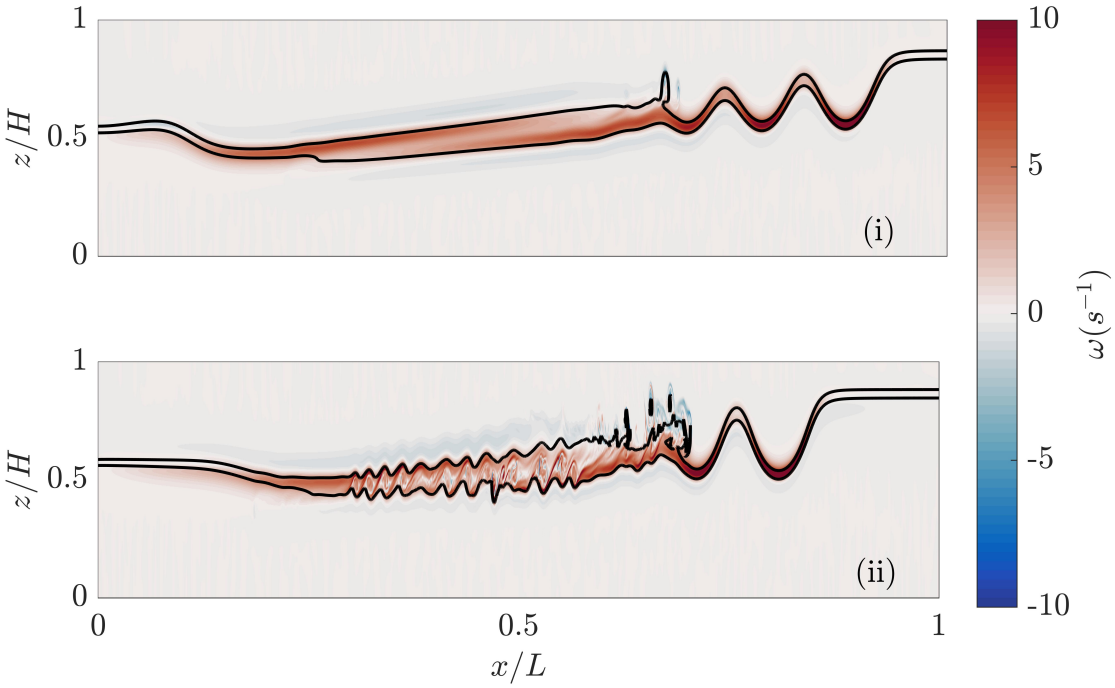

Figure 3.13: The vorticity field for the 15L5–8m (top) and 25L5–8m (bottom) cases at $\tau = 0.7$. The black contours are two representative isopycnals.

small shear instabilities within the leading solitary wave as it passed through the relatively quiescent region of the tank. This sort of instability was pointed out by Grue et al. [17], studied in Barad and Fringer [2] and then by Carr et al. [11].

The differences in how energy is distributed can be motivated by looking at the vorticity and the KE fields for the two skew cases described above. In figure 3.13, the vorticity field for the 15L5–8m and 25L5–8m cases at $\tau = 0.7$ is shown. Considering the vorticity field for 15L5–8m in 3.13(i), most of the vorticity is positive due to the background oscillation of the seiche and is especially intense at the peaks of the rightward propagating solitary wave train. When compared with the vorticity for the 25L5–8m case, 3.13(ii), it is clear that the pycnocline has been disturbed much more by the instabilities but that the vorticity field is otherwise similar to the 15L5–8m case. The main difference between these two cases is that due to the formation of the shear instabilities in the 25L5–8m case, there are small scale variations of vorticity within the pycnocline, while in the 15L5–8m case, the pycnocline is free of small scale variation in vorticity. Similar to symmetric cases, the vorticity is mainly

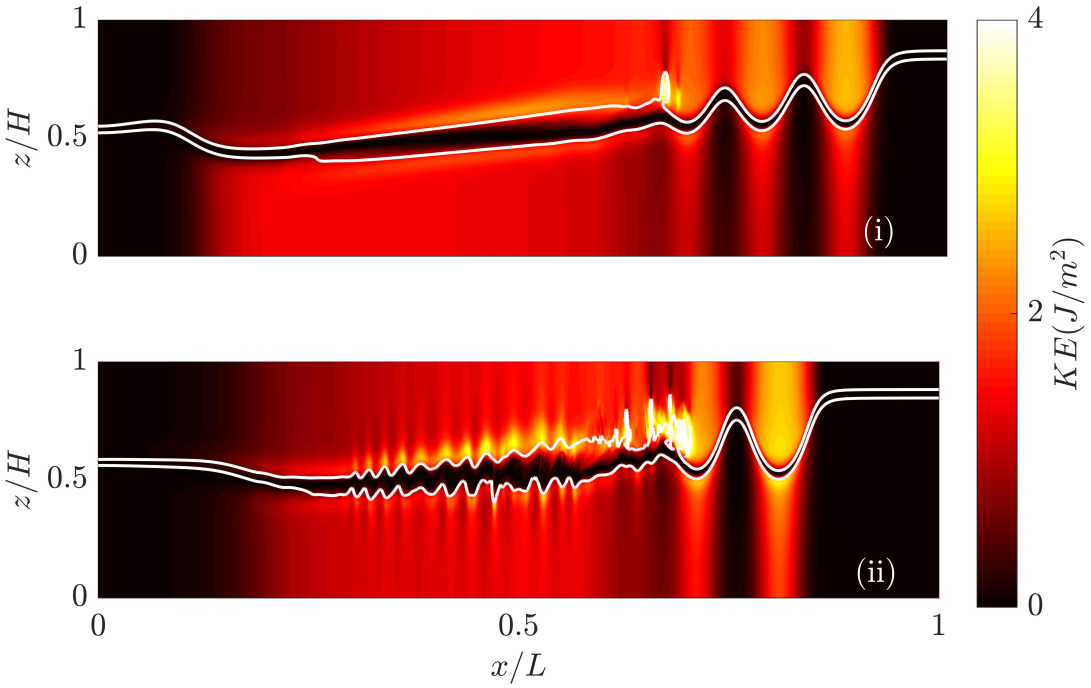

Figure 3.14: The KE field for the 15L5–8m (top) and 25L5–8m (bottom) cases at $\tau = 0.7$. The black contours are two representative isopycnals.

confined to within the pycnocline.

Figure 3.14(i) shows the KE for the 15L5–8m case. Most of the KE is in one contiguous region and is mostly absent from the pycnocline. This behaviour is similar to the L5–8m case. However, on the righthand side of the domain, there are intense vertical bands of KE following the propagating waves. Though the KE was seen to be in a similar configuration in the L5–8m case, for the 15L5–8m case, the symmetry about the node has been lost. Figure 3.14(ii) shows the KE of the 25L5–8m case. There is some small scale KE near the centre of the domain due to the formation of the shear instabilities as well as the characteristic intense vertical bands of KE at the peaks of the rightward propagating solitary waves.

Common to both of these cases is the fact the KE forms in vertical bands due to the propagating solitary waves. This behaviour is qualitatively similar to the L5–8m case and mostly absent from the L5–2m case which suggests that this phenomenon must be related to the length of the initial wave. The vertical bands are more intense for the skew cases than for the symmetric cases suggesting that the propagating solitary waves have a higher energy density than the dispersive waves in the L5–8m case. In the 25L5–8m case, there are two clear bands of KE due to the solitary wave train, but for the 15L5–8m case, there are 3. As was commented upon earlier, dispersion is strongest when the layer depths are equal. Thus, it makes sense that as the layer depths approach $H/2$, dispersion should create more rank ordered waves.

The vertical mean of KE for the 15L5–8m case is shown in figure 3.15(i). Notice first that by making the layer depths unequal, the symmetry about the centre of the tank that was seen in figures 3.10(i) and (iii) begins to look like the SA–35 in figure 3.4. The dispersive behaviour of these wave trains in the second to fourth lobes is evident because of the "streaking" nature of the vertical mean of KE, similar again in nature to figure 3.4. The most noticeable difference is the number of streaks that are present suggesting that dispersion is stronger in the large amplitude cases than in the small amplitude cases. The reason for this is because the large amplitude cases are more non–linear due to the largeness of the amplitude of the solitary wave. This means that there is more rapid steepening allowing for dispersion to occur earlier in the evolution. By the third lobe, between $\tau = 1$ and $\tau = 1.5$ the KE has broken down into about 5 or 6 streaks and in the fourth lobe, between $\tau = 1.5$ and $\tau = 2$, the KE has dispersed less, but appears to still be propagating back and forth in the domain. The dispersive behaviour carries over from the L5–8m case, but the difference here is the obvious asymmetry of how the KE evolves in space–time. Looking now at figure 3.15(ii), similar to the L5–8m case, there is a disparity between the low mode and total KE due to the dispersion of the large scale wave. However, the qualitative oscillatory nature of the KE is still present much like the earlier

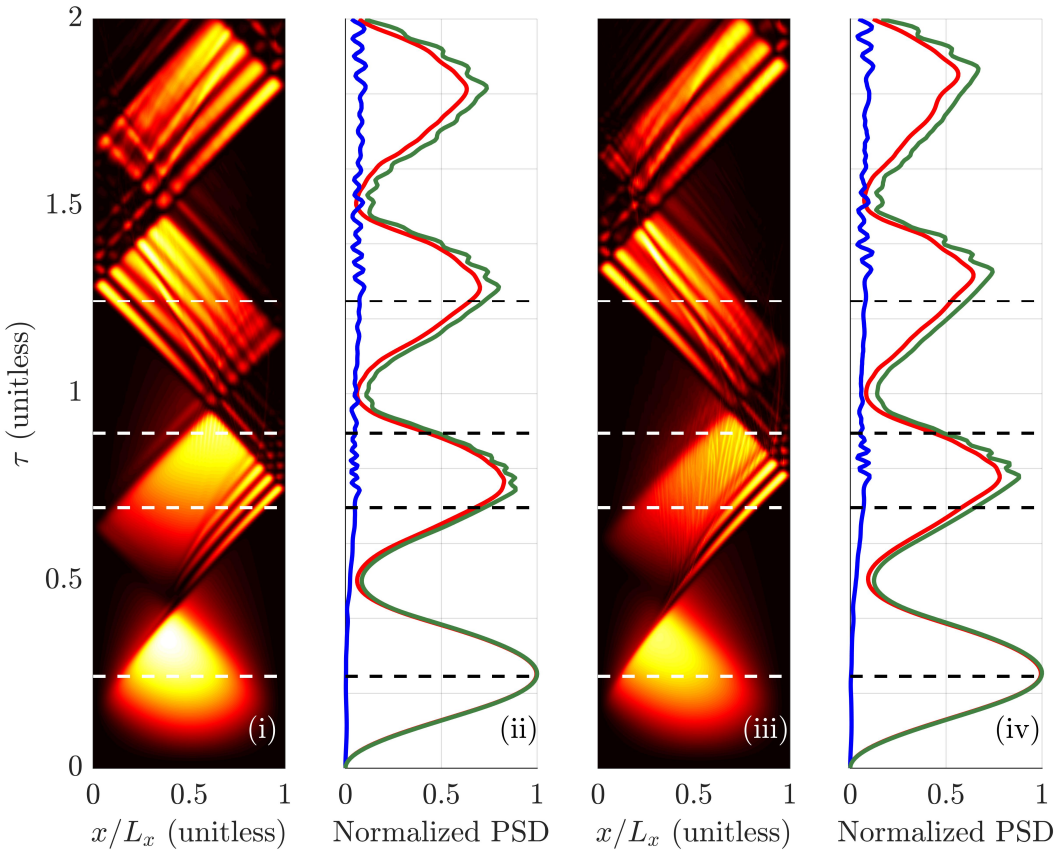

Figure 3.15: As in figure 3.4 but for the 15L5–8m (panels (i) and (ii)) and 25L5–8m (panels (ii) and (iv)) cases.

cases mentioned. There is a larger contribution from the higher modes in this case when compared to the symmetric cases. This is hinted at in figure 3.4 because SA–35 showed more of a contribution from the higher modes than SA–2 (for instance) suggesting that the dimensionless amplitude has a hand in controlling this.

Now consider the vertically integrated KE for the 25L5–8m case in figure 3.15(iv). There are many qualitative similarities to the 15L5–8m case such as the formation of the streak–like patterns due to the formation of the solitary wave train and general periodicity of the vertically integrated KE. There are some differences that are evident as well such as the weaker dispersion mentioned earlier, denoted by the fact that there are fewer streaks present in the plots because of the formation of fewer solitary waves. Between non–dimensional times $\tau = 0.5$ and $\tau = 1$, very thin bands of KE are evident that move very slowly across the domain in the wake of the solitary waves. These are the Kelvin–Helmholtz instabilities that are seen near the centre of the tank in figure 3.12(ii). Finally, in figure 3.15(iv), similar to 15L5–8m there is a disparity between the total KE and the low mode KE. The high horizontal modes have a similar proportion of the total KE to that of the L5–8m and 15L5–8m cases further suggesting that the way those modes gain KE is through a process dependent on the length of the initial wave.

Common to both of the skew cases discussed is the dispersion mechanism which is illustrated in both figure 3.15(i) and (iii) by streaking pattern that propagates back and forth in the tank. Similar dispersive behaviour is seen in the L5–8m (figure 3.10(iii)) case as well which suggests that this particular phenomenon is primarily dependent on the length of the domain while the degree at which dispersion occurs is due to the relative layer depths. Dispersion is most effective when the layer depths are equal and becomes less effective as the layer depths differ more. The reason for this is that the dispersive term in the classical 2–layer KdV equation is a maximum when the layer depths are equal [19]. Due to the dispersion, another similarity is the greater contribution to the total KE from the higher horizontal modes especially at traditional KE maximums ($\tau = 0.75$,1.25 and 1.75).

These results share similarities with the results presented in Horn et al. [22] and Boegman et al. [7]. Figure 2 in Horn et al. [22] shows in parameter space the dominant degeneration mechanism of the seiche. Much of the parameter space is occupied by what they label as "solitons", meaning that in most cases, solitary waves will occur and move energy around the basin. However, what figures 3.6, 3.7, 3.11, and 3.12 show is that there is typically more than one degenerative mechanism that may occur over the course of the early evolution of these waves. For instance, the only case where Horn et al. [22] saw KH billows was the case with equal layer depths and a large initial amplitude, but clear billowing was seen in 3 of the four cases discussed in this chapter. The aspect ratio of the tank

also appears to play an important role in which degeneration appears (at least initially). The L5–2m and L5–8m case have the same relative layer depths and initial amplitude but clearly have different dominant degeneration mechanisms.

3.4.3 Development of static instabilities

As a small aside, seen in a number of the large amplitude cases is the development of wisp–like features above and below the pycnocline after the first half period of oscillation. Below is an example of the appearance of these wisps in the L5–8m case. For this case, the average depth of the pycnocline in this case allows for the formation of wisps above and below the pycnocline in a roughly symmetric manner. These wisps advect outwards and form static instabilities where the pycnocline would otherwise be stable.

The instability creates a region in which $N^2(z) < 0$ which is an unstable stratification. This is qualitatively seen in figure 3.16. Panel (i) shows the the entire domain at $\tau = 0.9$, panel (ii) shows the region within the white box in panel (i) which gives a better view of the instability. In panel (iii), the instability in the density field is shown in the same location as in panel (ii) but at $\tau = 0.98$. At this time, there are some small disruptions on the pycnocline due to the unstable stratification. The interesting effect of this instability arises when looking at the vertical velocity field. Figures 3.17(i)–(iii) show the vertical velocity of the fluid at the same times as figure 3.16. Before the instability triggers, the vertical velocities are mainly large scale, but when the instability occurs, the induced velocities appear to be on the same order as the vertical velocities in the rest of the domain but are much smaller scale. The L5–8m case shown here is not the only case to exhibit these kinds of instabilities. Similar features appear in the asymmetric cases as well but only on one side of the node.

3.4.4 Energetic comparison of the large amplitude cases

The above discussion is meant to be a qualitative analysis of a subset of representative large amplitude cases. Now, a quantitative discussion can be performed describing how they relate to one another as well as other cases that were not shown above.

Figure 3.18 shows the KE per mode, as in figure 3.5 except for horizontal modes 2 to 17.

In the first panel, figure 3.18(i), the results for case L5–2m are shown. Horizontal mode–2 is clearly dominant for the first half period but is obviously losing KE as the

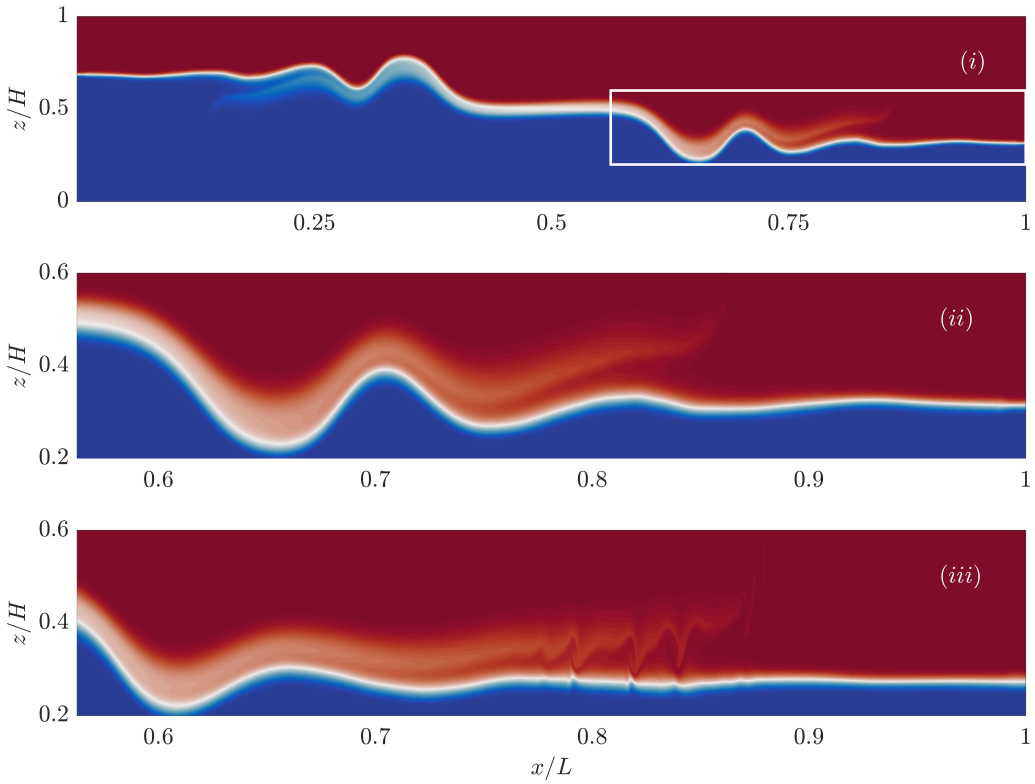

Figure 3.16: An example of wisps in the density field of the fluid. Panel (i) shows the entire domain at $\tau = 0.9$, panel (ii) is the region in the white box in panel (i) blown up at $\tau = 0.9$, and panel (iii) shows the same region as in panel (ii) but at $\tau = 0.98$.

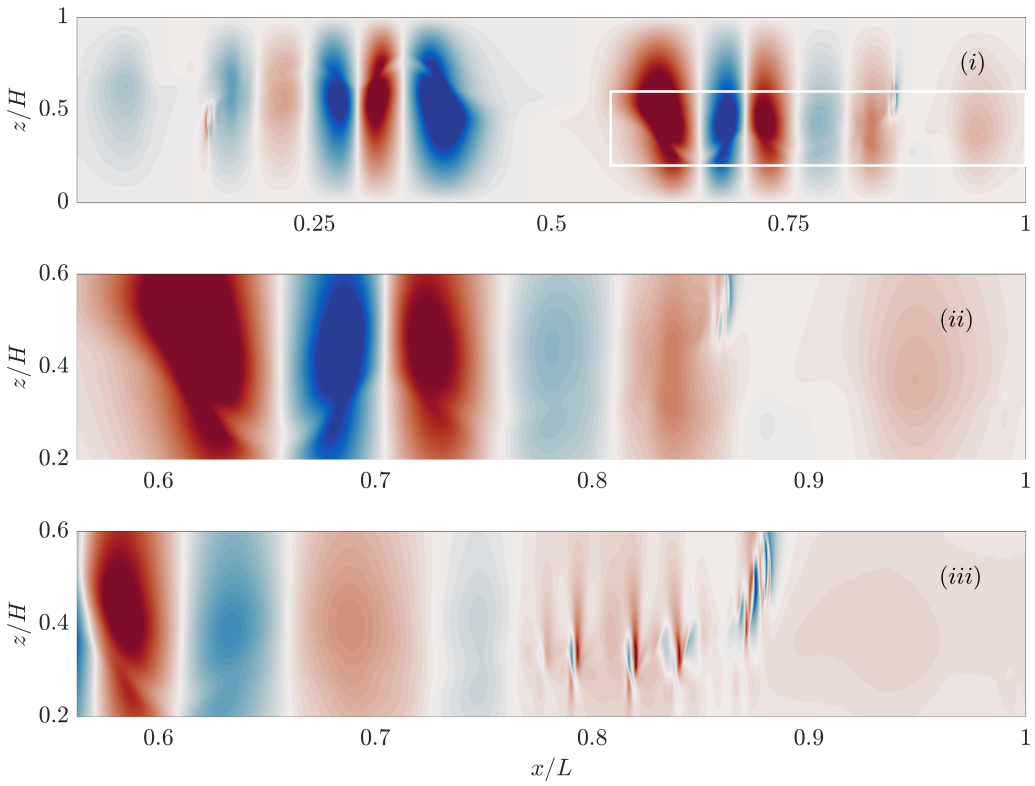

Figure 3.17: As in figure 3.16 but the vertical velocity field, w.

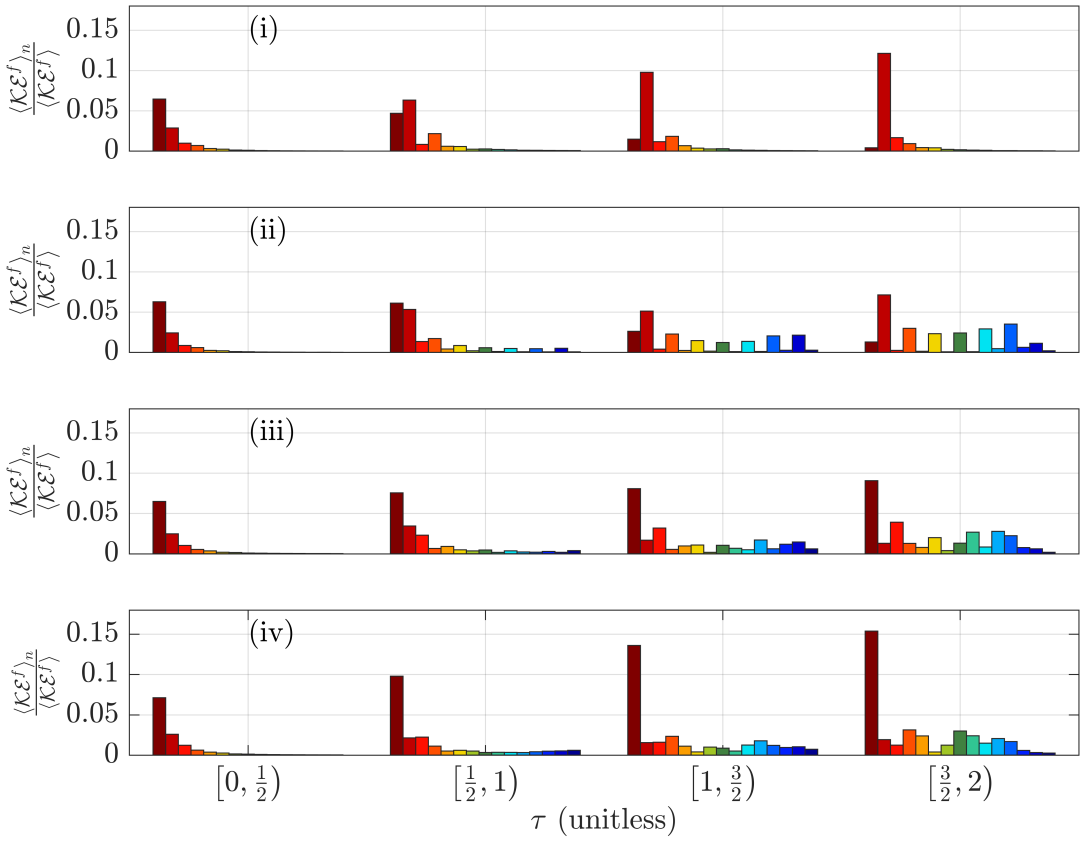

Figure 3.18: As is figure 3.5 but for horizontal modes 2 to 17. Again, horizontal mode–1 is ignored because it comprises most of the KE and thereby skews the plots. Panel (i) shows the results for L5–2m, panel (ii) is for L5–8m, panel (iii) is for 15L5–8m, and panel (iv) is for 25L5–8m.

seiche oscillates. This decrease in energy is accompanied by an increase in KE in other modes (especially in mode–3) suggesting that non–linear effects occur within the first half period of oscillation of the seiche. For all higher modes, there is a consistent decay in KE except for horizontal mode–5, which slightly increases in KE during the time interval $\tau = \left[\frac{1}{2}\frac{3}{2}\right]$. Over the first two seiche periods, horizontal mode–3 attains no more than 15% of the total KE available over that time interval but is clearly dominant over the rest of the modes shown. Since horizontal mode–3 attains more KE than mode–2 had to begin with, it is clear that some of this energy must have come from the mode–1 seiche. For this particular case, it seems that the KE is dominated by the two lowest *odd* modes. In the second panel, 3.18(ii), is the KE modal breakdown for case L5–8m. Much like L5–2m, mode–2 still loses KE over time and mode–3 gains some of it. What is notably different in this case is that mode–3 does not gain as much KE as was the case in L5–2m, but that the higher *odd* modes seem to be excited too. Interestingly, the higher even modes have almost none. Qualitatively speaking, this behaviour is reflected in the state of the density interface in figure 3.7(i)–(iv) because of the development of horizontal mode waves oscillating at higher frequencies. It is worth briefly drawing an analogy with the classical Stokes wave here [24]. The Stokes wave solution expands a finite amplitude wave as a trigonometric series in non–dimensional amplitude and wave number. A standing Stokes wave could be obtained by superimposing two counter-propagating Stokes waves. Typically, for surface waves the first three terms of the approximating series are given in the expansion of the free surface. The coefficients decrease monotonically, meaning that any non-monotonicity in the bar graphs shown in figure 3.18 can be taken as an indication that the motion in the simulations is more complex than a Stokes wave.

Next, looking at figure 3.18(iii), there appears to be different behaviour in how different modes become excited in the 15L5–8m case. The first difference to note is that horizontal mode–2 grows in this case. Though figure 3.18(ii) shows that the L5–8m case initially gains some relative KE, the growth of horizontal mode–2 is different behaviour than either L5–2m or L5–8m. In those cases the even modes were ultimately seen to lose KE with time. As well, there seems to be no pattern on how higher modes gain KE besides the fact that they *all* gain energy compared to the distribution during the first time interval. Finally, in the 25L5–8m case, we notice that the intermodal energy flux is qualitatively similar to the 15L5–8m case, albeit with the second horizontal mode making up a greater proportion of the total KE at that time. Much like the 15L5–8m case, there is a broader excitation of horizontal modes. As well, the KE appears to be spread to the higher modes with no clear bias towards odd or even modes. These figures serve to show that energy moves to smaller scales relatively quickly during the evolution of the seiche.

What figure 3.18 serves to show is that non–linear effects due to a disparity in the layer

depths quickly affect the spatial distribution of the KE. However, what is interesting is the way in which the KE is distributed when non–linear effects due to the layer depths are not present. Since different modes are becoming excited with time, non–linear effects still occur, but appear to be determined by the aspect ratio of the seiche rather than a classical non–linearity due to a relative difference in the layer depths. However, the behaviour of the KE changes very quickly when non–linearity due to the relative layer depths is present suggesting that the dependence of the spatial distribution on the aspect ratio may be a second order effect.

Due to the fact the the aspect ratio and the dimensionless amplitude of the initial condition appear to affect which horizontal modes are excited with KE, it is of use to discuss how these changes are manifested in the spatial distribution of the APE of the seiche. Here, the development of a model for phase plane behaviour of a parameter measuring the decay of the first horizontal mode (the fundamental mode) of the seiche is discussed. This parameter is defined as $\lambda(W^{-1}, \mu)$ and is inferred from simulations by isolating the time series data of the APE contribution from the first horizontal mode of the seiche. The value of the peaks and the times at which they happened in terms of the time scale in equation (3.4) are calculated and the value of the parameter follows.

Once the seiche has been converted from a continuously stratified model to a two layer model, spectral analysis can be used to partition potential energy into different horizontal modes. Hypothetically speaking, the contribution of every mode could be discussed, *but* more can be learned if only the lower horizontal modes are considered, much like the discussion regarding figures 3.5 and 3.18. This can help build an understanding of which modes are excited during the evolution of the seiche. Initially speaking, the first horizontal mode of the seiche contains all the APE, thus, a model for the APE in the first mode is proposed as follows:

$$E_a^{(1)} = APE(0)e^{-\lambda\tau}\cos^2(2\pi\tau)\,. \tag{3.6}$$

Here, $APE(0)$ is the initial APE input and λ is an APE decay rate. The two–layer APE is calculated by first determining the isosurface that is represented by the reference density, ρ_0, and then approximating the lower layer as everything below this isosurface and the upper layer as everything above this isosurface. The density of the lower layer is approximated as ρ_2 and the upper layer density as ρ_1. This parameter itself is assumed to be a function of two non–dimensional bulk parameters, $W^{-1} = \eta_0/h_1$ and $\mu = H/L$, these being the dimensionless amplitude (or inverse Wedderburn Number [22, 14]) and the aspect ratio of the tank. Once $\lambda(W^{-1}, \mu)$ is calculated for each case, a model for how it changes in parameter space is developed to build an understanding of how the behaviour

of fundamental mode of the seiche is affected by the initial condition. Building a model for the decay parameter is fairly straightforward. The first step is to simply take W^{-1} as constant for the moment and define

$$\ln(\lambda) = R_1(W^{-1})\mu + R_0(W^{-1}) \tag{3.7}$$

where R_1 and R_0 are constants and are dependent on the choice of W^{-1}. The constants of integration are calculated via linear fits to the data. By calculating $\lambda(W^{-1}, \mu)$, there is now a general rule for how the fundamental mode of the seiche loses APE in $W^{-1} - \mu$ parameter space. This gives an indication of the timescale on which the large scale seiche degenerates into higher mode waves and how fast non–linear effects become present in the flow.

In figures 3.19(i) and (ii), the rate of decay of the APE in the first seiche mode is shown. Considering first how it changes with aspect ratio (figure 3.19(i)), for all cases with constant W^{-1} the decay rate of the mode–1 seiche decreases. Since these curves are decreasing with aspect ratio, the rate at which APE is decreasing in mode–1 is faster per period for longer seiches than for shorter seiches. These results agree qualitatively with the plots of the density fields in figure 3.6 and 3.7 because of the absence of higher mode deflections of the density interface in the L5–2m and the presence of them in the L5–8m case. Physically, the breakdown of a seiche into non–linear dispersive wave trains is more efficient than small scale shear instability or localized overturning at extracting energy from the fundamental mode of the seiche. On the other hand, for all cases with constant aspect ratio in figure 3.19(ii), the rate at which APE is removed from the mode–1 seiche *increases* with increasing dimensionless amplitude. As the dimensionless amplitude becomes larger, the rate at which energy leaves the first horizontal mode has a weaker dependence on the aspect ratio of the wave, denoted by the clustering of the points of the aspect ratios, but as the dimensionless amplitude decreases, the variation of the rate of change of APE is reasonably large.

Using the definitions for R_0 and R_1 from the analysis discussed above, a linear regression as a function of the dimensionless amplitude is carried out with the results shown in figure 3.19. The legend for panel (i) gives the explicit values of the dimensionless amplitude. R_1 is found to depend on W^{-1} linearly, as shown in figure 3.20(i). From figure 3.20(ii), R_0 also depends nearly linearly on W^{-1}. There is some spread in the markers, where each marker denotes a different aspect ratio, thus the constant R_0 also depends weakly on the aspect ratio, but not enough to warrant further analysis. Since both R_1 and R_0 are dominated by variation of W^{-1} the fit allows for a complete closed form model of $\lambda(W^{-1}, \mu)$, equation (3.7) as

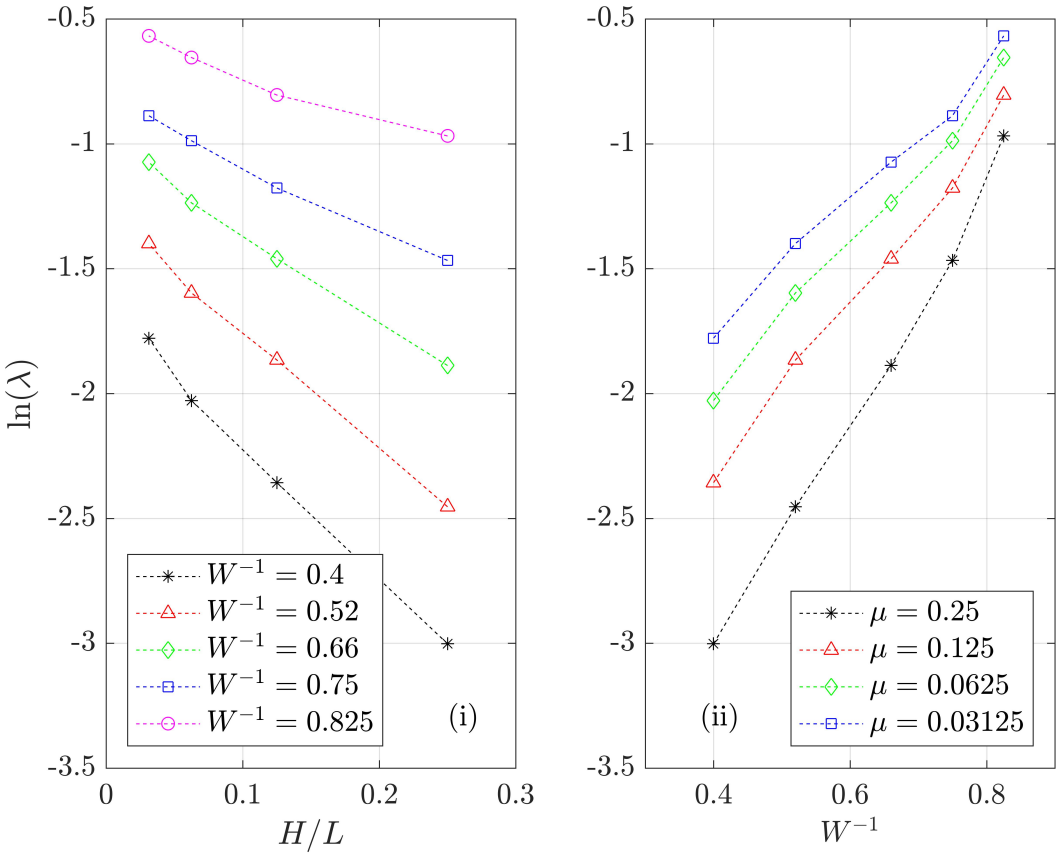

Figure 3.19: The logarithm of the decay parameter λ calculated via linear regression of the maximums of horizontal mode–1 potential energy, as a function of the dimensionless amplitude η_0/h_1 and aspect ratio $\mu = H/L$.

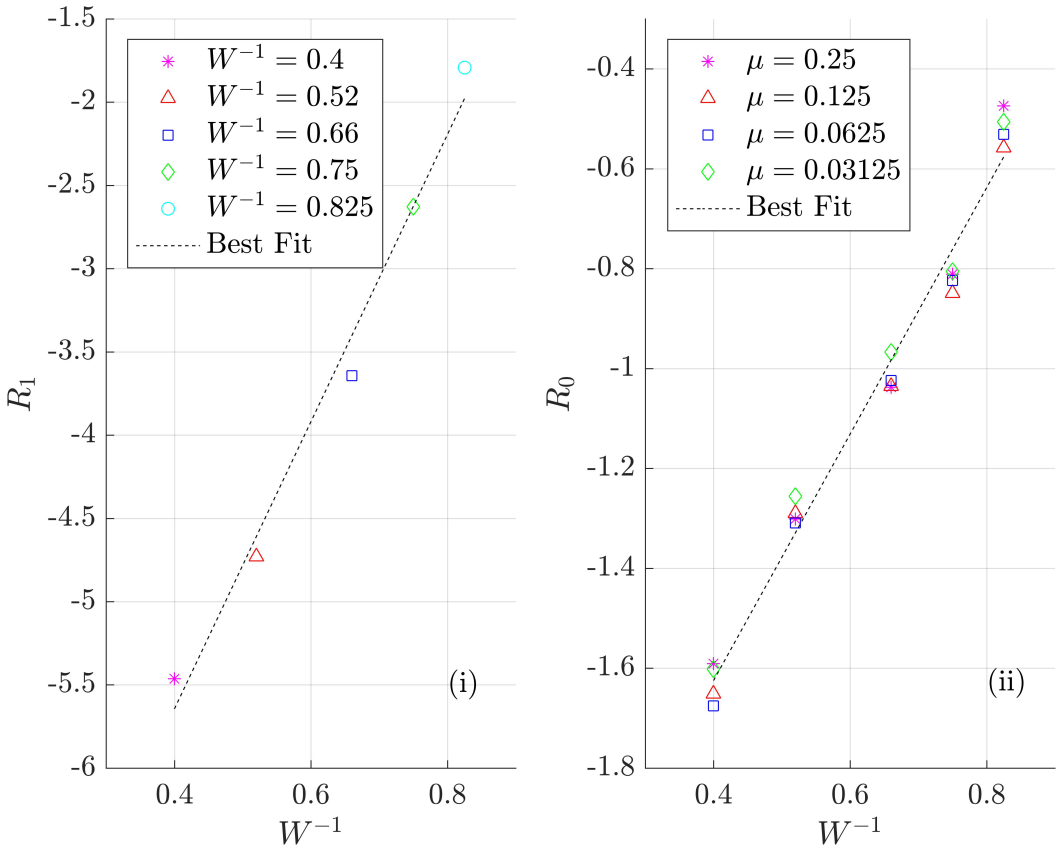

Figure 3.20: The fitting Parameters for the model of $\lambda(W^{-1}, \mu)$

$$R_0 = k_1 W^{-1} + k_2 \tag{3.8}$$

and

$$R_1 = r_1 W^{-1} + r_2 \tag{3.9}$$

The values for k_1, r_1, k_2, and r_2 under a 95% confidence interval are presented in table 3.4.

Table 3.4: The fitting parameters as discussed in the text.

Parameter	k_1	k_0	r_1	r_0
Value	2.5 ±0.14	-2.6 ±0.10	8.6 ±1.5	-9.1 ±0.96

In figure 3.21 is shown how λ changes in parameter space and where each of the cases performed for this study lies in the model. From figure 3.21, the decay rate is seen to be lowest at high aspect ratios and low dimensionless amplitudes, which agrees with the data from figures 3.19(i) and (ii). The model also agrees with the notion that at high dimensionless amplitudes and low aspect ratios, the potential energy leaves the first horizontal mode of the seiche fastest.

Plotted in figure 3.22 (see caption for details) is the potential energy calculated via equation (2.76) and the decaying part of the model in equation 3.6 for the 25L5–8m case (black) and the L5–2m case (red). The model predicts the decay of the mode one energy reasonable well, over estimating the decay parameter for 25L5–8m and under estimating for the L5–2m case. It is necessary to note that even the decay parameter calculated via linear regression from the peaks of the mode–1 data does not exactly replicate the peaks themselves due to the fact that the APE in mode–1 is not *exactly* decaying exponentially. However, the model predicts the large scale decay of mode–1 energy fairly well for two fundamentally different cases.

3.5 Mixing

Most cases considered exhibit mixing of fluid from the upper and lower layers resulting in interfacial widening. For instance, at later times, figures 3.6(iv), 3.7(iv), 3.11(iv) and 3.12(iv) show that at least part of the pycnocline has become wider due to mixing of the upper and lower layers. In figure 3.23 the VMC (equation (2.93)) is plotted against the EMC (equation (2.86)) for several cases. Only the subset of cases denoted with L5*, 15L5* and 25L5* are considered here because the other cases only undergo very small amounts

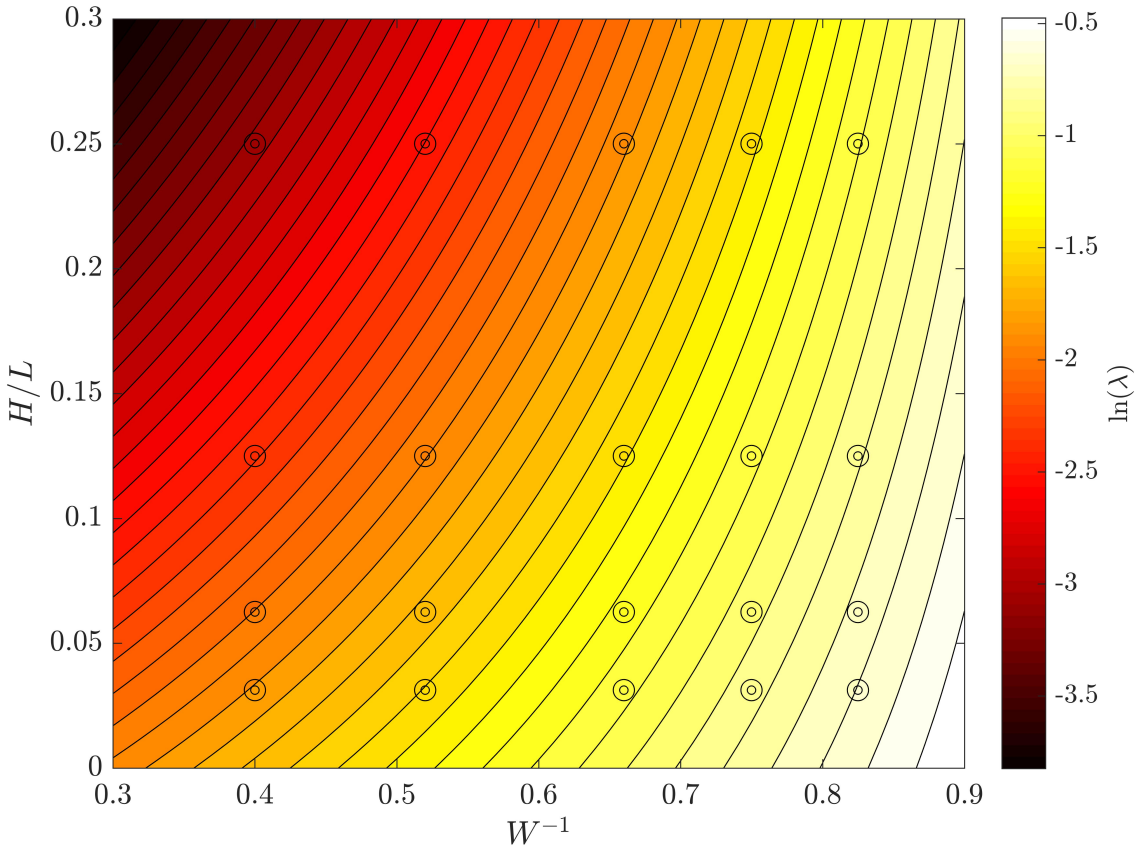

Figure 3.21: The variation of $\ln(\lambda)$ in (W^{-1}, μ) parameter space. Each circle corresponds to a particular large amplitude case and where it fits in the parameter space.

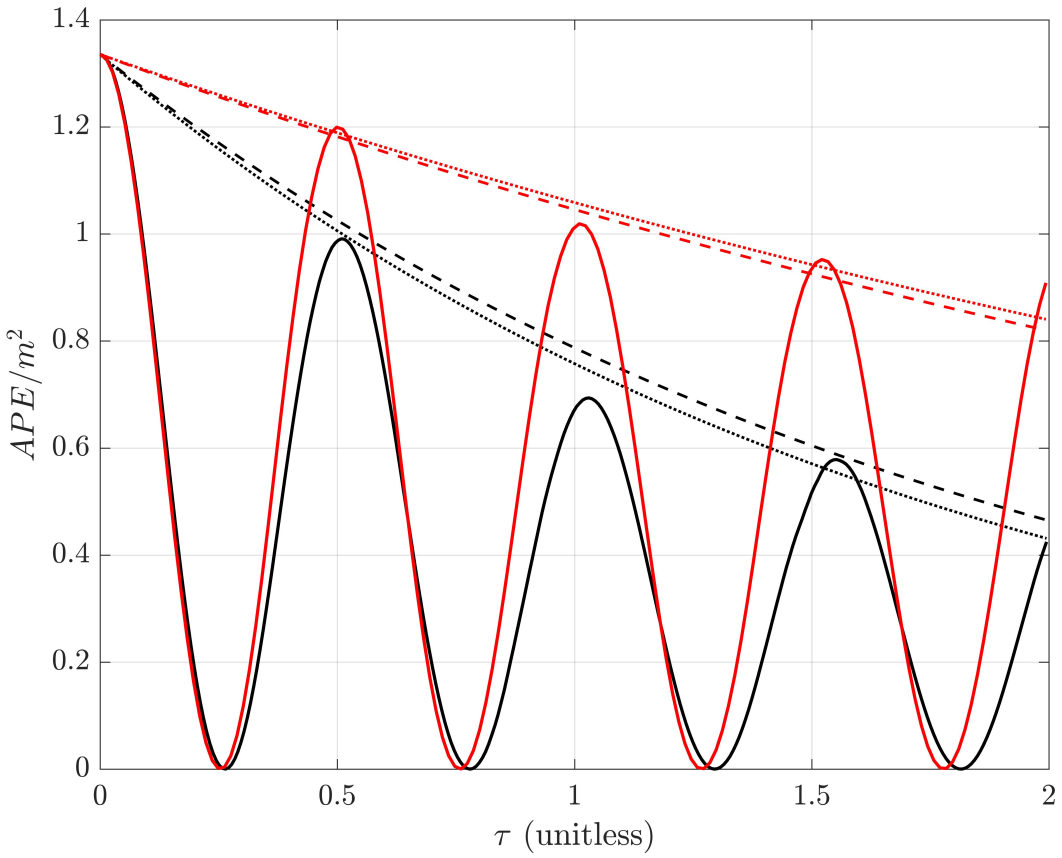

Figure 3.22: A comparison of the model decay parameter (dashed line) from equation (3.7) and the calculated decay parameter (dotted line) against the mode–one contribution to the APE (solid line)for two cases. 25L5–8m case is in black and the L5–2m case is in red. The oscillating component out of the model was removed because there is no decay in mode–1 APE built into the oscillating part.

of mixing and skew the plots. On each curve there are three markers, added to denote some measurement of time. The small circles denote $\tau = 0.5$, the medium circles denote $\tau = 1$ and the largest circles denote $\tau = 1.5$. The beginning and the end of the curve denote $\tau = 0$ and $\tau = 2$, respectively. First, some extreme scenarios are outlined: 1) if the VMC was totally independent of the EMC, then the curve would be a vertical line, 2) if the EMC was completely independent of the VMC, then the curve would be horizontal, 3) if one was just a scalar multiple of the other, then the curve would be a straight line of some non–zero slope.

First, consider figure 3.23(i), before the first half period, the slope of the curve is very steep with respect to the EMC. Physically speaking, the variability of the density field is undergoing a quick transition to uniformity. The reason for this is that all cases with $\mu = 0.25$ exhibit shear instabilities early in the evolution of the wave. Essentially, when the shear instabilities collapse, the high density gradients created by their steepening processes become smoothed out. Broadly speaking, this means that the second derivative of the density field is becoming large and thus, mixing occurs and a spike in the curve is seen. This behaviour can be seen for for all three cases with $\mu = 0.25$ as there is a relatively clear peak in all three of these curves. After the peak, the VMC is decreasing at a relatively constant rate while the EMC is still increasing. This suggests that density gradients are becoming smoothed out at a slower rate than before. By this time, the collapsing of shear instabilities has ceased and perhaps this increase in EMC is due to other effects such as diapycnal stress due to passing waves. The rate at which these density gradients are being smoothed appears to be different depending on the dimensionless amplitude. This is denoted by the approximate angle the curve makes with the EMC–axis after the peak.

By increasing the length of the tank, or reducing the aspect ratio to $\mu = 0.125$, there is a shift in how the VMC and EMC depend on the dimensionless amplitude, shown in figure 3.23(ii). At early times, there is a strong increase in the VMC before there is much of an increase EMC for all cases. There is an episodic nature to the VMC for the cases with $W^{-1} = 0.75$ and 0.825. This could be due to the fact that there is a coexistence of shear instabilities and propagating waves. The approximate episodic nature of the green and the blue curve (cases with unequal layer depths) suggest that the solitary waves that form due to this disparity play a role in how much the VMC and EMC increase. The lack of any sort of episodic mixing in the red curve (cases with equal layer depths) supports this theory as propagating waves did not quite form in this case. The blue and green curves initially begin to increase at approximately the same time that a solitary wave passes through a region of collapsed instabilities, accelerating the rate at which density gradients are smoothed out. Another important point here is that the normalized value of the VMC is not as large as the cases with $\mu = 0.25$, but the EMC has increased slightly in the $W^{-1} = 0.66$ and 0.75

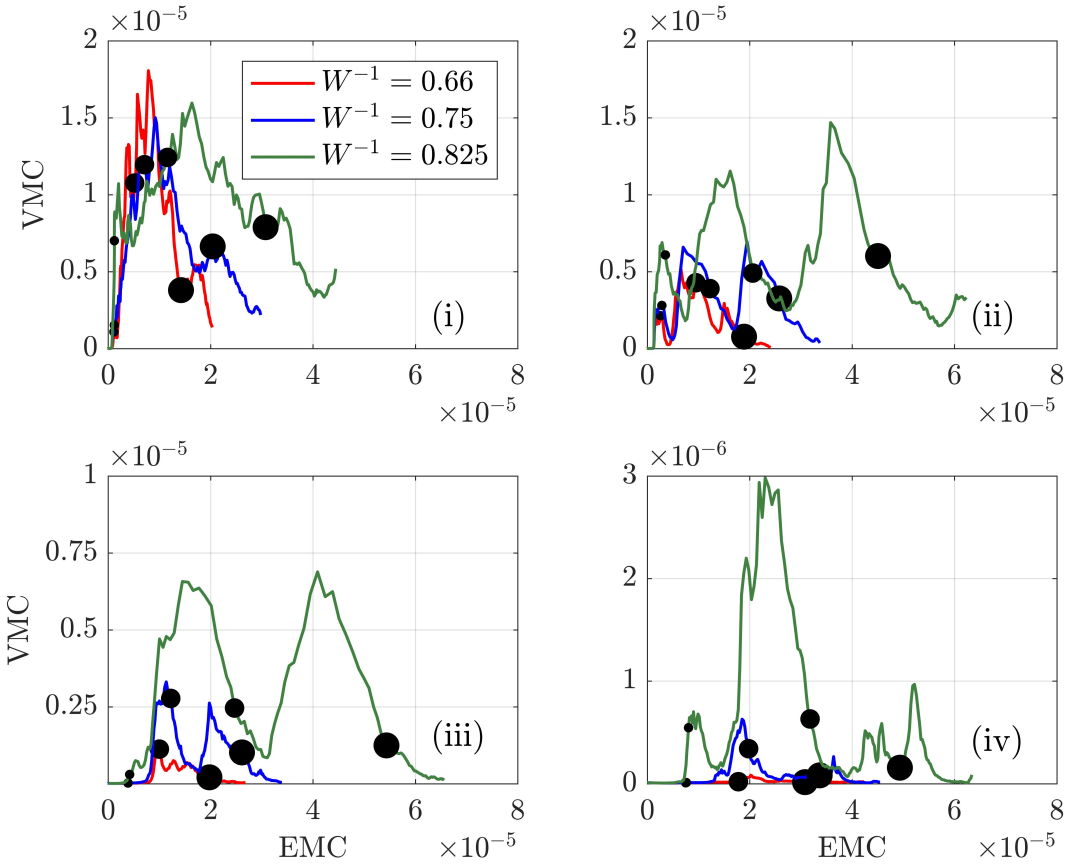

Figure 3.23: The Variability Mixing Characterization (VMC) plotted against the Energetic Mixing Characterization (EMC). The black markers on each plot depict the non–dimensional times $\tau = 0.5$, 1 and 1.5. Larger markers indicate later times. Subplot (i) is the cases where $\mu = 0.25$, (ii) represents $\mu = 0.125$, (iii) represents $\mu = 0.0625$ and finally (iv) depicts $\mu = 0.03125$. Red lines indicate $W^{-1} = 0.66$, blue indicate $W^{-1} = 0.75$ and green indicates $W^{-1} = 0.825$. Cases with $W^{-1} = 0.52$ and $W^{-1} = 0.4$ were omitted from this plot because they showed almost no VMC and very little EMC and complicate the plot.

cases and noticeably in the $W^{-1} = 0.825$ case.

In figure 3.23(iii) the curves for an increase in tank length, or reduction in the aspect ratio to $\mu = 0.0625$ are shown. Note the change in scale on the VMC–axis. What is immediately different is that there is a greater increase in the EMC before the mixing occurs for all cases. This is because the period of oscillation of the seiche is sufficiently long such that molecular diffusion can work to widen the pycnocline before any other mechanisms can contribute to an increase in the EMC. Similar to the cases in figure 3.23(ii), there is evidence of the episodic nature of the VMC due to instances of shear instabilities colliding with passing solitary waves for cases $W^{-1} = 0.75$ and 0.825. Similar to the $\mu = 0.125$ cases mentioned earlier, this phenomenon is not nearly as prevalent in the $W^{-1} = 0.66$ (red curve) case due to the fact that there is only one instance of shear instability and the waves that occur cannot accelerate the smoothing of the density field.

Finally, for the $\mu = 0.03125$ cases in figure 3.23(iv)(again, note the change in scale on the VMC–axis), the case with $W^{-1} = 0.825$ clearly undergoes the strongest increase in VMC when compared to cases with $W^{-1} = 0.66$ and 0.75 due to the distinct peak in the curve. Again this is probably due to the solitary wave interacting with the collapsed shear instabilities. In fact, cases with $W^{-1} = 0.66$ and 0.75 undergoes almost no change in the VMC suggesting that diffusive processes are dominating the increase in the EMC. Figure 3.7(iii) shows that there is only a small amount of widening near the node of the seiche at $\tau = 0.9$ but the pycnocline is otherwise smooth and there are no signs of shear instabilities. However, for the case with $W^{-1} = 0.75$, there is a small increase in the mixing suggesting that there may have been an instance of shear instability and solitary wave coexistence which could contribute to an increase in the EMC but does not clearly show up in the VMC. The confound here is that the shortest cases undergo the strongest increase in the VMC but the smallest increase in the EMC. For the longer cases where it is possible to form a propagating wave, there is an increase in the EMC and only a small episodic increase in the VMC.

In figure 3.24 is plotted the change in the BPE as a proportion of the initially available potential energy (see caption of figure 3.24). This gives a measure of the efficiency of energy transfer over the course of two seiche periods, because the majority of the energy available for mixing is due to the initial APE input.

Figure 3.24 shows that the efficiency of increase in the BPE is not a simple relationship between the aspect ratio and the dimensionless amplitude of the seiche. A possible mechanism responsible for increasing the efficiency in energy transfer to background potential energy transfer is the occurrence of the vigorous shear instabilities. Cases denoted by filled in markers are those for which Kelvin–Helmholtz instabilities are observed. Notice that

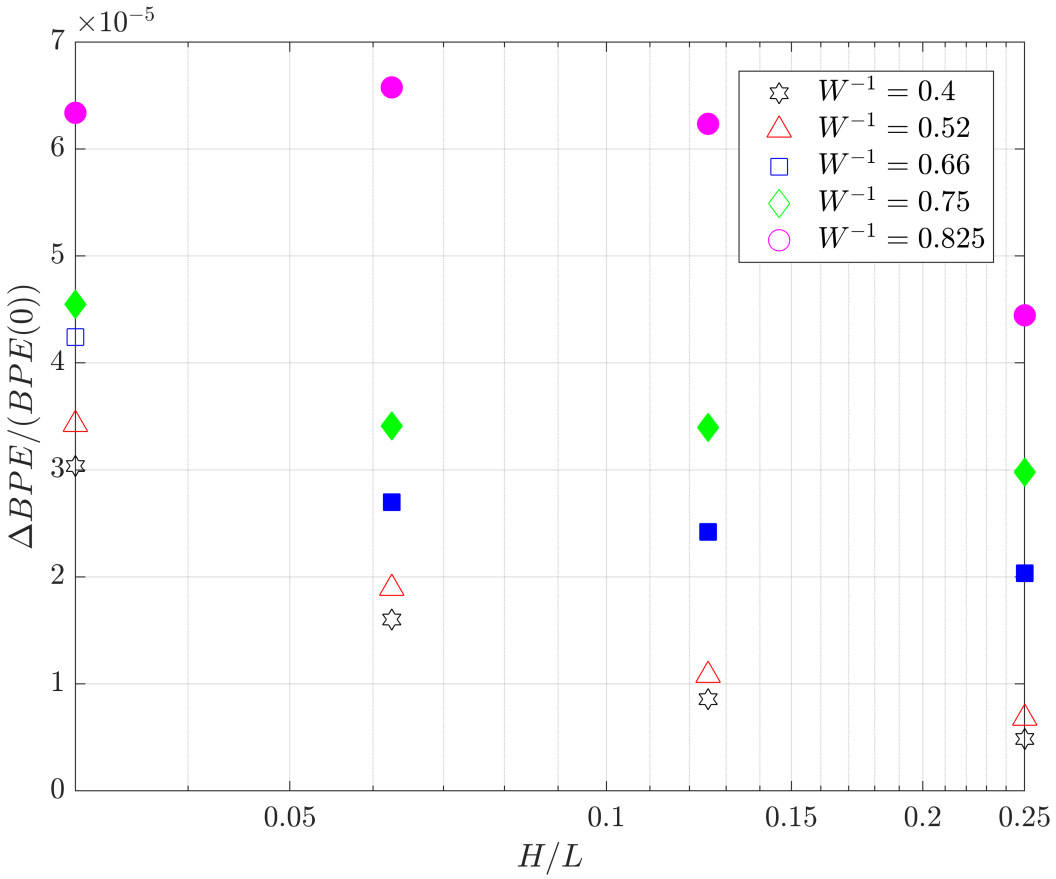

Figure 3.24: The change in BPE as a percentage of the initial BPE plotted against H/L. The change in BPE is taken as the final value BPE of the fluid at $\tau = 2$ minus the initial background potential energy. The points with the same marker shape are of equal W^{-1}. Read left to write, the aspect ratios of columns of points are $H/L = 0.03125$, $H/L = 0.0625$, $H/L = 0.125$, and $H/L = 0.25$. Filled markers are cases where Kelvin–Helmholtz billows are seen.

the increase in BPE of cases without Kelvin–Helmholtz billows decay exponentially with increasing aspect ratio. However, the cases where Kelvin–Helmholtz billows *do* appear do not fall off exponentially but instead appear to level off to some relatively constant value. That being said the character of the BPE increase completely changes for the case with the highest dimensionless amplitude, denoted by magenta circles ($W^{-1} = 0.825$). For the cases with $(W^{-1}, \mu) = (0.825, 0.0625)$ and $(0.825, 0.125)$ the interaction between shear instabili-

ties and propagating solitary waves was seen as opposed to the case $(W^{-1}, \mu) = (0.825, 0.25)$ where only shear instabilities were seen. In figure 3.12(ii), the solitary waves that form midway through the simulation are seen to work efficiently to widen the pycnocline and increase the BPE when they propagate through a region with shear instabilities. Case $(W^{-1}, \mu) = (0.825, 0.0625)$ has two distinct events in which the background potential energy increased dramatically while $(W^{-1}, \mu) = (0.825, 0.03125)$ exhibited only one.

Chapter 4

Conclusions and future work

4.1 Discussion

This thesis presents high resolution two dimensional pseudo–spectral simulations of internal seiches with two goals in mind. The first is to present a discussion regarding the temporal and spatial evolution of small amplitude seiches. The reason for this is to discuss the motion in a relatively controlled manner without added complications such as rapid non–linear steepening, mixing, and shear instability. Analyzing small amplitude seiches allows for a clean qualitative discussion of only the motion of the fluid and to put later results into context. The second goal is to focus on cases with large enough dimensionless amplitude to yield either significant Kelvin–Helmholtz billows in addition to trains of solitary like waves. None of the large amplitude simulations exhibit the formation of turbulent bores, and indeed most observations in lakes suggest that the formation of non–linear wave trains (i.e. undular bores) is a far more generic phenomenon. A particular focus of the study is on the change in behaviour as the aspect ratio is varied, and the way in which this change is manifested in the energetics and mixing. While the dynamics of small amplitude waves can be described with linear and weakly non–linear theories, the results of this thesis indicate that short tanks, or large aspect ratios, yield behaviour that is initially dominated by shear instability that sets in near the node of the standing wave. Increasing the tank length, or decreasing the aspect ratio, accelerates the process by which the standing wave breaks down in to a non–linear wave train. In many cases where the dimensionless amplitude and the length of the domain are sufficiently large, the formation of the wave train coexists with shear instabilities during the evolution, and there is enhanced mixing as the instabilities and waves interact. At field scales, rotation, atmospheric forcing and

topographic wave generation may have an order one contribution to the dynamics and the overall degeneration of the seiche, thus, simulating cases that large in the idealized conditions of this thesis is not worth the computational cost as many important characteristics of the flow may be missing. The dynamics described above are summarized as a schematic in figure 4.1.

In many cases for which billows do not occur (and even some cases that they do), development of statically unstable convective wisps is a common feature. As the initial tank scale wave approaches the end of its first period, these wisps are seen to advect outwards. They are seen in figure 3.7 immediately above and below the pycnocline and are discussed in section 3.4.3. As these instabilities move outwards, they induce small mode–2 like instabilities near the sides of the tank. The wisps also facilitate shear instabilities in a region with a weak unstable stratification when the large scale seiche induces shear that would otherwise be stable on its own. These wisps appear in cases where the layer depths are unequal as well. However, through various processes the horizontal density gradients are much higher in those cases, suggesting that the wisps are mostly disrupted by the wave induced currents.

In order to build an understanding of the energetics of the wavefield, spectral analysis of the KE is utilized to build a mode-by-mode understanding of the flow. This analysis is partially based on the analysis performed by Horn et al. [22]. Where they use an *a priori* method of estimating when the non–linearity of the system becomes important, here, an *a posteriori* method based on spectral decomposition of the KE is used, where non–linear effects are said to become important when higher horizontal modes become excited due to various mechanisms. With the large amplitude cases discussed in the second section of the previous chapter, the development of a solitary wave occurs very rapidly in the evolution of the seiche because the layer depths are unequal and the amplitude is sufficiently large. Thus, non–linear effects appear early in the evolution of the large amplitude cases. For the small amplitude cases discussed in that chapter, the development of the solitary wave train took much longer due to the fact that the dimensionless amplitude is small and therefore the timescale associated with non–linear steepening is much longer. To some degree, the development of the solitary–like waves was seen in almost every case considered. For the sake of comparison, most of the cases considered in [22] fall into a regime in which the dominant degeneration mechanism is the formation of a packet of solitary waves.

To complement the analysis for the KE, a semi-analytical model is developed which gives an estimate as to the rate at which APE is irreversibly removed from the fundamental mode of the seiche. The main results of this method predict that there will *always* be some sort of energy transfer between modes. Though viscosity is not explicitly accounted for in this analysis, at early times, the model is reasonably representative of the decay of APE from

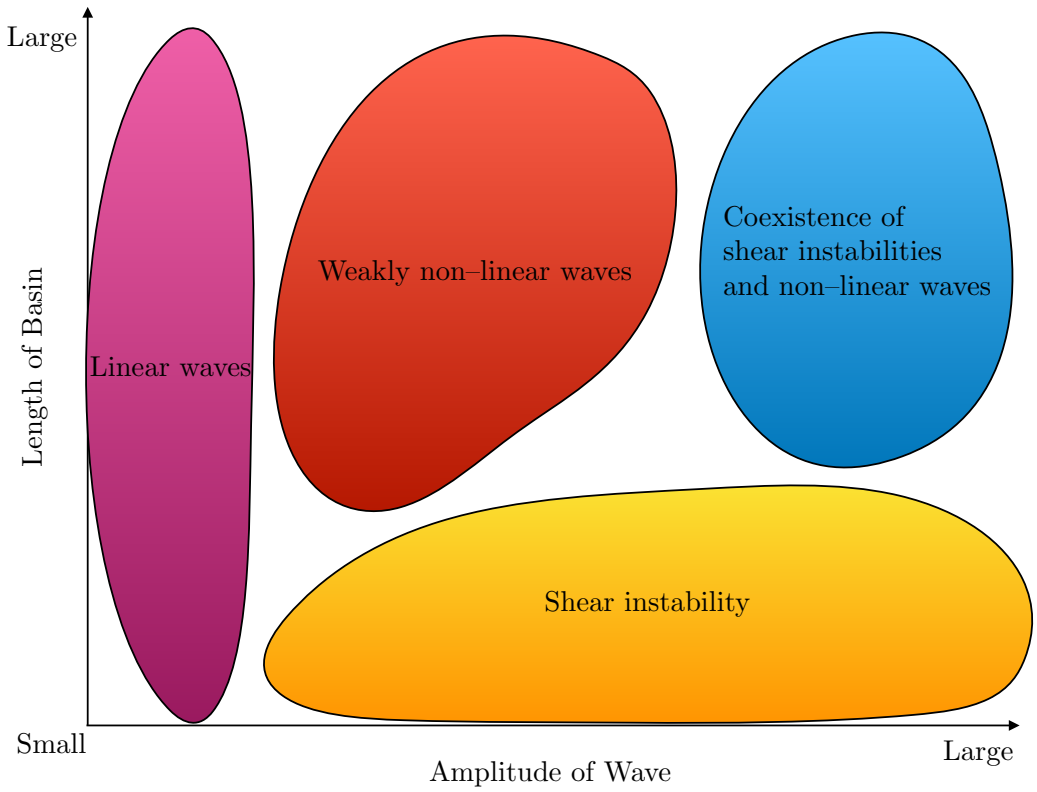

Figure 4.1: The proposed degeneration regime diagram for a laboratory scale seiche. For small amplitudes, linear theory and weakly non–linear theory apply and are mostly independent of aspect ratio of the tank (small amplitude cases). For large amplitude and reasonably short tanks, shear instabilities form (L5–1m, L5–2m). For mid-length and mid–amplitude waves, wave trains form and for longer tanks with large amplitudes, both shear instabilities and wave trains form (15L5–4m, 15L5–8m, 25L5–4m, 25L5–8m).

the large scale seiche. The results of this model quantify the fact that the available potential energy leaves the fundamental mode faster for cases with a larger dimensionless amplitude and slower for a smaller dimensionless amplitude. This agrees with the qualitative results from figures 3.6, 3.7, 3.11 and 3.12 as well as with the analysis of Horn et al. [22] and Boegman et al. [7].

A discussion of the quantitative analysis of the mixing that the density field undergoes is also provided. The paradigm that figures 3.23 and 3.24 demonstrate contains two parts, one is the dependence of the amount of mixing on the wavelength of the seiche and the second is the dependence on the amplitude.

Under certain conditions, the coexistence of shear instabilities and solitary waves enhances the amount of mixing that occurs and the results in chapter 3 show that there is a dependence on the initial wavelength of the seiche given a sufficient amplitude. There are two mechanisms that contribute to this behaviour. The first, and slightly less vigorous case occurs when, due to non–linear steepening, shear produced at the peak of the resulting solitary waves can be enough to overcome the stratification and result in the formation of small shear instabilities which mix upper and lower fluid layers. Troy and Koseff [52] showed through a series of parallel flow experiments that the emergence of Kelvin–Helmholtz instability is dependent on the ratio of timescales of the steepening of the instabilities to the wave period of the waves being considered. Others showed that the development of the instabilities within the solitary waves were related to the length of the wave and the length of the region that is subject to a gradient Richardson number less than 0.25 [2, 11, 26]. The second and more dominant mechanism is the shear produced due to the fluid layers moving past each other from the large scale oscillation of the seiche. The shear is typically enough to overcome buoyancy and allow for the formation of vigorous shear instabilities which can be smoothed out by passing waves. This behaviour leads to multiple mixing events over the course of the evolution of the seiche.

Alternatively, when only shear instabilities are allowed to form there is only typically one mixing event, as seen when comparing figures 3.23(i) and (iv). The effect may solely be due to the fact that there are shear instabilities in the L5–1m case while there are no such instabilities in the L5–8m case. When both shear instabilities and solitary waves appear together the amount of mixing due to the shear instabilities is enhanced due to the passing solitary wave.

The second point is that the overall change in BPE certainly depends on the dimensionless amplitude. This is the case for two reasons. The first is that with a higher dimensionless amplitude, there is a larger initial APE. This energy can either be transferred to KE and back to APE (which results in oscillations of the density interface), can be transferred to

KE and dissipated, or can be changed to BPE due to mixing. Through various processes not discussed, the result of the latter two of these actions is ultimately an increase in BPE [57]. However, if the dimensionless amplitude is not large, the results from figure 3.21 suggest that the rate at which APE is irreversibly removed from the fundamental mode of the seiche is small. What this means is that the rate at which APE is transferred to BPE through mixing must also be small. This suggests that the energy remains in flux between KE and APE and is not used for mixing. Alternatively, with a large dimensionless amplitude, the rate at which APE is irreversibly removed from the fundamental mode of the seiche is larger, meaning that that APE must go *somewhere* such that it is unavailable for the large scale oscillation of the seiche. The results in figure 3.21 are insufficient to show where energy goes once it leaves the large scale oscillation of the seiche but it is more likely that through non–linear processes the large scale APE is transferred to higher horizontal modes of KE, illustrated in figure 3.18. These higher modes can then either be independently damped out by viscosity [22, 7] or contribute to the formation of shear instabilities. The second point having to do with the larger dimensionless amplitude is the fact that when the dimensionless amplitude is large enough, the combination of the resulting waves and the formation of shear instabilities changes the characteristic way in which the system gains BPE. The paradigm of 3.24 is that in the absence of shear instabilities, cases with the smallest aspect ratio have the largest relative change in BPE, with the relative change dropping exponentially with increasing aspect ratio. Cases with the lowest aspect ratio here have the largest periods, allowing diffusion to work for a longer time. However, when the amplitude becomes large enough such that shear instabilities occur, the character of the BPE increase begins to lose its exponential behaviour. In figure 3.24, the markers that are colored–in correspond to cases where shear instabilities are seen and the cases denoted by stars and triangles exhibit clear wave motion. Thus, by pairing waves and instabilities, the relative increase in BPE is increased. The confound here is that the cases with the largest dimensionless amplitude exhibit a completely different, almost quadratic, character in the relative change in BPE. This maximum in the efficiency suggests that the tank in that case is short enough that shear instabilities can occur multiple times while also allowing for formation of clear waves that can repeatedly increase the background potential energy. The point here is not the actual relative increase, which is very small on its own, but in how the relative increase changes when compared against other cases. These ideas above are summarized in figure 4.2. Notice the parallels as to where the bubbles are placed on both figures 4.1 and 4.2. For linear waves, there is very little mixing that occurs. In the region where shear instabilities occur as the primary degeneration mechanism, there is some mixing. Where there are small amplitude weakly non–linear waves, there is typically only a single mixing event, which could be small or vigorous depending on the amplitude. Finally, for cases where the amplitude is large, there are typically multiple mixing events

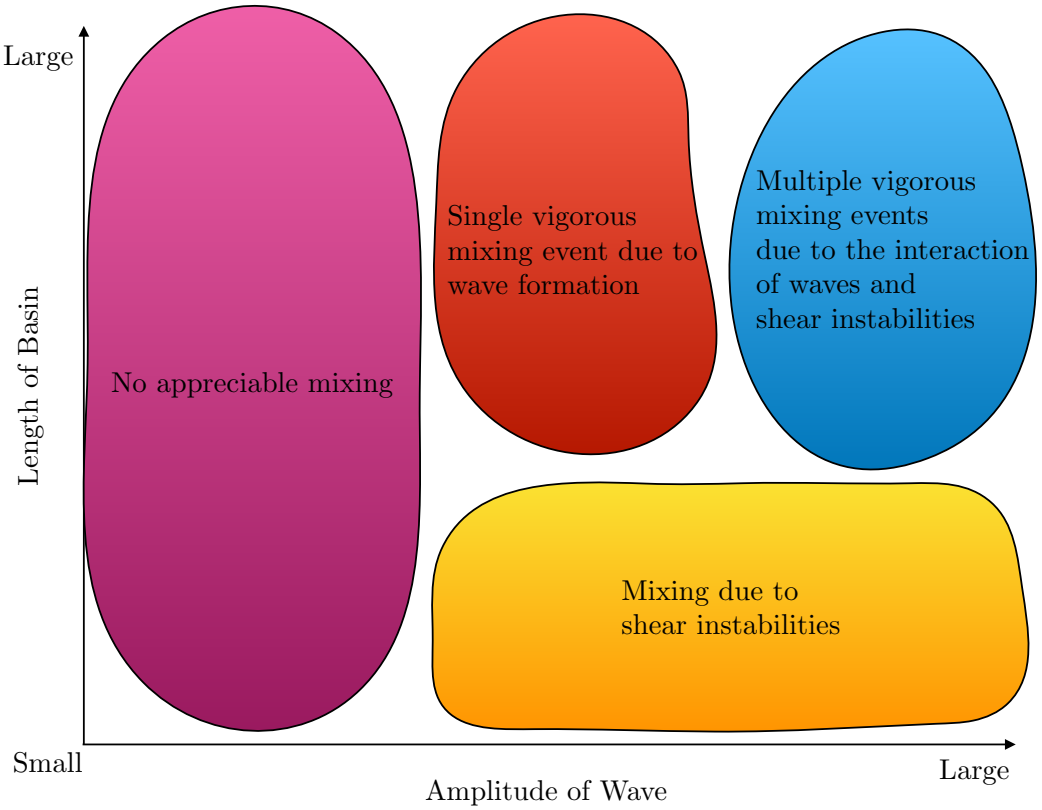

Figure 4.2: The proposed mixing regime diagram for a laboratory scale seiche. For small amplitudes and small tank lengths, there is almost no mixing that occurs. For large amplitude and reasonably short tanks, shear instabilities are seen to form which result in some mixing. For mid-length and mid–amplitude waves, wave trains form and for longer tanks with large amplitudes, both shear instabilities and wave trains form both of which mix fluid layers but at different amounts.

due to wave formation and shear instabilities. Rotation modified waves have been ignored in figure 4.2 because at the scales where rotation matters, mixing is typically a sub–grid scale process and must be parameterized in order to quantify its effects.

4.2 Future Work

The results presented in chapter 3 lend themselves to several different directions to build on, three of which will be briefly discussed in the last section of this chapter.

The first direction one could consider is to re–run a representative subset of the simulations presented above in 3D to compare the dynamics and instability within the flow. The second is adjusting the boundary conditions to better replicate what happens in a laboratory setting near the boundary with the goal of parameterizing across boundary layer transport of tracer and visualizing and characterizing boundary layer instability in the presence of a seiche. Finally, the third direction considered is to change the pycnocline structure in such a way as to excite higher vertical wave modes.

4.2.1 Understanding three dimensional dynamics

The scales that are considered in this thesis are comparable to length scales found in a laboratory, thus, it is not unreasonable to expect 3D dynamics to occur. Analysis of these dynamics could allow for a better and more complete spatial picture of the energetics as well as the mixing dynamics. Some representative cases discussed in this manuscript could be performed in 3D to see if the dynamics change during the transition to turbulence. By performing simulations in 3D, there are numerous instabilities that are able to occur that would otherwise not be possible in 2D. It is known that primary instabilities in the $x - z$ plane further decompose into secondary instabilities in the spanwise (y) direction [38, 30, 31]. By resolving 3D motion, the development of shear instability into a more complicated 3D instability could be discussed in the presence of a seiche. This analysis could lead to a better quantitative understanding of the effects of interfacial mixing in the context of a seiche and how it affects the bulk dynamics.

Due to the resolution of the cases discussed here, certain concessions must be made if studying 3D fluid flows is of interest such as less temporal resolution and shorter total simulation time. These barriers make analysis of temporal characteristics of the flow difficult rendering 2D cases suitable for inter-comparison and analysis of temporal behaviour.

4.2.2 Adjusting boundary conditions

Due to the fact that viscosity is small relative to other physical scales in a laboratory setting, boundary layers are very thin with respect to the fluid depth, and solving the Navier–Stokes equations including the boundary layer becomes a problem with multiple scales. Computationally, this amounts to disallowing parallel flow at the boundary. This condition is often called the "no–slip condition". To accurately simulate dynamics with the no–slip condition, grid points must be clustered near the boundary. To see why this is the case in spectral models, see Trefethen [50]. By clustering the points near the boundary, the resolution there increases dramatically, but there is a subsequent loss of resolution near the mid–depth of the domain.

Why studying the dynamics at the boundary might be of interest for future work is the effect that the boundary has on the large scale dynamics of the flow, the energetics of the seiche, and vertical transport capabilities of the seiche. By resolving the boundary, one could build an understanding of how the viscous dissipation at the boundary affects the dynamics of the large scale flow. It should be expected that by resolving the boundary layer, the rate at which APE is removed from the large scale seiche should be higher due to dissipation of KE at the boundary thereby allowing less energy to be stored as APE. As well, field studies have shown that the motion resulting from a seiche can contribute to the vertical transport of matter and biological material [29], so by utilizing high resolution simulations of seiche boundary layers, parameterizations of vertical transport of material could be created and used in larger scale models.

Some work has already been done on this. In figure 4.3 the tracer field is shown in a case similar to 25L5–4m, albeit with no–slip boundary conditions, at two different times. The concentration of the tracer is depicted by the intensity of the colour of the field with black corresponding to a concentration of 0 and white a concentration of 1. The oscillation of the seiche triggers a flow within the boundary layer that steepens and provides a means for vertical flux of the tracer.

4.2.3 Outer pycnocline

The last proposed direction that the current research could take is by superimposing a wider pycnocline onto the existing pycnocline. This change could affect the dynamics is in several ways, two of which are highlighted here. The first reason becomes evident when

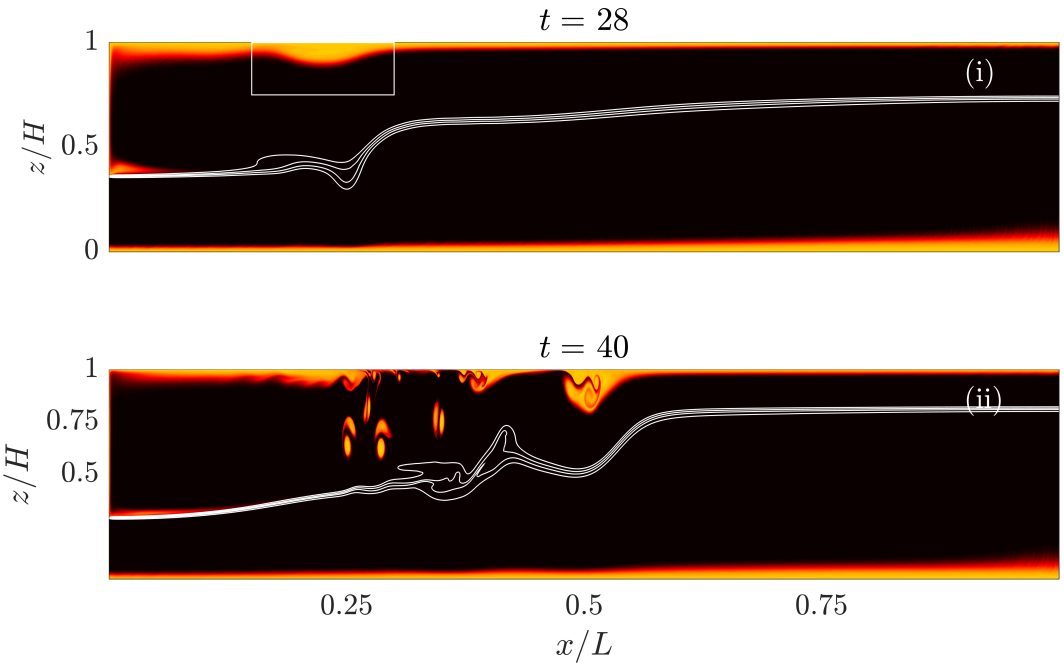

Figure 4.3: Shown is a tracer field added to a case analagous to 25L5–4m. The boundary conditions on the upper and lower boundaries in this case are no–slip while the lefthand and righthand boundaries are kept as free–slip. Black corresponds to a tracer concentration of 0 all the way to white which is concentration of 1. Density contours are plotted to reference where the wave is. Over the course of the oscillation of the seiche, a counter flow occurs in the boundary, possibly due to a combination of the chosen boundary conditions and the presence of sidewalls. At $t = 28$, a small bubble in the tracer forms which steepens and tracer is dragged downwards.

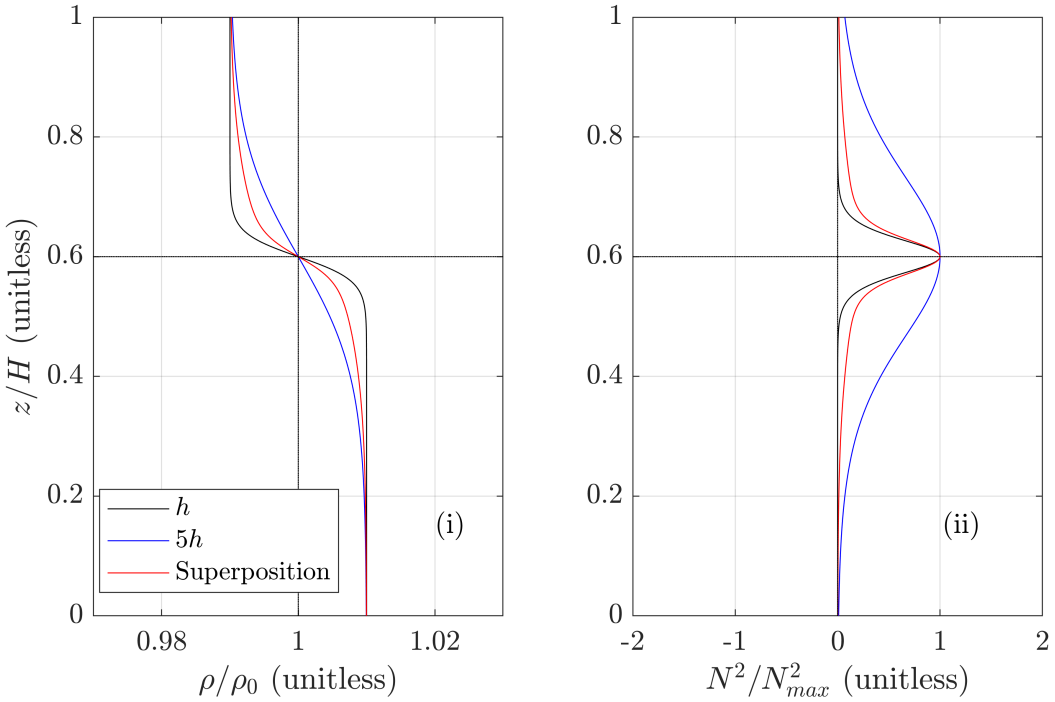

Figure 4.4: A comparison of the profiles of the three stratifications discussed in this section. The black curve is the profile of equation (2.48), the blue curve is equation (2.48) but allowing $h \to 5h$, and the red curve is the profile using equation (4.1).

equations (2.40) along with (2.41) are solved with the initial density profile

$$\rho(x,z) = \rho_0 + \frac{1}{4}(\rho_2 - \rho_1)\left(\tanh\left(\frac{z-z_0}{h}\right) + \tanh\left(\frac{z-z_0}{5h}\right)\right). \tag{4.1}$$

Comparing the profiles using h, $5h$, and the superposition of the stratification and the buoyancy frequency (figures 4.4 (i) and (ii) respectively), the clear difference is that the strongest stratification is more localized for the thin case (black curve), and very broad for the thick case (blue line), which is expected behaviour. What is interesting is that the stratification of the superposition of the two is still localized but is non–zero for a greater fraction of the total depth. The extra "tails" created by superimposing the more broad stratification onto the thin stratification provides evidence that the possible wave motion may differ due to the wider waveguide. The influence on the motion from this change to the pycnocline is clear from looking at figure 4.5 where the higher vertical modes vary over

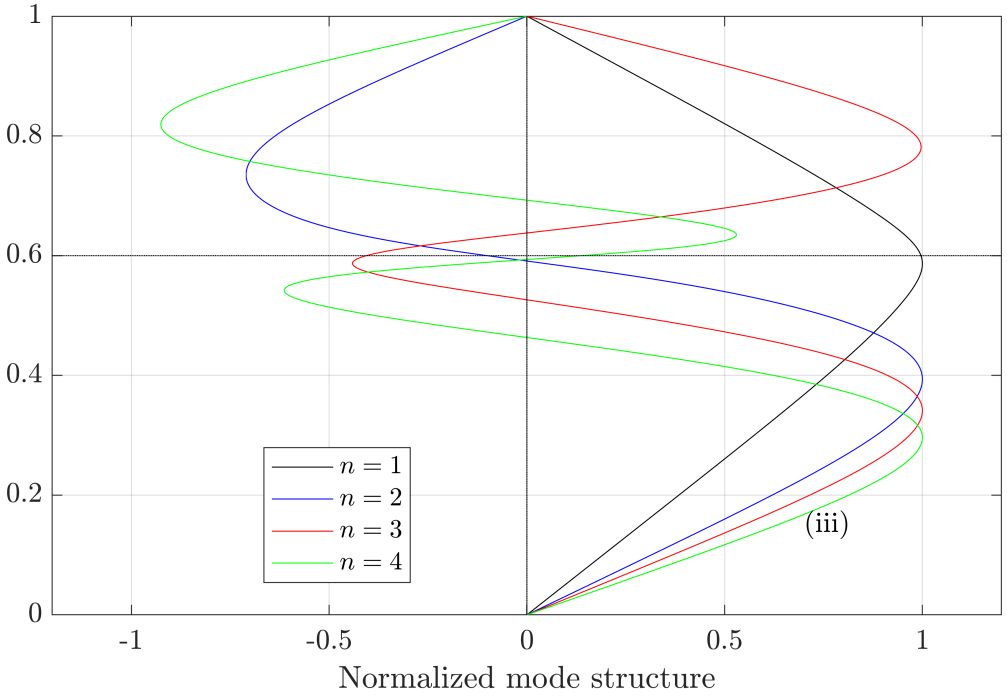

Figure 4.5: The first four vertical modes for the superimposed pycnocline in equation (4.1). The resulting stratification provides the possibility for higher vertical mode wave dynamics to appear lower in the water column away from the pycnocline.

a greater depth and may have a larger influence on the dynamics of the flow away from the pycnocline.

The second reason the dynamics might change is the suppression of shear instability. The effect that superimposing the wider pycnocline appears to have (at least at relatively early times) is to suppress the formation of shear instabilities on the density interface. In figure 4.6(i), there are clear shear instabilities as near the region of large horizontal velocity density, but when the pycnocline is widened to have a halfwidth of $5h$ in figure 4.6(ii), the horizontal velocity is lower and there are no shear instabilities present. Finally, when the wider pycnocline is superimposed onto the thinner pycnocline in figure 4.6(iii), it appears as if the horizontal velocity change across the pycnocline is similar to that of figure 4.6(i), except there are no shear instabilities present.

A qualitative interpretation of the density interfaces for these cases at this time reveals that the addition of the outer pycnocline appears to weaken the intrusion of lower density

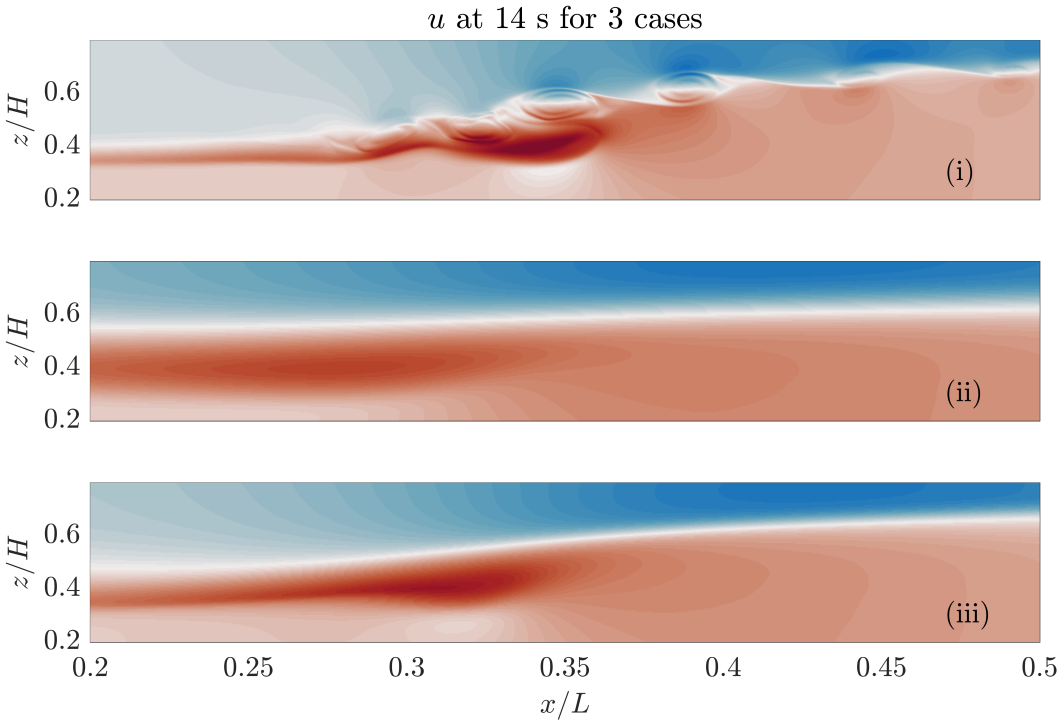

Figure 4.6: u at 14 s for three cases where the pycnocline structure is varied. Panel (i) begins with the initial condition given in equation (3.5) with $h = 0.005$ m. Panel (ii) depicts u with the initial condition of $h = 0.025$ (5 times wider than the thin case). Panel (iii) shows u with an initial stratification given by equation (4.1).

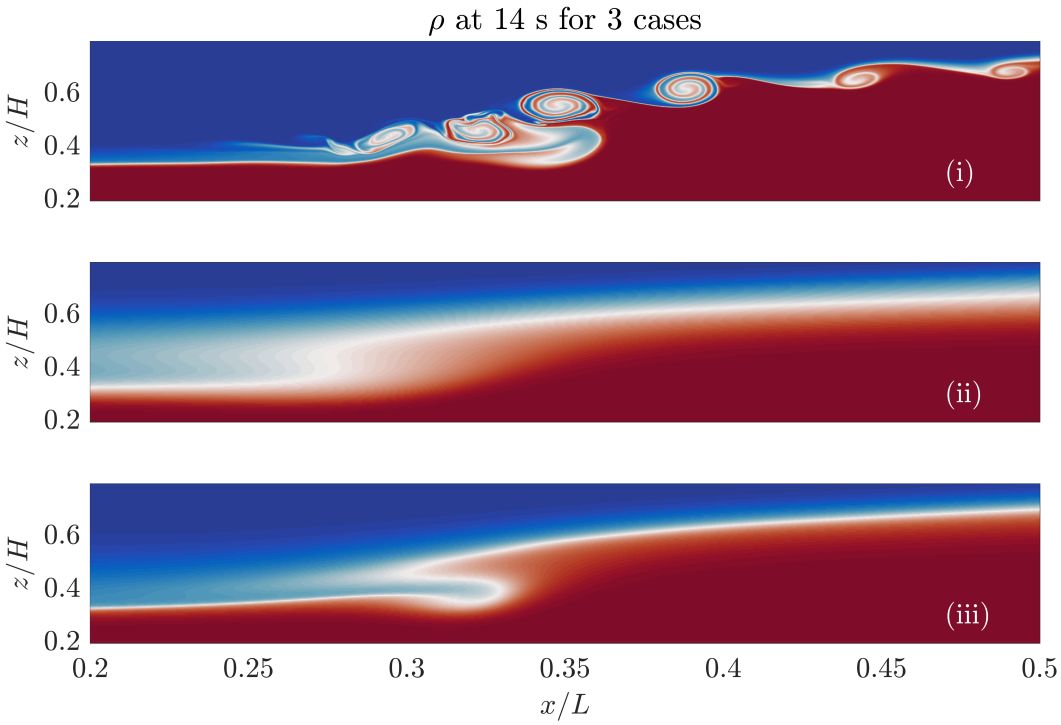

Figure 4.7: As in figure 4.6, but for the density field, ρ.

fluid into the higher density fluid but not totally remove it. In figure 4.7(i), there is a very strong intrusion of upper layer fluid into the bottom layer and in figure 4.7(ii), it is not apparent that the intrusion is there at all. By superimposing the outer pyncocline, the intrusion appears to weaken slightly and remove the instabilities that form ahead of the wave. More work needs to be done to verify this such as a wide parameter sweep of the single pycnocline cases and the addition of the outer pycnocline cases.

Bibliography

[1] D.J. Acheson. *Elementary Fluid Dynamics*. Clarendon Press, 1st edition, 1990.

[2] Michael F. Barad and Oliver B. Fringer. Simulations of shear instabilities in interfacial gravity waves. *Journal of Fluid Mechanics*, 644:61, 2010. ISSN 0022-1120. doi: 10.1017/S0022112009992035.

[3] George Keith Batchelor. *An Introduction to Fluid Dynamics*. Cambridge University Press, 2000.

[4] Eric Bembenek, Francis J Poulin, and Michael L Waite. Realizing Surface-Driven Flows in the Primitive Equations. *J. Phys. Oceanogr.*, 45(5):1376–1392, 2015. ISSN 0022-3670. doi: 10.1175/jpo-d-14-0097.1.

[5] David John Benney. Long Non-Linear Waves in Fluid Flows. *Studies In Applied Mathematics*, 45:52–63, 1966.

[6] L. Boegman, J. Imberger, G. N. Ivey, and J. P. Antenucci. High-frequency internal waves in large stratified lakes. *Limnology and Oceanography*, 48(2):895–919, 2003. ISSN 00243590. doi: 10.4319/lo.2003.48.2.0895.

[7] L. Boegman, Ivey G. N., and J. Imberger. The energetics of large-scale internal wave degeneration in lakes. *Journal of Fluid Mechanics*, 531:159–180, 2005. ISSN 0022-1120. doi: 10.1017/S0022112005003915.

[8] Bertram Boehrer and Martin Schultze. Stratification of lakes. *Reviews of Geophysics*, 46(2):1–27, 2008. ISSN 87551209. doi: 10.1029/2006RG000210.

[9] Bertram Boehrer, Ryuji Fukuyama, and Kazuhisa Chikita. Stratification of very deep, thermally stratified lakes. *Geophysical Research Letters*, 35(16):8–12, 2008. ISSN 00948276. doi: 10.1029/2008GL034519.

[10] Peter Brandt, Angelo Rubino, Werner Alpers, and Jan O Backhaus. Internal waves in the Strait of Messina studied by a numerical model and synthetic aperture radar images from the ERS 1/2 satellites. *Journal of Physical Oceanography*, 27(5):648–663, 1997. ISSN 0022-3670. doi: 10.1175/1520-0485(1997)027⟨0648:IWITSO⟩2.0.CO;2.

[11] Magda Carr, Stuart E King, and David G Dritschel. Numerical simulation of shear-induced instabilities in internal solitary waves. *Journal of Fluid Mechanics*, 683:263–288, 2011. ISSN 0022-1120. doi: 10.1017/jfm.2011.261.

[12] Aaron Coutino and Marek Stastna. The fully nonlinear stratified geostrophic adjustment problem. *Nonlinear Processes in Geophysics*, 24:61–75, 2017. ISSN 16077946. doi: 10.5194/npg-24-61-2017.

[13] Aaron Coutino, Marek Stastna, Shawn Kovacs, and Eduard Reinhardt. Hurricanes Ingrid and Manuel (2013) and their impact on the salinity of the Meteoric Water Mass, Quintana Roo, Mexico. *Journal of Hydrology*, 551:715–729, 2017. ISSN 00221694. doi: 10.1016/j.jhydrol.2017.04.022.

[14] Alberto de la Fuente, Kenji Shimizu, Jörg Imberger, and Yarko Niño. The evolution of internal waves in a rotating, stratified, circular basin and the influence of weakly nonlinear and nonhydrostatic accelerations. *Limnology and Oceanography*, 53(6):2738–2748, 2008. ISSN 00243590. doi: 10.4319/lo.2008.53.6.2738.

[15] David Deepwell, Marek Stastna, and Aaron Coutino. Multi-scale phenomena of rotation-modified mode-2 internal waves. *Nonlinear Processes in Geophysics*, 25:217–231, 2018.

[16] Abbas Dorostkar, Leon Boegman, and Andrew Pollard. Three-dimensional simulation of high-frequency nonlinear internal wave dynamics in Cayuga Lake. *Journal of Geophysical Research: Oceans*, 122(3):2183–2204, 2017. ISSN 21699291. doi: 10.1002/2016JC011862.

[17] John Grue, Atle Jensen, Per-Olav Rusås, and J. Kristian Sveen. Properties of large-amplitude internal waves. *Journal of Fluid Mechanics*, 380:257–278, 1999. ISSN 00221120. doi: 10.1017/S0022112098003528.

[18] Richard Haberman. *Elementary Applied Partial Differential Equations*. Prentice Hall Englewood Cliffs, NJ, 1983.

[19] Karl R. Helfrich and W. Kendall Melville. Long nonlinear internal waves. *Annual Review of Fluid Mechanics*, 38(1):395–425, 2006. ISSN 0066-4189. doi: 10.1146/annurev.fluid.38.050304.092129.

[20] Stephen M. Henderson and Bridget R. Deemer. Vertical propagation of lakewide internal waves. *Geophysical Research Letters*, 39(6):2–6, 2012. ISSN 00948276. doi: 10.1029/2011GL050534.

[21] D A Horn, J Imberger, G N Ivey, and L G Redekopp. A weakly nonlinear model of long internal waves in closed basins. 467:269–287, 2002. doi: 10.1017/S0022112002001362.

[22] D.A. Horn, J. Imberger, and G.N. Ivey. The degeneration of large-scale interfacial gravity waves in lakes. *J. Fluid Mech*, 434:181–207, 2001.

[23] D. J. Korteweg and G. de Vries. On the change of form of long waves advancing in a rectangular canal, and on a new type of long stationary waves. *Philosophical Magazine Series 5*, 39(240):422–443, 1895. ISSN 1941-5982. doi: 10.1080/14786449508620739.

[24] Pijush K. Kundu, Ira Cohen, and David Dowling. *Fluid mechanics*. Elsevier, 5th edition, 2012. ISBN 0077422414. doi: 10.1111/j.1549-8719.2009.00016.x.Mechanobiology.

[25] Kevin G. Lamb. Are solitary internal waves solitons? *Studies in Applied Mathematics*, 101:289–308, 1998. ISSN 0022-2526. doi: 10.1111/1467-9590.00094.

[26] Kevin G. Lamb and David Farmer. Instabilities in an Internal solitary-like wave on the Oregon Shelf. *Journal of Physical Oceanography*, 41(1):67–87, 2011. ISSN 0022-3670. doi: 10.1175/2010JPO4308.1.

[27] Kevin G. Lamb and Van T. Nguyen. Calculating energy flux in internal solitary waves with an application to reflectance. *Journal of Physical Oceanography*, 39(3):559–580, 2009. ISSN 0022-3670. doi: 10.1175/2008JPO3882.1.

[28] Bruce D Lazerte. The dominating higher order vertical modes of the internal seiche in a small lake. *Limnology and Oceanography*, 25(5):846–854, 1980. ISSN 00243590. doi: 10.4319/lo.1980.25.5.0846.

[29] Sally MacIntyre, Kevin M. Flynn, Robert Jellison, and José R. Romero. Boundary mixing and nutrient fluxes in Mono Lake, California. *Limnology and Oceanography*, 44(3):512–529, 1999. ISSN 00243590. doi: 10.4319/lo.1999.44.3.0512.

[30] A. Mashayek and W. R. Peltier. The 'zoo' of secondary instabilities precursory to stratified shear flow transition. Part 1 Shear aligned convection, pairing, and braid instabilities. *Journal of Fluid Mechanics*, 708:5–44, 2012. ISSN 1469-7645. doi: 10.1017/jfm.2012.304.

[31] A. Mashayek and W. R. Peltier. The 'zoo' of secondary instabilities precursory to stratified shear flow transition. Part 2 The influence of stratification. *Journal of Fluid Mechanics*, 708:5–44, 2012. ISSN 1469-7645. doi: 10.1017/jfm.2012.304.

[32] T. Maxworthy, Jörg Imberger, and A. Saggio. *A laboratory demonstration of a mechanism for the production of secondary, internal gravity-waves in a stratified fluid*. American Geophysical Union, 1998.

[33] J.C. McWilliams. *Fundamentals of geophysical fluid dynamics*. 2006.

[34] J W Miles. The Korteweg-de Vries equation: a historical essay. *J. Fluid Mech.*, 106: 131–147, 1981.

[35] Clifford Hiley Mortimer. *Lake Hydrodynamics*. 1974.

[36] Jason Olsthoorn and Stuart B. Dalziel. Vortex-ring-induced stratified mixing: Mixing model. *Journal of Fluid Mechanics*, 837:129–146, 2018. ISSN 14697645. doi: 10.1017/jfm.2017.846.

[37] I. Ostrovsky, Y. Z. Yacobi, P. Walline, and I. Kalikhman. Seiche-induced mixing: its impact on lake productivity. *Limnology and Oceanography*, 41(2):323–332, 1996. ISSN 00243590. doi: 10.4319/lo.1996.41.2.0323.

[38] W. R. Peltier and C. P. Caulfield. Mixing efficiency in stratified shear flows. *Annual Review of Fluid Mechanics*, 35(1):135–167, 2003. ISSN 0066-4189. doi: 10.1146/annurev.fluid.35.101101.161144.

[39] W.H. Press. *Numerical Recipes in C: The art of scientific computing*. Cambridge University Press, 1992. ISBN 9780521437202.

[40] M. Preusse, H. Freistühler, and F. Peeters. Seasonal variation of solitary wave properties in Lake Constance. *Journal of Geophysical Research: Oceans*, 117(4):1–14, 2012. ISSN 21699291. doi: 10.1029/2011JC007403.

[41] Martina Preusse, Frank Peeters, and Andreas Lorke. Internal waves and the generation of turbulence in the thermocline of a large lake. *Limnology and Oceanography*, 55(6): 2353–2365, 2010. ISSN 00243590. doi: 10.4319/lo.2010.55.6.2353.

[42] Martina Preusse, Marek Stastna, Heinrich Freistühler, Frank Peeters, and Guido Germano. Intrinsic breaking of internal solitary waves in a deep lake. *PLoS ONE*, 7(7), 2012. doi: 10.1371/.

[43] Rick Salmon. *Lectures on geophysical fluid dynamics*. Oxford University Press, New York, 1st edition, 1998.

[44] E. A. Spiegel and G Veronis. On the Boussinesq Approximation for a Compressible Fluid. *The Astrophysical Journal*, 131:442, 1960. ISSN 0004-637X. doi: 10.1086/146849.

[45] D. T. Steinmoeller, M. Stastna, and K. G. Lamb. Fourier pseudospectral methods for 2D Boussinesq-type equations. *Ocean Modelling*, 52-53:76–89, 2012. ISSN 14635003. doi: 10.1016/j.ocemod.2012.05.003.

[46] D. T. Steinmoeller, M. Stastna, and K. G. Lamb. Pseudospectral methods for Boussinesq-type equations in an annular domain with applications to mid-sized lakes. *Journal of Computational Science*, 4(1-2):3–11, 2013. ISSN 18777503. doi: 10.1016/j.jocs.2012.01.005.

[47] Benjamin A. Storer, Francis J. Poulin, and Claire Ménesguen. The Dynamics of Quasi-Geostropic Lens-Shaped Vortices. *Journal of Physical Oceanography*, pages JPO–D–17–0039.1, 2017. ISSN 0022-3670. doi: 10.1175/JPO-D-17-0039.1.

[48] Christopher J. Subich, Kevin G. Lamb, and Marek Stastna. Simulation of the Navier-Stokes equations in three dimensions with a spectral collocation method. *International Journal for Numerical Methods in Fluids*, 73(2):103–129, 2013. ISSN 02712091. doi: 10.1002/fld.3788.

[49] Kristen M. Thyng, Chad A. Greene, Robert D. Hetland, Heather M. Zimmerle, and Steven F. DiMarco. True colors of oceanography: guidelines for effective and accurate colormap selection. *Oceanography*, 29(3):9–13, 2016. ISSN 10428275. doi: 10.5670/oceanog.2016.66.

[50] Lloyd N. Trefethen. *Spectral Methods in Matlab*. The Society for Industrial and Applied Mathematics, Philadelphia, first edition, 2000.

[51] David J. Tritton. *Physical Fluid Dynamics*. Springer Science \& Business Media, 2012.

[52] Cary D. Troy and Jeffrey R. Koseff. The instability and breaking of long internal waves. *Journal of Fluid Mechanics*, 543:107–136, 2005. ISSN 00221120. doi: 10.1017/S0022112005006798.

[53] E.R. Watson. Movements of the waters of Loch Ness, as indicated by temperature observations. *The Geographical Journal*, 24(4):430–437, 1904.

[54] R.F. Weiss, E.C. Carmack, and V.M. Koropalov. Deep-water renewal and biological production in Lake Baikal. *Nature*, 349, 1991. ISSN 0028-0836. doi: 10.1038/350055a0.

[55] Gerald Beresford Whitham. *Linear and nonlinear waves*. John Wiley \& Sons, 1999.

[56] K. B. Winters and E. A. D'Asaro. Diascalar flux and the rate of fluid mixing. *Journal of Fluid Mechanics*, 317(1996):179–193, 1996. ISSN 0022-1120. doi: 10.1017/S0022112096000717.

[57] Kraig B. Winters, Peter N. Lombard, James J. Riley, and Eric a. D'Asaro. Available potential energy and mixing in density-stratified fluids. *Journal of Fluid Mechanics*, 289:115–128, 1995. ISSN 0022-1120. doi: 10.1017/S002211209500125X.

[58] I.R. Wood and J. E. Simpson. Jumps in layered miscible fluids. *Journal of Fluid Mechanics*, 140(EMS):329–342, 1984. ISSN 14697645. doi: 10.1017/S0022112084000628.

[59] Alfred Wüest and Andreas Lorke. Small scale hydrodynamics in lakes. *Annual Review of Fluid Mechanics*, 35(1):373–412, 2003. ISSN 0066-4189. doi: 10.1146/annurev.fluid.35.101101.161220.